Technischen Universität München
Fakultät für Physik
Institut für Experimentalphysik E21

Quantitative time resolved neutron imaging methods at the high flux neutron source FRM-II

Johannes Brunner

Vollständiger Abdruck der von der Fakultät für Physik
der Technischen Universität München zur Erlangung des akademischen Grades eines

Doktors der Naturwissenschaften

genehmigten Dissertation.

Vorsitzender:	Univ. Prof. Dr. M. Kleber
Prüfer der Dissertation:	1. Univ. Prof. Dr. P. Böni
	2. Univ. Prof. Dr. W. Petry

Die Dissertation wurde am 19.09.2005 bei der Technischen Universität München eingereicht und durch die Fakultät für Physik am 01.03.2006 angenommen.

"One picture is worth a thousand words"

chinese saying

Abstract

English

In the current work various new experimental methods and computation procedures in the field of neutron imaging are presented. These methods have a significant technical importance in non-destructive material investigations.

With stroboscopic neutron radiography periodic processes can be investigated on a sub-millisecond time scale. This opens great opportunities for the study and the development of combustion engines.

Energy selective time of flight neutron radiography at neutron spallation sources uses the energy dependence of the neutron cross section to distinguish between materials. The energy resolution of this technique is very good and allows the identification of specific materials.

Software tools for neutron radiography data evaluation and data visualization were programmed: calibration algorithms, image deconvolution procedures, tools for image assessment, a graphical user interface for fast data inspection and many batch processing routines for large neutron radiography image series.

The developed methods and software tools are in use at the neutron radiography and tomography facilities at new research reactor FRM-II in Munich, Germany.

Zusammenfassung

Deutsch

In der vorliegenden Arbeit werden verschiedene neue experimentelle Methoden und Rechenverfahren aus dem Gebiet der Radiographie und Tomographie mit Neutronen vorgestellt. Diese Durchstrahlungsverfahren gewinnen zunehmend an Bedeutung für die zerstörungsfreie Prüfung von neuen Materialien.

Mit der stroboskopischen Neutronenradiographie-Methode können periodische Prozesse auf einer Submillisekunden-Zeitskala untersucht werden. Das eröffnet viele verheißungsvolle Möglichkeiten für das Studium und die Weiterentwicklung von Verbrennungsmotoren.

Die energieaufgelöste Flugzeit-Neutronenradiographie an Neutronen-Spallationsquellen nützt die Energieabhängigkeit der Schwächungskoeffizienten aus, um zwischen verschiedenen Materialien zu unterschieden. Durch die hohe Energieauflösung dieser Methode wird das gezielte Suchen nach bestimmten Materialien in einem unbekannten Objekt möglich.

Softwarewerkzeuge für die Auswertung und Visualisierung von Neutronenradiographie-Daten wurden programmiert: Evaluierungsalgorithmen, Programme zur Entfaltung der Bildunschärfe und zur Korrektur von Artefakten, eine graphische Benutzeroberfläche für die schnelle Dateninspektion, Algorithmen zur Bestimmung der Bildqualität sowie Routinen für die Stapelverarbeitung von großen Bildserien.

Die neuen experimentellen Methoden und Softwarewerkzeuge werden an den Neutronenradiographie- und -tomographieanlagen am neuen Forschungsreaktor München FRM-II eingesetzt.

Contents

Introduction

Neutron imaging (NI) is a collective term for non-destructive testing (NDT) methods which use the penetration of neutrons for the investigation of the internal structure of an object. The unique information delivered by Neutron Radiography (NR) and Neutron Tomography (NT) contribute to the development of high tech products and concedes insight into historical and archeological objects.

The first NR images were taken in 1940, at the beginning of the 80's the method was applied at the research reactor FRM in Garching with thermal and soon with fast neutrons. With the use of large 2D detectors and increasing computing power the NI methods really got established. In the last years new methods like energy selective NR, phase contrast NR and many new areas of applications opened up. High flux neutron sources and a growing interest from industry and science pushed the activities in the field and gave new opportunities for methodical improvements. In the last five years eight diploma and PhD theses about NI appeared.

This work is dedicated to new experimental methods for time resolved neutron imaging and methods for quantitative data analysis. It consists of five chapters:

Chapter 1 starts with the principle and the physics of NR and presents the exponential attenuation model. For a wider understanding of neutron imaging deviations from the simple model like neutron scattering, total reflection, effects due to the beam geometry and spectral effects are discussed.

The experimental setup of a NI facility is treated in chapter 2. At the FRM-II two facilities for neutron imaging are available: The ANTARES facility with a cold neutron spectrum and the NECTAR facility with a fast fission spectrum. The ANTARES facility is presented and described focussing on the beam, the detector and possible objects of investigation.

A major part of this work consists of new and powerful techniques for quantitative evaluation and visualization of NR data (chapter 3). All important steps of the evaluation procedure are described and the software "Neutroneye" for visualization is explained.

Within this work two new experimental methods were developed and applied in practical measurements: the stroboscopic neutron imaging technique and the energy selective time of flight NR. In chapter 4 both techniques are introduced and the experiments, carried out at neutron imaging facilities in Europe, are described and their results are discussed.

Chapter 1

Physics of neutron imaging

The object of investigation is placed in a well defined neutron beam $I_0(x, y)$ and a 2D position sensitive detector records the transmitted radiation intensity $I(x, y)$, the radiography image (1.1). This shadow image contains information about the internal structure of the object.

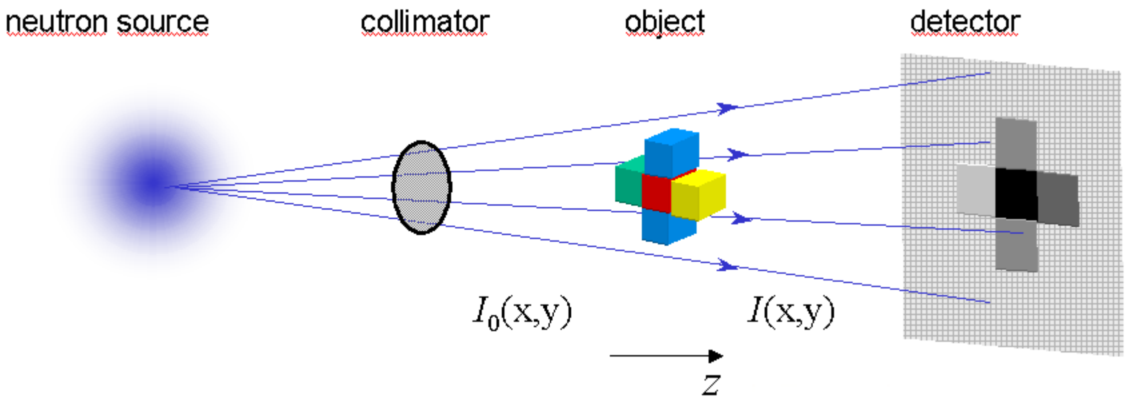

Figure 1.1: Principle of neutron radiography

For neutron tomography, a series of NR images from different directions are measured by rotating the object. From the images stack the complete 3D volume of the object is reconstructed. A detailed mathematical description of the tomographic reconstruction can be found in [Kak88, 0]. The grey levels of each volume element (voxel) correspond to the attenuation coefficient of that element's material. In this way materials differing in the neutron attenuation coefficients can be distinguished and the individual components of a multi composite object can be separated.

Neutron imaging is complementary to other NDT methods and often permits a non destructive analysis when other methods fail. Characteristic for NI is the unique ability to penetrate large metallic objects and at the same time the sensitivity for hydrogenous materials. In the following some examples of typical applications are listed:

- penetration behaviour of water in soil, wood, stone, concrete, textiles and development of hydrophobic agents
- dynamics of lubrication liquids in combustion engines
- behaviour of samples under mechanical, electrical or chemical load
- defect detection in metal casts, 3D measuring of thick metallic samples like turbine blades

- measurement of distributions of the electrolyte in batteries and rechargeable batteries under different working conditions
- inspection of historical objects
- autoradiographies of paintings
- localization and preparation of fossils in rocks
- control examinations of seals, pyro-elements and switches of high security relevance
- studies of liquid balances in plants, animals and food
- time dependent liquid distributions in cooling aggregates and heat exchangers
- measurement of boron distributions in steel
- inspection of carbon fiber materials
- investigation of helicopter rotor blades
- investigation of archeological objects
- measurement of glue distributions

1.1 Exponential attenuation model

How the neutron beam is attenuated by objects depends on the object geometry, its thickness and its material composition. In a first approximation for neutrons as well as for x-rays the exponential attenuation law, also known as Lambert Beer law, is valid:

$$I(z) = I_0\, e^{-\Sigma z} \qquad \Sigma = \Sigma_\rho \cdot \rho = \frac{\sigma_{tot}}{A \cdot amu} \cdot \rho = \sigma_{tot} \cdot n \tag{1.1}$$

$I(z)$	... neutron intensity after a distance z in material $\left[\frac{n}{cm^2\, s}\right]$
I_0	... neutron intensity before the object $\left[\frac{n}{cm^2\, s}\right]$
z	... distance in the material $[cm]$
Σ	... attenuation coefficient $\left[\frac{1}{cm}\right]$
Σ_ρ	... mass attenuation coefficient $\left[\frac{cm^2}{g}\right]$
σ_{tot}	... total cross section $\left[cm^2\right]$
ρ	... material density $\left[\frac{g}{cm^3}\right]$
A	... nuclear mass number $[\,]$
$amu = 1,660 \cdot 10^{-24}$	... atomic mass unit $[g]$
n	... atomic density of the material $\left[\frac{g}{cm^3}\right]$

How strong neutrons and photons are attenuated per cm material is determined by the material specific attenuation coefficient Σ_ρ. The mass attenuation coefficient (Fig. 1.2) σ is independent of the material density and allows the comparison of the microscopic attenuation properties between the atoms, the cross sections.

For x-rays Σ increases (black line) with the atomic number Z because the photons interact with the electrons in the atomic shell. The higher the photon energies are the lower is the attenuation and the resulting contrasts between the elements (green and brown line). The attenuation for neutrons differs between fast and thermal neutrons. Fast neutrons

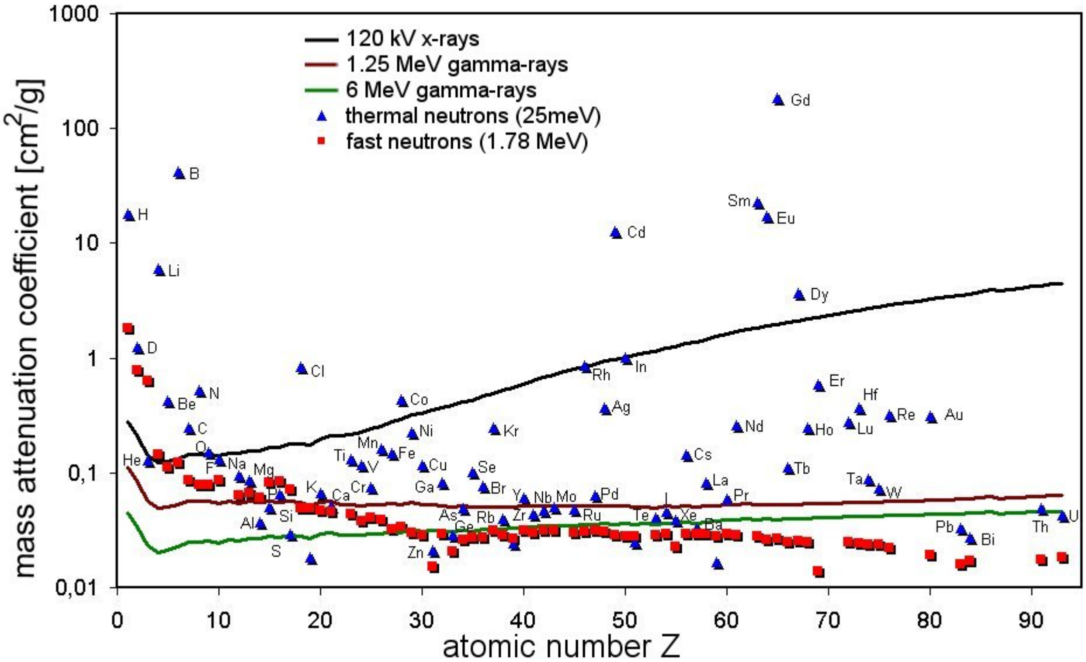

Figure 1.2: Attenuation properties of the elements for neutrons and X-rays [Iae05, 3]

interact with matter mainly via elastic scattering while thermal and cold neutrons interact more via nuclear reactions. Thus, for fast neutrons (red dots) Σ decreases with increasing mass of the target nuclei and for the thermal neutrons (blue dots) Σ depends on the inner structure of the atomic core showing no regularity along Z. For thermal neutrons many metals are transparent and hydrogen in contrast is strongly attenuating. Neighboring elements in the periodic table have completely different attenuation coefficients.
For small attenuations the exponential attenuation law can be approximated by a Taylor series:

$$I(z)/I_0 = e^{-\Sigma z} \approx 1 - \Sigma z/1! \qquad \text{Error:}\Sigma^2 z^2/2! \tag{1.2}$$

For $\Sigma z = 0.1$ (attenuation $I/I_0 \approx 90.4\%$) the approximation error is only 0.5%.
The aim of neutron imaging is the measurement of I/I_0 via the grey levels in the NR image as exact as possible. But the physical model of neutron attenuation and detection has some limits, which can not be neglected and are treated individually in this chapter. Since the attenuation properties for fast neutrons are quite different, especially the limits for cold and thermal neutrons are studied. If the underlying processes can be understood and modelled, I/I_0 can be measured with a higher precision and even more information can be extracted from the object.

1.2 Effects of neutron scattering

According to equation 1.2 only neutrons transmitted through the object contribute to the radiography image. In reality this is not correct. Scattered neutrons can lead to considerable artefacts in the NR image (Fig. 1.3). The red line and the black line are the attenuation profiles with and without the contribution of scattered neutrons from the object.

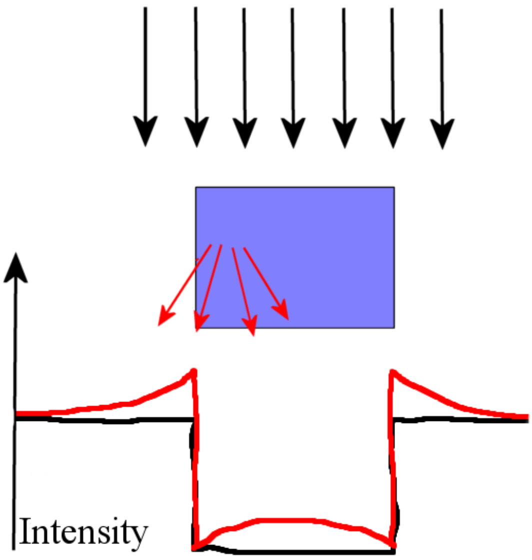

Figure 1.3: Neutron scattering in the object

De Broglie postulated in 1923 that the wave-particle dualism was valid not only for photons but also for massive particles. The relations between wavelength λ, energy E and velocity v for the non relativistic case are listed in table 1.1.

$\lambda = \frac{h}{m_n v}$	$\lambda\,[\text{Å}] \approx \frac{9.9}{v\left[\frac{m}{s}\right]}$	$\lambda = \frac{h}{\sqrt{2\,m_n\,E}}$	$\lambda\,[\text{Å}] \approx \frac{9.0}{\sqrt{E[meV]}}$
$E = \frac{h^2}{2\,m_n\,\lambda^2}$	$E\,[meV] \approx \frac{81.8}{\lambda[\text{Å}]^2}$	$E \approx \frac{1}{2} m_n v^2$	$E\,[meV] \approx 5.2 \cdot 10^{-6}\, v\,\left[\frac{m}{s}\right]^2$
$v = \sqrt{\frac{2\,E}{m_n}}$	$v\,\left[\frac{m}{s}\right] \approx 473 \cdot \sqrt{E\,[meV]}$	$v = \frac{h}{m_n\,\lambda}$	$v\,\left[\frac{m}{s}\right] \approx \frac{3964}{\lambda[\text{Å}]}$

Table 1.1: Relations between neutron energy, wavelength and velocity

Considering the neutron beam as an incoming wave the neutrons leaving the object are outgoing waves. In the first approximation the object is a source of spherical waves (s-wave scattering) and the neutron scattering can be assumed to be isotropic in the laboratory system. Thus, the intensity of scattered neutrons I should diminish with distance d from the object with $I \propto 1/d^2$. This is not perfectly true, especially for light target nuclei an isotropic scattering in the center of mass system is a better assumption. The correction factor according to [Eme82, 1] and [Due76, 2] is $\overline{cos(\phi)} = 2/3A$ where is A mass of the target and ϕ the angle of scattered neutrons in the laboratory system. For light target nuclei (small A) forward scattering is significantly predominant. Hydrogen for instance has an average angle ϕ of 48° towards the flight direction of the neutron in comparison to 90° in the case of isotropic scattering.

For low neutron energies the chemical bond of a target nucleus as well as the temperature of the target can influence the scattering process. The probability of scattering of a nucleus bond in a molecule can be up to a factor $(1+1/A)^2/(1+1/M)^2$ higher compared to free nuclei, where A is the weight of the nucleus and M is the weight of the bonding system. The thermal motion of the target nuclei changes the relative speed between incident neutrons and these nuclei. For this purpose effective cross sections depending on neutron energy and target temperature can be defined.

The stronger the scattering source is and the closer it is to the detector the stronger is its effect on the NR image. The object, the beam stop and the detector itself are the main sources of scattered neutrons. In Fig. 1.4 hydrogenous biological objects were inspected with a minimal distance to the detector. The scattered neutrons give rise to bright halos around the objects in the NR image. In order to visualize the scattering effect the NR image is displayed in false colors.

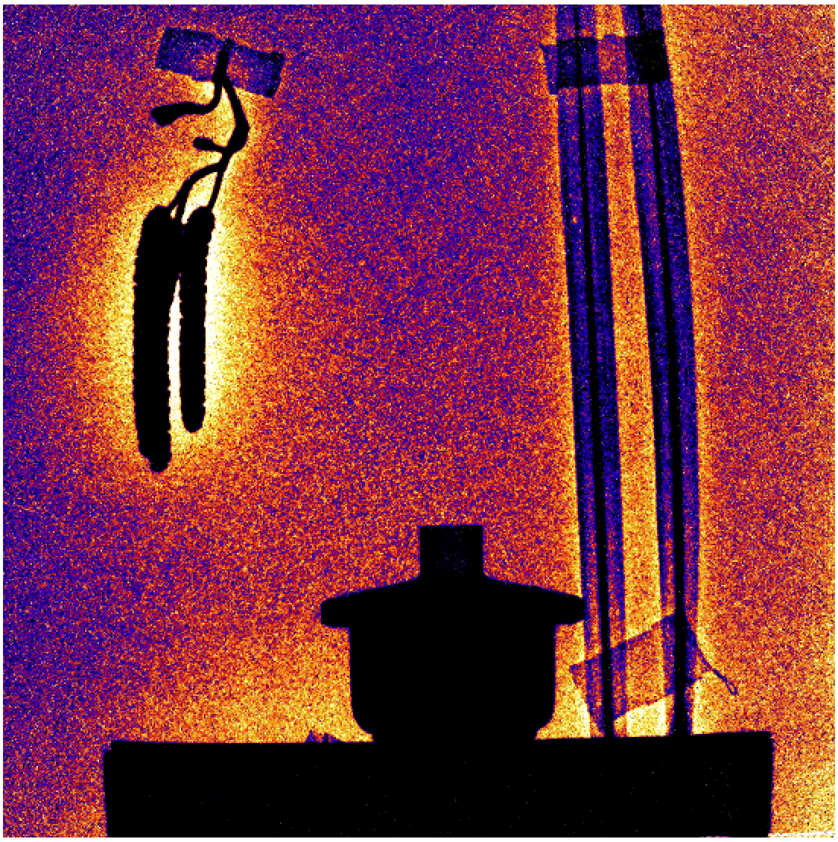

Figure 1.4: NR of biological objects, artefacts due to scattered neutrons

By choosing a large distance between object and detector the effect of scattered neutrons can easily be reduced. Even if the major fraction of scattered neutrons normally come from the object, also the beam stop or the mirror is a source of scattered neutrons. It makes sense to limit the neutron beam to the smallest size necessary. This minimizes the background of scattered neutrons.

1.3 Effects of total reflection

For neutrons that impinge under a small angle on a plane surface, total reflection may occur (see Fig. 1.5). This effect is well known and it is used for neutron transport in neutron guides. In neutron imaging however, total reflection was not observed yet.

The neutron refraction index n is given in equation 1.3 by:

$$n^2 = 1 - N_A \cdot b_{coh} \cdot \frac{\lambda^2}{\pi} \tag{1.3}$$

n ... refraction index [ ]
N_A ... atomic density $\left[\frac{1}{cm^3}\right]$

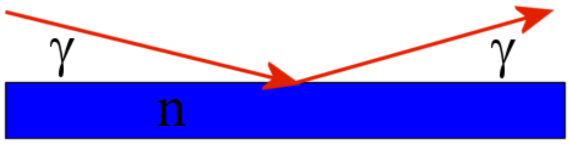

Figure 1.5: Total reflection

b_{coh}	...	coherent scattering length $[cm]$
λ	...	neutron wavelength $\left[\frac{1}{cm}\right]$

The neutron refraction index is very small and for most materials smaller than one (see Tab. 1.2). This means that total reflection for neutrons occurs only on very plane surfaces at small angles and depend on the scattering length of the scattering material and the wavelength of the neutrons.

material	$N_A \cdot b_{coh}$ $\left[10^{-6}\text{Å}^{-2}\right]$	material	$N_A \cdot b_{coh}$ $\left[10^{-6}\text{Å}^{-2}\right]$
Ni^{58}	13.31	Aluminium	2.08
C (diamond)	11.71	Silicon	2.08
Nickel	9.40	Vanadium	0.27
Quartz	3.64	Titanium	-1.95
Germanium	3.62	Manganese	-2.95
Silver	3.50		

Table 1.2: Neutron refraction index ([Fur99, 4])

Since the effect is stronger at lower energies, these disturbing artefacts appear presumably at cold beam lines.
If the angle between the incident neutron and the surface is below the critical angle total reflection can occur. The critical angle γ for the total reflection of neutrons is:

$$\gamma = \lambda \cdot \sqrt{\frac{N_A \cdot b_{coh}}{\pi}} \cdot \frac{360}{2\pi} \tag{1.4}$$

For Ni^{58} the angle of total reflection is $0.1°/\text{Å}$.
In Fig. 1.6 the total reflection of a neutron mirror was observed at the ANTARES facility at FRM-II. The NR image shows the object (black), a 30 cm long super mirror (m=2) and a 30% higher flux 4 mm above the surface. The distance between object and detector is about 50 cm. The rhombic form of the reflex can be attributed to the tilting between mirror and the beam direction.

Likewise total reflections from the rotation table for tomography were detected in some images. Though this effect disturbs neutron imaging, it could be used for the inspection of neutron optical devices in future.

1.4 Spectral effects in neutron imaging

Other deviations from the exponential attenuation model are spectral effects. The attenuation coefficient of a material Σ is not constant but varies with the neutron energy

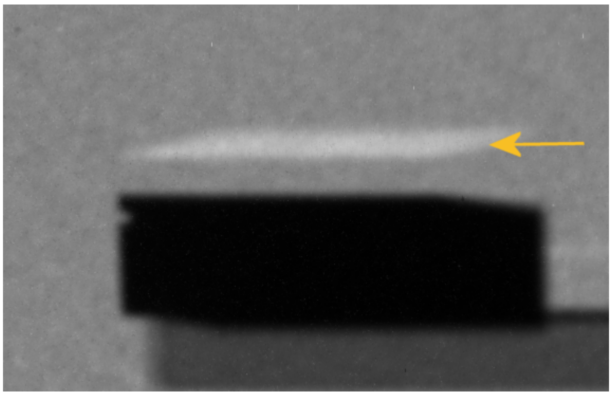

Figure 1.6: NR of a neutron super mirror (black) shows a 30% higher flux (arrow) 5 mm above the reflecting surface

$\Sigma = \Sigma(E)$. A measured attenuation coefficient $\bar{\Sigma}$ for a given neutron spectrum $\phi_{spectrum}$ is averaged according to:

$$\bar{\Sigma} = \frac{1}{\phi_{spectrum}} \int_{spectrum} \Sigma(E)\, \phi_{spectrum}(E)\, dE \tag{1.5}$$

In the cold and the thermal energy regime $\Sigma(E)$ is proportional to $1/\mathrm{v} \propto 1/\sqrt{\mathrm{E}}$ (Fig. 1.7) for most materials. That means low energy -slow or cold- neutrons are attenuated stronger.

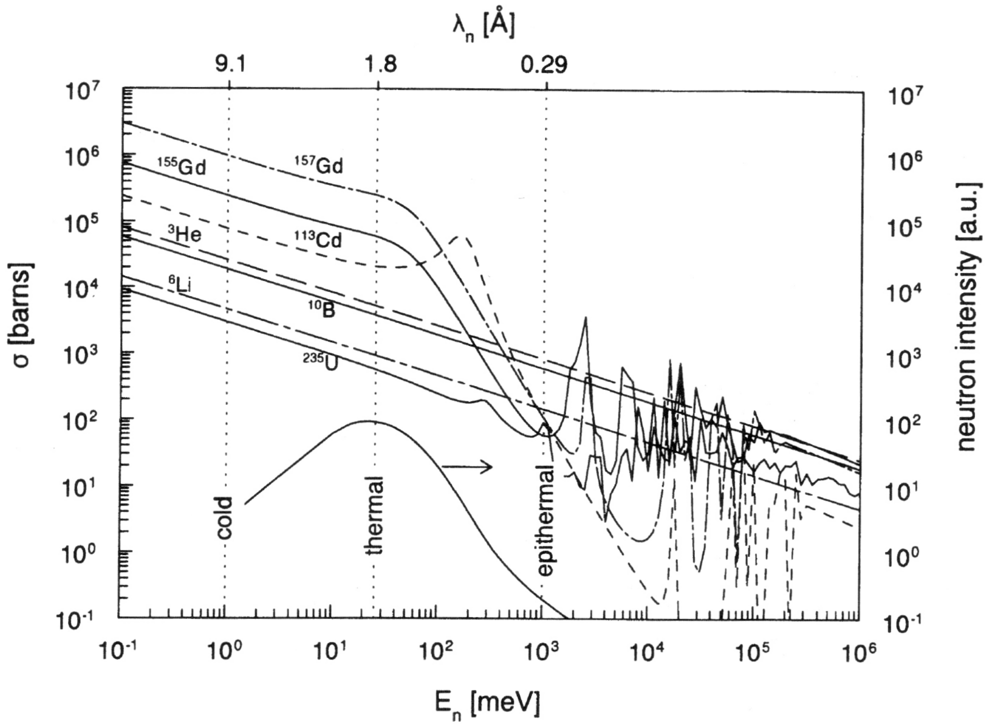

Figure 1.7: The $1/\sqrt{\mathrm{E}}$ energy dependence of the total neutron cross section with nuclear resonances at higher neutron energies

The strong attenuation of cold neutrons signifies that they are attenuated first in thicker samples. With increasing penetration depth the neutron energy spectrum shifts towards higher energies resulting in a smaller attenuation. This effect is called beam hardening. The attenuation coefficients for cold neutrons were measured in an experiment at FRM-II for iron, aluminium, lead and graphite from a NR image of step wedges with a known thickness (see Fig. 1.8, left). The decreasing attenuation coefficient of iron (black line) clearly proves the spectral effect of beam hardening (see Fig. 1.8, right).

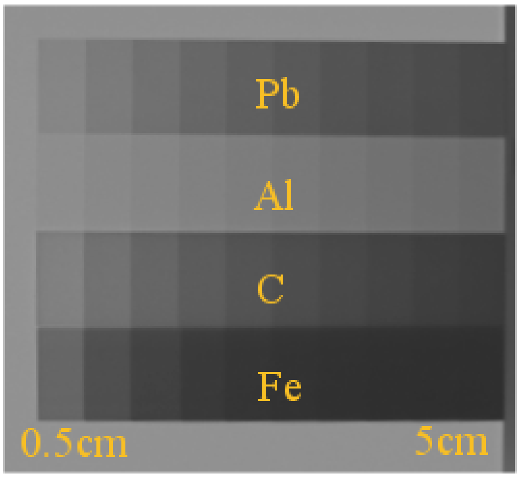

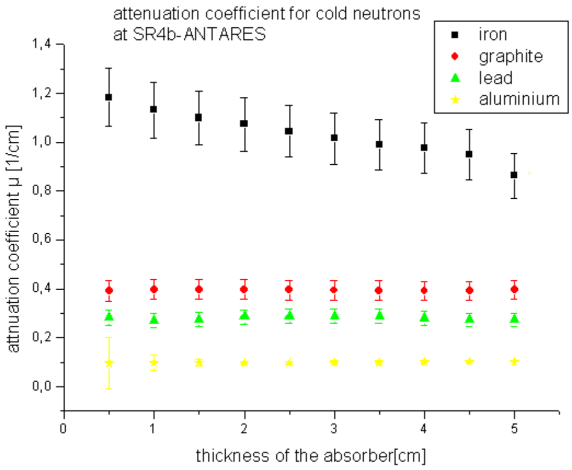

Figure 1.8: NR(left) of step wedges, calculated mean attenuation coefficients (right), iron shows beam harding

Other spectral effects at lower energies appear in crystalline materials (see Fig.1.9). The neutron cross section shows sharp edges, so called Bragg cutoffs, at determined wavelengths. The explanation for this is the coherent elastic scattering mechanism on the atomic lattices of crystallites in microcrystalline materials.

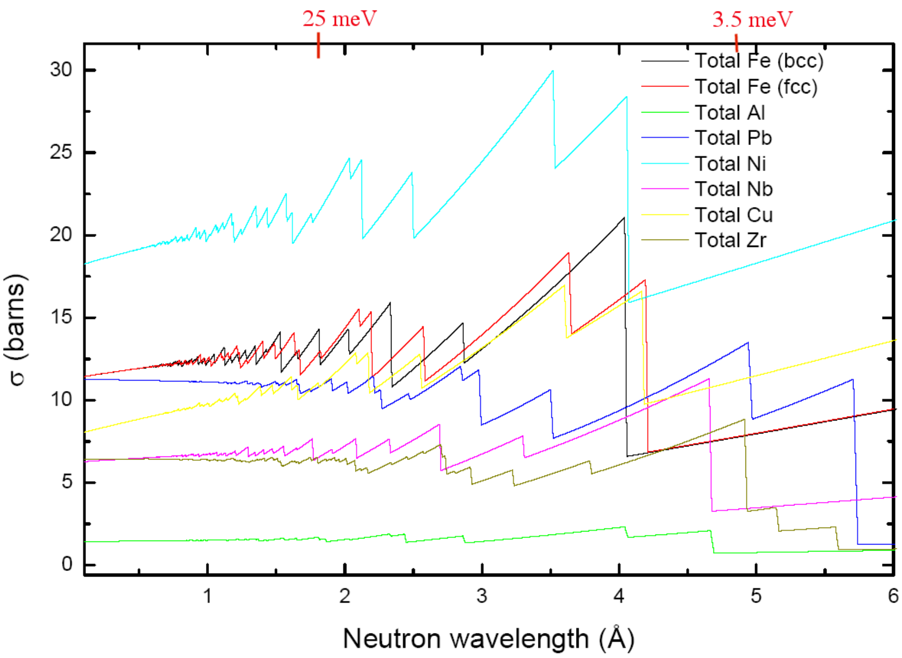

Figure 1.9: Coherent neutron cross section of different materials at large wavelengths, from [San01, 5]

In poly-crystalline materials many orientations exist and neutrons with wavelengths below the lattice spacing are scattered out of the beam. If $\lambda/2$ exceeds the lattice spacing the transmitted intensity increases significantly (see Fig. 1.10). In this way every crystalline material shows a characteristic fingerprint of its lattice type and its lattice parameters. The principle of neutron diffraction can be combined with the macroscopic spatial resolution of neutron imaging. Using neutrons of a defined energy this characteristic structure in the attenuation gives us a chance to distinguish between materials.

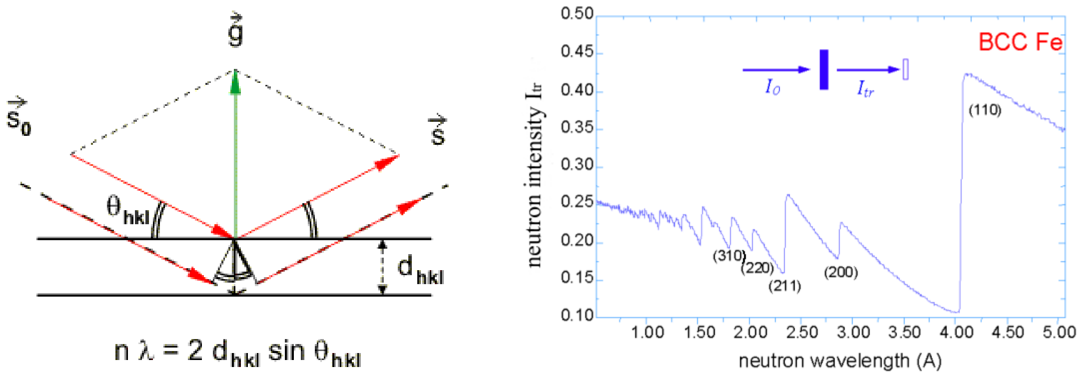

Figure 1.10: Scheme of the Bragg law (left), energy dependent neutron transmission curve of iron (right), [San01, 5]

1.5 Monte Carlo Simulations

Neutron transport can be described more precisely using the transport equation. This differential equation can be solved by Monte Carlo Simulations. After the definition of the exact geometry, the source and the detector, randomly shuffled neutron trajectories are calculated using the energy dependent neutron cross sections for all possible targets. In the sum it is possible to draw a conclusion about the total neutron flux. Monte Carlo Simulations are an indispensable tool for complex problems like the calculation and optimization of nuclear instruments.

Chapter 2

Experimental setup for neutron imaging

The experimental setup for NR imaging consists of three main components: A neutron source including the beam defining components providing the neutron beam, a position sensitive NR detector and the object of investigation. This chapter gives an overview of neutron sources and NR detectors, with a focus on the ANTARES setup at FRM-II. Finally the most important image parameters are discussed.

2.1 Neutron source

Neutrons for imaging experiments are usually extracted from a moderator of a spallation source or a reactor by means of beam tubes and guides. The velocities of the neutrons follow closely a Maxwell-Boltzmann distribution:

$$P(v)dv = 4\pi \left(\frac{m}{2\pi k_B T}^{\frac{3}{2}} \right) v^2 e^{-\frac{mv^2}{2k_B T}} dv \tag{2.1}$$

The maximum of $P(v)$ is at $E = \frac{1}{2}mv^2 = k_B T$. This relation explains the classification hot, thermal and cold neutrons, referring to the moderator temperature T corresponding to a 2000 K hot graphite moderator, water with 320 K or liquid deuterium with T≈30 K. Further we can distinguish between continuous and pulsed neutron sources. Accelerator based spallation neutrons sources guide an intense pulsed proton beam on a spallation target. In the target neutron pulses are produced by a nuclear spallation reaction and are moderated afterwards. The neutron spectrum at the sample position in a certain distance from the moderator is time dependent and called a time of flight spectrum. Nuclear reactors in contrast are continuous neutron sources producing neutrons by a nuclear fission reaction in the reactor fuel elements.
The low refraction index of neutrons favors a quasi parallel beam geometry for imaging. Such beams are optimized for two criteria, which compete with each other: a high flux and a low divergency. At today's neutron radiography facilities the thermal or cold neutron flux is up to 10^8 to 10^9 n/cm^{2}s at the sample position. This is five orders of magnitude less than for typical X-rays sources. The synchrotron beam at the ID22 beam line at European Synchrotron Radiation Facility ESRF, Grenoble, France for instance is focused on an area of about 3.5 x 1.5 μm^2 with a flux up to 10^{12} ph/s between 6.5 and 18 keV. Thus, even at high flux neutron sources the precision of the I/I$_0$ measurement is determined by the limited neutron flux. Typical exposure times for single NR images are in the range between 100 and 1000 ms.

The divergency of a neutron beam is normally defined with the L/D ratio, where D is the diameter of the collimator and L is the distance between object and collimator. At modern facilities it is at least above 100. A low beam divergency (and a high L/D ratio) is realized with a long distance L from the source to the object at the cost of a lower neutron flux according to the $1/L^2$ law. If the distance between object and detector l is large, the beam divergency affects the image sharpness. A point in the object is blurred in a spot of size d=l/(L/D) in the corresponding image, where l is the distance between object and detector (Fig.2.1).

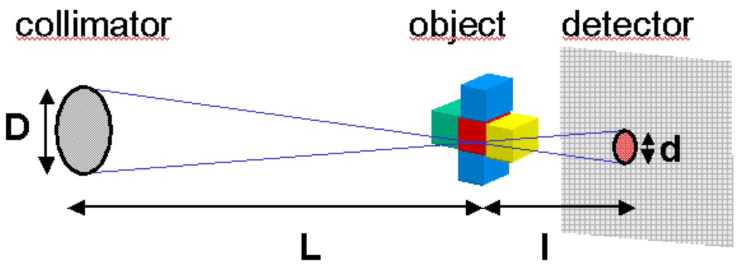

Figure 2.1: Beam divergency and spatial resolution

2.1.1 The neutron radiography facility ANTARES at FRM-II

In the following the ANTARES facility (Advanced Neutron Tomography and Radiography Experimental Setup) at the high flux research reactor Forschungsreaktor München II, FRM-II, is presented (Fig. 2.2).

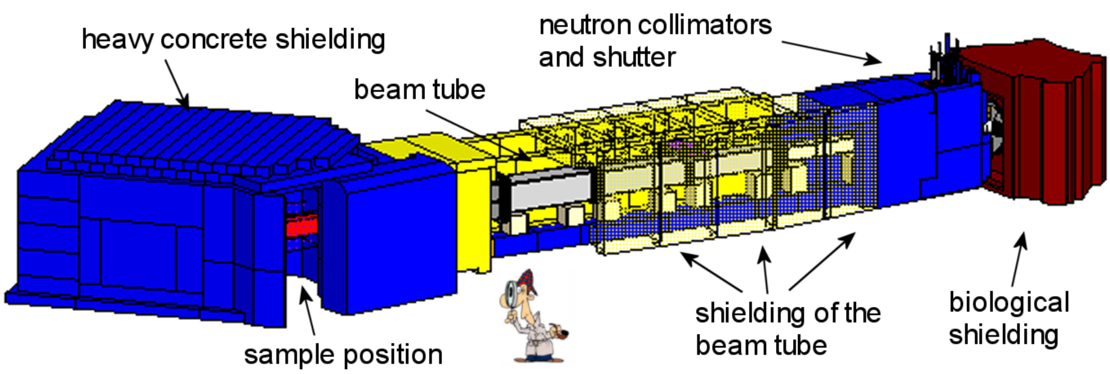

Figure 2.2: Shielding of the tomography facility ANTARES

A detailed study including Monte Carlo Simulations of every individual component is given in [Gru05, 17]. The neutron source FRM-II is a fission reactor with a compact core fuel element of highly enriched uranium, which emits neutrons with a typical fission spectrum. In the liquid D_2O moderator tank a quasi-isotropic thermal flux is generated by moderation. In the thermal flux maximum 20 cm outside the fuel element the cold source, a liquid D_2 bottle at 25 K, is positioned and moderates the thermal neutrons further down to a cold spectrum. The neutrons are extracted by the ANTARES beam tube SR4 and reach the sample position through a flight tube. Shutters allow an opening and closing of the neutron beam within some seconds. The neutron collimator with the diameter D and its distance L to the sample position defines the divergency of the quasi parallel beam geometry with the ratio L/D.

In Fig. 2.3 the beam geometry is sketched in more detail with some additional beam parameters. The distance L=17.31 m and L=16.7 m between collimator and detector for respective collimator diameters of D=4.3 cm and D=2.1 cm are available. The respective L/D ratios are 400 and 800.

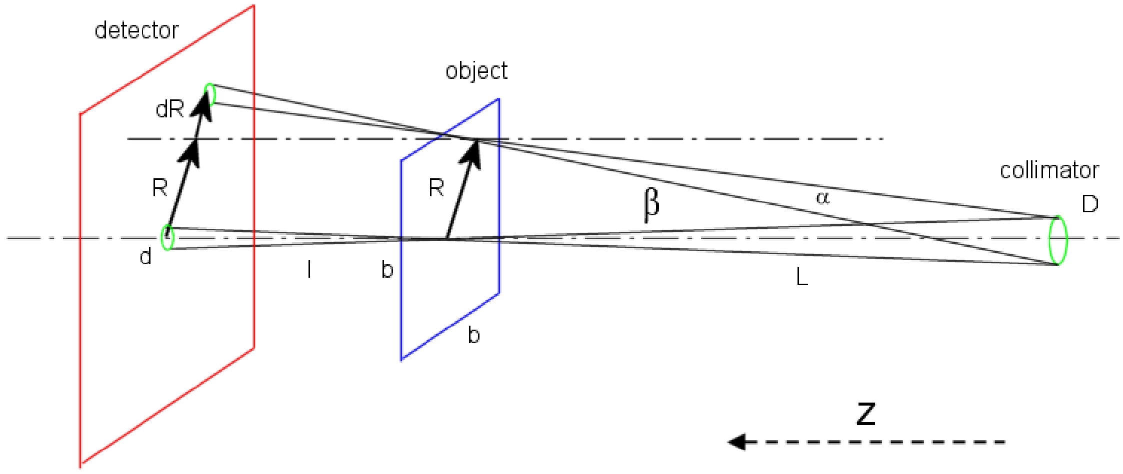

Figure 2.3: Scheme of the neutron beam at ANTARES

At the sample position (18.4 m from the biological shielding of the reactor) the beam diameter is 40 x 40 cm^2 and the neutron flux is $1.02 \cdot 10^8$ n/cm^2s and $2.6 \cdot 10^7$ n/cm^2 s. The neutron flux was measured with a precision of a few percent. One point of the object is mapped onto a spot of the size d=l/(L/D) on the detector, where l is the distance between object and detector. The larger the distance from the optical axis and the larger the distance between object and detector the bigger is the displacement, dR=l·R/L. Further parameters are listed in Table 2.1.

	large collimator	small collimator
L/D	400	800
L'[m] distance tube-nose collimator	3.69	4.3
D[cm]	4.3	2.10
L[m]	17.31	16.7
α[°]	0.14	0.07
β(R)[°]	0.14·R/(b/2)	0.07·R/(b/2)
Neutron flux at sample position[n/cm^2s]	$1.02 \cdot 10^8$	$2.5 \cdot 10^7$

Table 2.1: ANTARES beam parameters

The neutron spectrum is in the cold regime, but not fully moderated and therefore not perfectly corresponding to a Maxwell distribution. It can be approximated best with a Maxwell spectrum at T = 42 K (see Fig. 2.4). The blue points connected with the black line are the neutron spectrum on the sample position simulated by [Gru05, 17], the red line is the best fit. The flux maximum of that neutron spectrum is at a wavelength of 4.8 Å, corresponding to a neutron energy of 3.5 meV and a neutron velocity of 884 m/s, to pale in comparison with 25 meV, 1.8 Å and 2300 m/s at the thermal maximum.

The stability of the neutron flux was studied with a series of open beam images at a time scale of about 10 seconds. A comparison between the image brightness in four

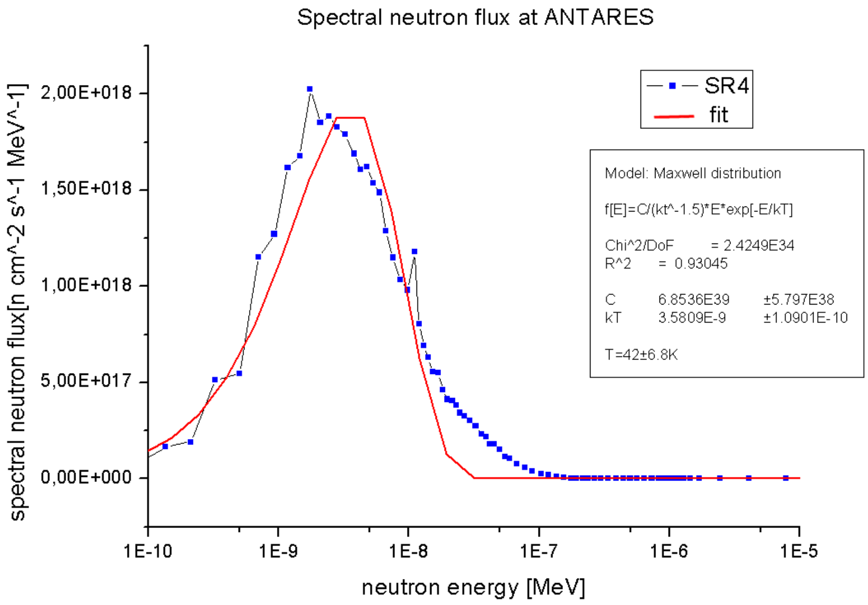

Figure 2.4: Neutron spectrum of the ANTARES facility

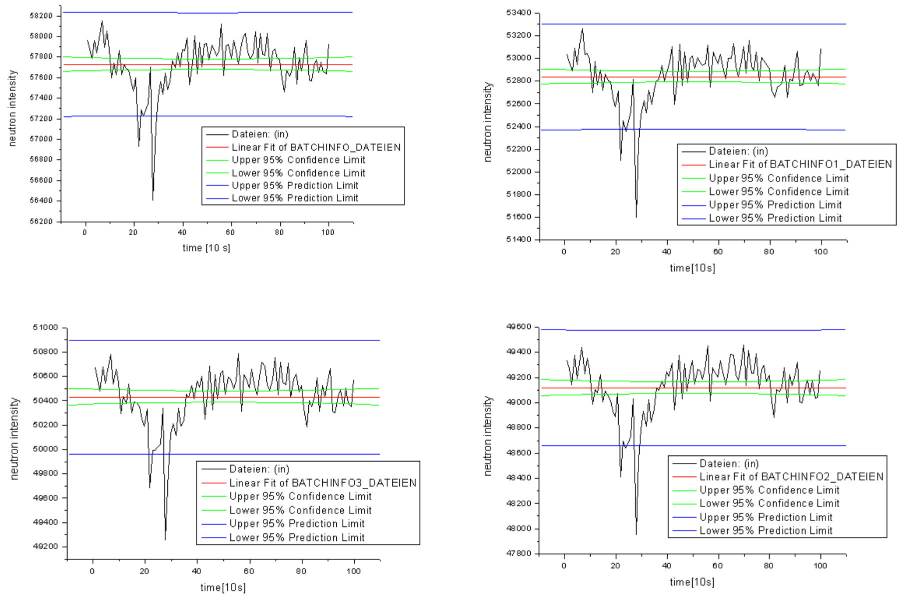

Figure 2.5: Neutron intensity fluctuations at four different areas in the ANTARES beam

different areas of beam revealed that the beam fluctuations are in the range between 0.4 and 0.5% (see Fig. 2.5) due to the movements of the control rod. As a consequence in the case of precise measurements these beam fluctuations must be corrected. At spallation neutron sources the beam fluctuates much stronger due to the proton beam fluctuation and sometimes even a complete beam breakdown can happen.

2.2 Neutron radiography detectors

A NR detector measures a two dimensional image of the neutron flux transmitted by an object. Requirements for such a system are:

- high detection sensitivity
- high spatial resolution
- high time resolution (a short gating time)
- short cycle times between the images (a short readout time)
- good linearity
- large dynamic range
- low noise level
- large detector area
- the availability of the images in digital form

Among the multitude of available detector types like conventional film, image plates, Si based flat panel detectors, GEM foils or ^{3}He counting tubes one detector is most spread in the NR community: The NR detector based on the combination of a neutron to light converter plate and a CCD camera (Fig. 2.6).

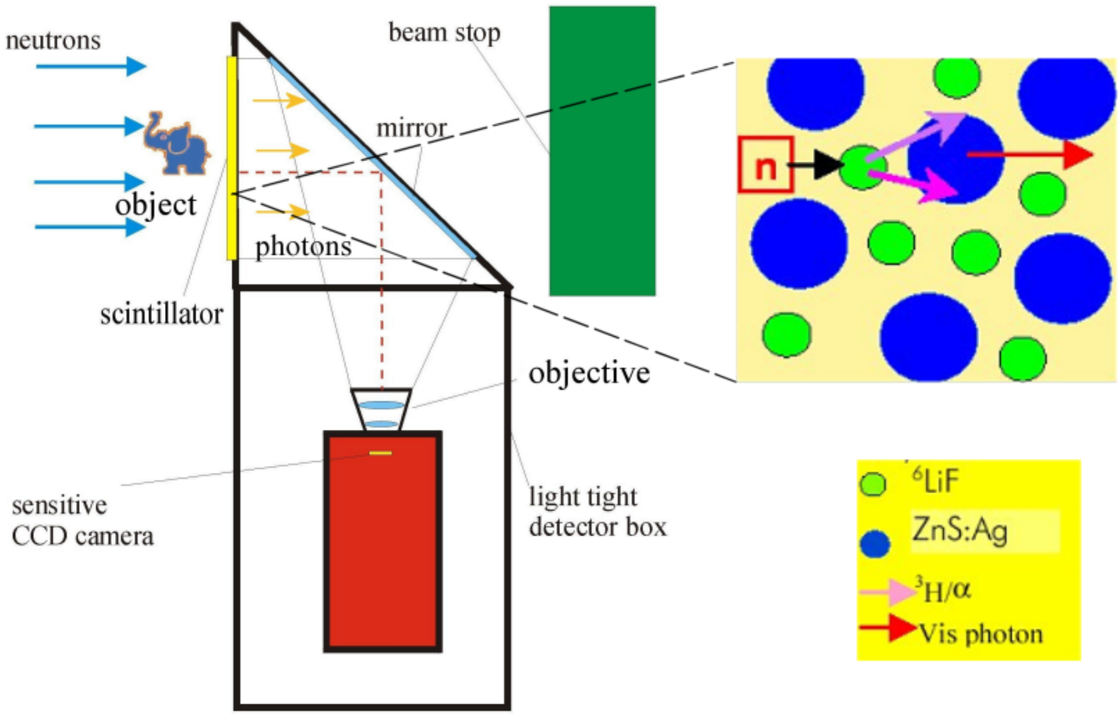

Figure 2.6: Scheme of a NR detector and neutron conversion principle

Neutrons induce a (n,α)-reaction in the ^{6}Li. The reaction products ionize the scintillation material, which recombines by emitting visible light in 4π. A sensitive CCD camera detects the low neutron induced photon flux (Fig. 2.6). With the help of a mirror the camera does not have to stay in the direct beam and can not get damaged. A light tight box prevents light incidence from outside.

The detection properties of this kind of detector are determined by the used scintillator, the camera optics and mainly by the used CCD camera.

2.2.1 Scintillators

Most NR groups use NDg (formerly known as NE426) scintillator plates of ^{6}LiF/ZnS produced by the company Applied Scintillation Technologies (AST). The neutron detection reaction in these plates is: $^6\text{Li}+\text{n} \rightarrow {}^3\text{H}+{}^4\text{He}+4.79$ MeV

The Tritium nucleus ^{3}H and the α particle (^{4}He) have a high kinetic energy of 4.79 MeV.

According to the Bethe-Bloch-law the charged particles are stopped in the scintillator material exciting the ZnS grains, which then emit green or blue light depending on the dopants. The mean range of the reaction products in the scintillator define the lower limit for the spatial resolution of a neutron radiography detector. The efficiency of the scintillator is determined by the high cross section of ^{6}Li and is in the 20% range for the 300 μm thick standard scintillator. Similar scintillators emit in the average $1.77{\cdot}10^5$ photons per detected neutron. The spatial resolution is determined by the grain size and the thickness of the scintillator. Recently the spatial resolution and relative efficiency of such a converter plate were measured for cold neutrons by [Bac02, 13]. For a 100 μm thick scintillator the spatial resolution was 240$\pm$10 μm with a 36% loss in efficiency in respect to a usual 300 μm scintillator with the highest efficiency and a spatial resolution of 540 μm. Scintillator are never completely homogenous (Fig. 2.7), but that is not so disturbing if the data is normalized. The time resolution of the scintillator is given by the decay time of the excited states of the material. The light intensity decays to 10% within 85 μs according to the data sheet of the company AST [Ast04, 11]. In future glass scintillators [Ciz99, 7] seem to be promising candidates for dynamic neutron imaging. They have better decay properties and a higher detection efficiency of 90% at the cost of a lower light output.

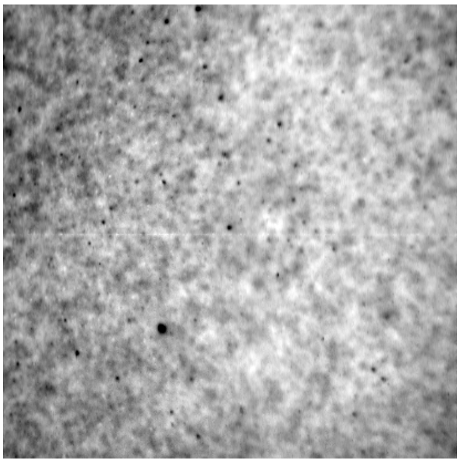

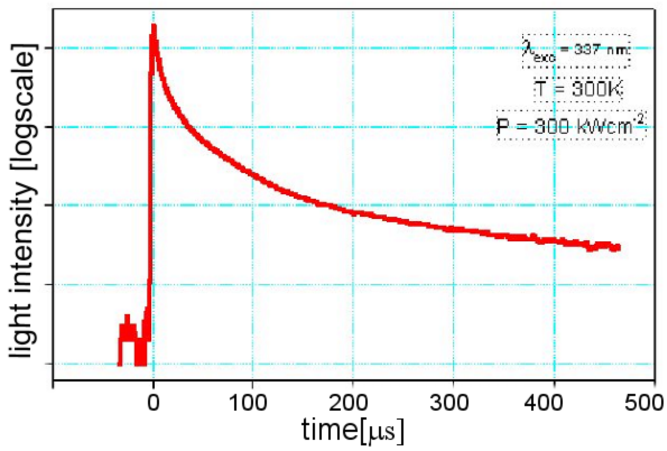

Figure 2.7: Structure of the scintillator (left): an area of 1.1 x 1.1 cm^2 with fluctuations up to a few % in brightness; decay curve of neutron induced scintillation light (right) [Ast04, 11]

At the Neutrograph facility, Institute Laue Langevin (ILL), Grenoble, France, at NEUTRA facility, Paul Scherrer Institut (PSI), Villigen, Switzerland and at KFKI research institute, Budapest, Hungary the scintillator degradation with time was observed. It was found that the organic binder of the scintillator looses its transparency for light depending on scintillator thickness. According to [Hil05, 6] the scintillator efficiency decreases with every hour of irradiation with neutrons at the thermal neutron beam with the high flux of $3{\cdot}10^9$ n/cm^{2}s by 4%. That would correspond to a degradation of 0.23%/hour and 0.03%/hour at ANTARES for the large and the small collimator. Because of the cold spectrum at ANTARES the degradation rates are expected to be higher. Measuring open beam images during large NR series these artefacts can be quantified and corrected more easily.

2.2.2 Detector optics

The optics between scintillator screen and the camera chip or the entrance window of the image intensifier has to perform the following task: Depending on the object size an area up to 30 x 30 cm^2 on the scintillator has to be mapped onto the chip area A. Since the scintillation light is emitted into 4π, only a small fraction of the light reaches the chip: $A/(4\pi d^2)$. That is why a small distance and a big aperture is the best for a high efficiency mapping. Objectives are chosen by their focal length f and their aperture. Standard objectives have a focal length of 50 mm and a viewing angle of 12°, macro objects with f = 28 mm and f = 16 mm a viewing angle of a 25° and 45°. Going to macro objectives one should keep in mind some possible aberrations and distortions. For short distances to the object plane and large angles from the optical axis the image gets darker, blurred and distorted. This results from the increasing distance to the focal sphere and increasing areas seen at large solid angle. Mostly barrel like optical distortions (some mm in the corners) and lower brightness in the corners of the image due to angles of more than 40° are visible. Spherical aberrations can be avoided at the cost of lower light intensity by reducing the aperture. If the camera to scintillator distance is variable by means of a translation table, the field of view can be adjusted best to the object size.

2.2.3 CCD cameras

The CCD camera is the core part of a NR detector and responsible for most detector parameters. The principle of a Charge Coupled Device (CCD) is shortly discussed.
Every pixel of a CCD chip consists of an array of Metal Oxide Semiconductor (MOS) capacitors. If on the metal contact of a MOS capacitor a positive voltage is applied, in the depletion zone on the oxid semiconductor interface charge can be storaged. Charge is generated by incident light due to the photoelectric effect and by thermal excitation. By cooling the device the fraction of thermal induced charge is negligible for short integration times. In a periodic array of such electrodes the charge can be shifted from one pixel to the next by varying the applied voltages (see Fig. 2.8).

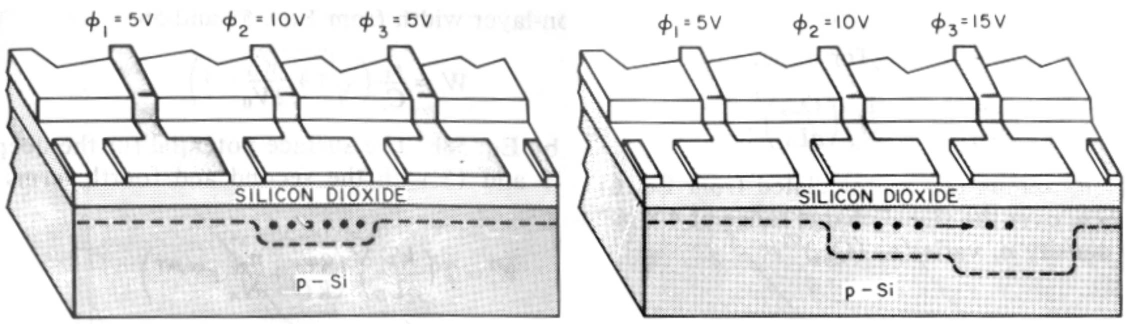

Figure 2.8: Charge transport in a CCD pixel

After every charge shift to the next pixel the charge distribution of the pixel row at the chip border is moved into a serial register. From the serial register the charge is transferred to the read out amplifier, which converts it into a voltage and amplifies it for data processing. After digitalization of the image it is stored on hard disc. Finally the grey level of each pixel in the NR image corresponds to the amount of charge collected in the potential well. In the case of a NR detector the amount of light emitted by the scintillator area corresponding to a CCD pixel is proportional to the number of neutrons detected on this area. Thus, the grey level in the NR image is proportional to the detected neutrons.

A CCD can be characterized by the following physical parameters:
- the quantum efficiency
- the chip size
- the gating times

- the frame rate
- the noise
- the linearity

The CCD camera properties strongly affect the NR image and determine the possible application. For the new methods developed within this work the time resolution, or more exact the shutter options of modern CCD cameras are essential. While the time resolution is determined by the neutron flux (it is typically between 100 and 1000 ms), the number of images one can acquire per time is given by the frame rate of the detector. Since the frame rate depends on the number of pixels and on the readout frequency of the CCD, typical values for a 1k x 1k pixel CCD chip with a readout frequency of 1 MHz is around 1 Hz and a complete readout takes 1 second. Processes with a time scale of minutes can be investigated well in real time. However, periodic processes down to 100 μs can be examined by stroboscopic neutron imaging. A triggered detector is synchronized with the repetitive process and neutrons of identical time-windows of the cycle are accumulated. By phase shifting the triggering signal of the process different time windows in the cycle can be selected and a movie can be composed. We have examined LCD shutters, interline transfer CCDs, CCDs with a gated image intensifier and shuttered CCDs.

2.2.3.1 LCD shutters

LCD shutters work by rotating the polarization of light between two perpendicular polarizers (Fig. 2.9). New Ferroelectric Liquid Crystal (FLC) shutters offer exposure times down to 0.2 ms, but their state transition time is in the order of 70-100 μs [Dis05, 8]. The cell requires some recovery time, so it cannot be run with a 50% duty cycle.

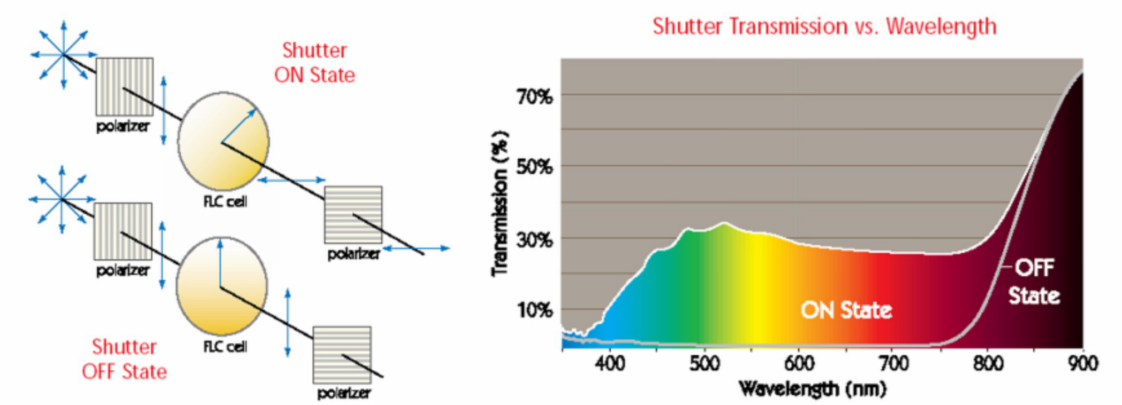

Figure 2.9: Working principle and transmission of a FLC shutter [Dis05, 8]

More important are the transmission and opacity values in the open and closed state, given in the order of 30% and 0.05% (Fig. 2.9). While these values look good at first, they may be sufficient for a pulsed spallation source, but insufficient for the continuous illumination of a reactor source. An engine running at idle 1000 rpm will rotate with 16.7 Hz. Given a time window of 1 ms, the shutter will roughly be open 16 ms, but closed for 984 ms under continuous illumination. The ratio between image signal and background is (16 x 30%) / (984 x 0.05%) = 9.8, so the useful image signal is only ten times the background signal and will be nearly drowned out by the transmission during closed time. In the case of a spallation source, the pulse length is spread out to a few milliseconds, with intensity rapidly dropping towards longer wavelengths and flight times, so the application of LCD shutters may be feasible, but we dropped them for continuous sources.

2.2.3.2 Interline transfer CCDs

For conventional full area CCDs, the light flux either has to be shut off for readout after integration time, or - in the case of frame transfer CCDs - the transfer time to the image storage area has to be short compared to the exposure time. Full area CCDs are not feasible for below-millisecond exposure times without an external shutter. For Interline transfer CCDs the CCD chip area consists of alternate light sensitive pixel columns and masked vertical shift registers. Image information from the light sensitive pixels can be transferred into the masked, light-insensitive shift register with a single clock cycle, then be read out consecutively through the readout registers (see Fig. 2.10).

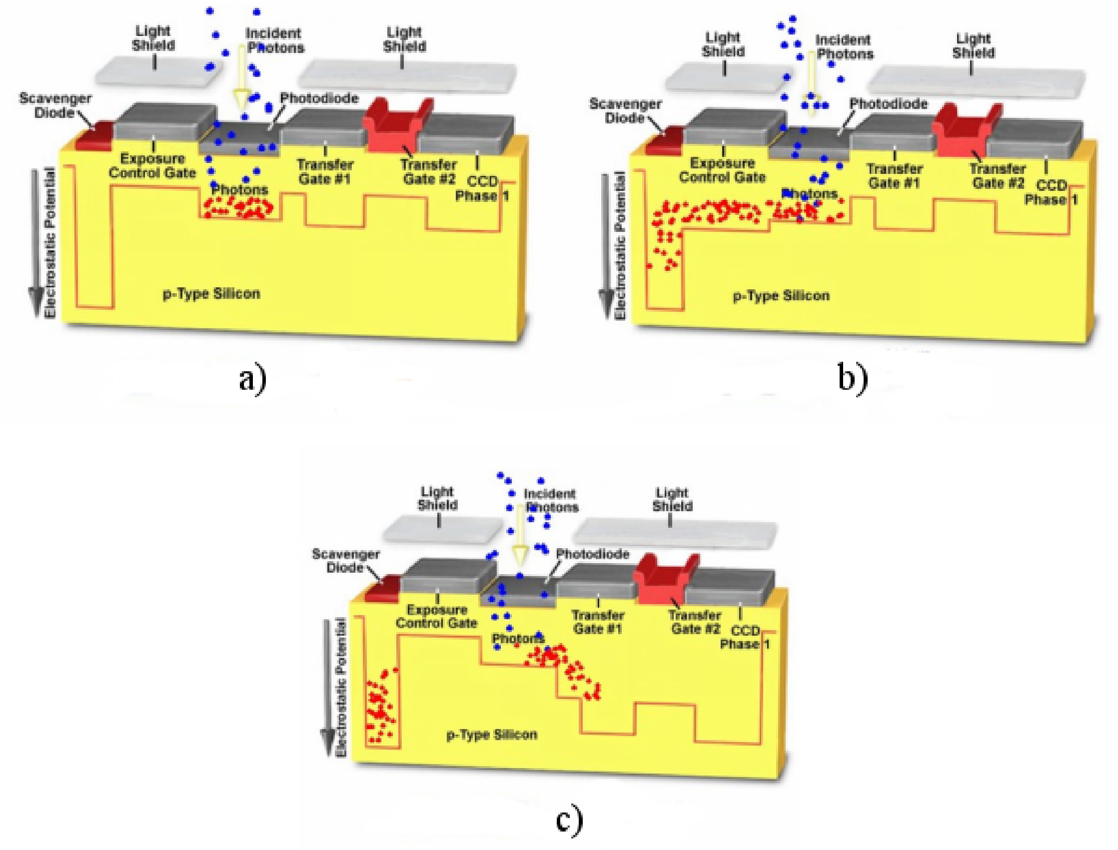

Figure 2.10: Cut view of an interline CCD: a) charge collecting mode, b) shuttered mode, c) charge transfer mode [Oly05, 9]

Photo electrons are collected in the potential well below the light sensitive pixel area. This area is sided by an exposure control gate and a transfer gate (see Fig. 2.10). If the exposure control gate is clocked high, the potential well below the light sensitive pixel is extended towards the even deeper well of a scavenger diode line. All collected photo electrons are immediately drained away, which effectively serves as a shutter (see Fig. 2.10 a)). The CCD collects photo electrons only if the exposure control gate is clocked low, forming a barrier between the pixel and the scavenger diode and controlling the exposure time (see Fig. 2.10 b)). If the opposite transfer gate is clocked high, the collected charge is transferred into the vertical transfer register (see Fig. 2.10 c)). After clocking the transfer gate low again, the collected charge in the transfer register is transferred into the horizontal readout register (perpendicular to the cut view here). The big advantage of the interline CCD is that no additional noise is introduced by an image intensifier, that it can be shuttered on the chip itself, and that the process of short-time exposure and charge transfer into the transfer register can be repeated several times before the charge has to be moved to the readout register. The disadvantage is that - even with very low light levels - the low pixel full well capacity limits the number of on-chip accumulations to a few dozen times, which is not sufficient for stroboscopic imaging. Further integration can only be performed off-chip in the computer, but the images to be summed up suffer from readout noise and from digitization error if their intensity is very low. Such a camera system is successfully employed by the radiography group at the ILL.

2.2.3.3 CCDs with image intensifier

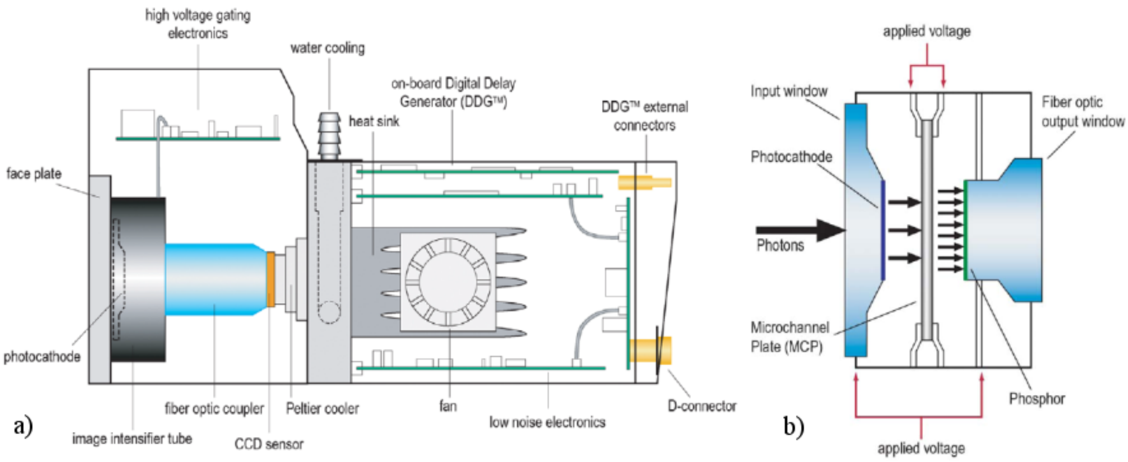

Figure 2.11: a) Intensified CCD camera (Andor Technology), b) image intensifier scheme

Image intensifiers are light amplifying devices coming originally from military night vision equipment. By putting them in front of a CCD, low level light measurements are possible. A photon flux amplification up to 10^8 and even single photon detection becames possible with the latest generation image intensifiers. An image intensifiers consists of an evacuated tube comprising a photo cathode, a micro channel plate (MCP) and a phosphor screen (Fig. 2.11). The photo cathode is coated on the inside surface of the input window. When a photon strikes the photo cathode, a photoelectron is emitted and drawn towards the MCP by an electric field.

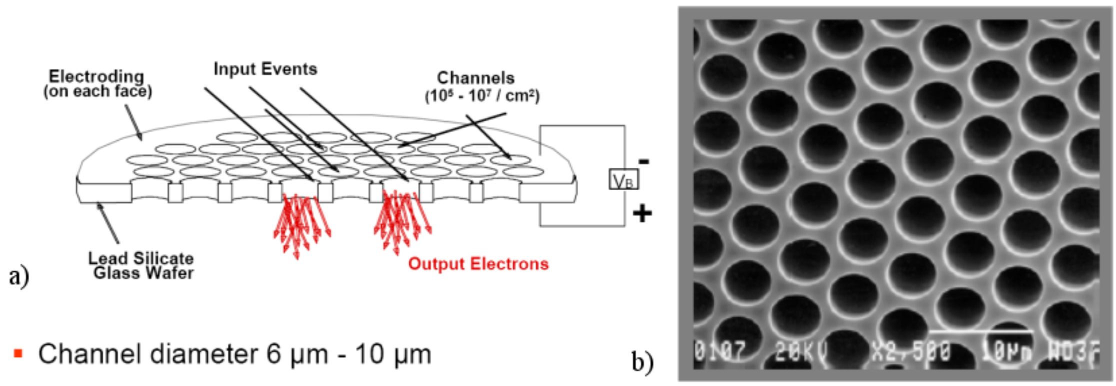

Figure 2.12: a) Scheme of a MCP, b) Microscopy image of a MCP

The MCP (Fig. 2.12) is a 1 mm thin glass disc with a honeycomb of typically 10

μm fine channels, each with a resistive coating. A high potential is applied across the MCP, enabling the photoelectrons to slowed down one of the channels of the disc. When a photoelectron has sufficient energy, it dislodges secondary electrons, which in turn undergo acceleration which results in a cloud of electrons exiting the MCP. The degree of electron multiplication 2.13 depends on the gain voltage applied across the MCP. By cascading MCPs up to 4 times the amplification can be further increased. The voltage across the MCP can be gated very fast down to ns time scale, which makes ICCD cameras very interesting for many spectroscopy applications.

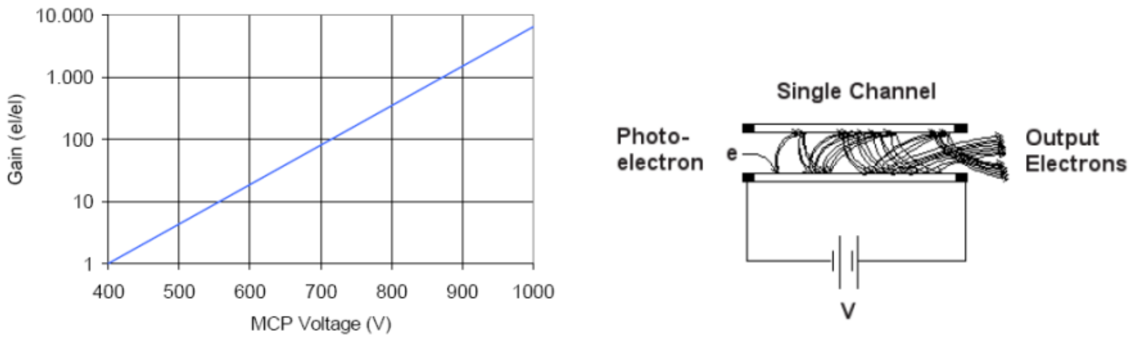

Figure 2.13: Electron multiplication in a single MCP channel

The noise is quantified in the so-called noise factor $N_f = SNR_{in}/SNR_{out}$, the signal to noise ratio before and after the intensifier. The SNR is best with maximal gain, but the dynamic range decreases for one image. The dynamic range of a detector can be expanded with multiple readouts and summing images after acquisition. But even if the readout noise is negligible, the required readout time is not. Thus, for a limited beam time, it is advisable to reduce the gain in order to improve dynamic range and to get in consequence a lower number of readouts and better neutron statistics.

2.2.3.4 Shuttered CCDs

A completely different type of electronic on-chip shutter was developed for tasks like controlling adaptive optics in telescopes or tracking rocket launchers [Rei93, 10]. This technique works on back-illuminated CCDs, which means that the CCD chip is etched very thin down to a few ten micrometers and is illuminated from the backside opposite the gate electrodes (see Fig. 2.14).

The light sensitive area is flanked by two drain electrodes which serve as channel stops between pixels. Using layers of different doping, a permanent potential well is formed below the gate electrode of the light sensitive pixel within the silicon chip. By applying a positive potential to the gate electrode, this potential well can be extended to the opposite surface of the CCD to collect photo electrons in the open mode. If a negative voltage is applied to the drain electrodes, a repulsive potential is formed below the drain electrodes. Due to the varying doping below the pixel area, the potential well is compressed but not eliminated until the remaining potential well is pinched off from the lower chip surface, effectively shutting it off from generated photo electrons. This method works best for short wavelength light, because the range of incident short-wavelength photons in the silicon is much smaller than for longer wavelengths. The measured extinction ratio is greater than 75000, the switching time below 55 ns. By varying the negative voltage on the drain electrodes, the pinch-off can also be regulated from zero to full, controlling the amount of photo-electrons reaching the potential well and thus the sensitivity of the device.

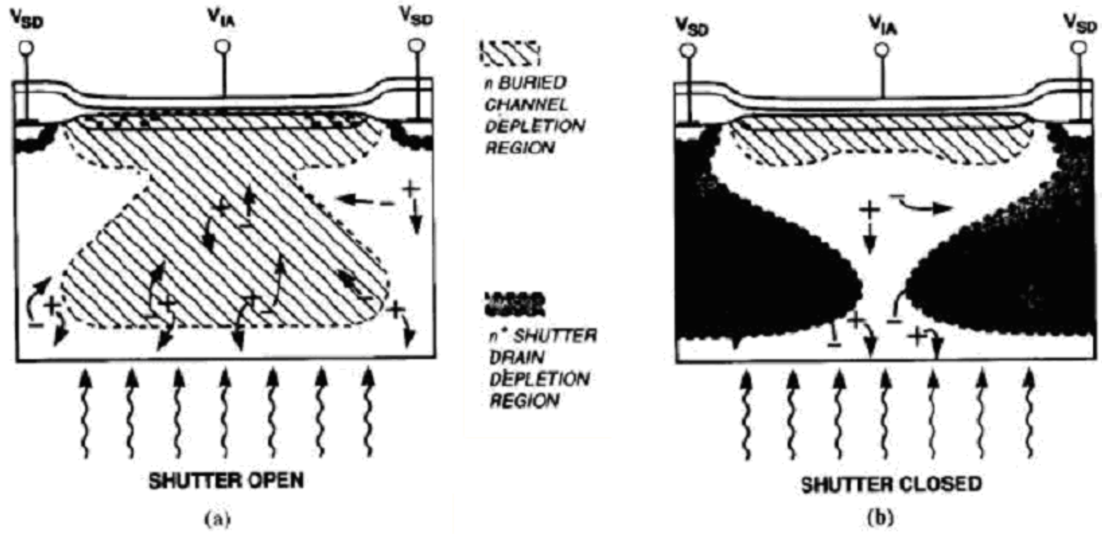

Figure 2.14: Single back-illuminated pixel in a CCD with electronic shutter showing the potential well of the pixel and the repulsive potential of the shutter drains with a) shutter open and b) shutter closed [Rei93, 10]

2.2.4 The NR detector at ANTARES

Fig. 2.15 shows the NR detector at the ANTARES facility. It is a detector box with a 200 μm thick NDg neutron scintillator screen of 26 x 26 cm^2 and a CCD camera on a translation table. Depending on the object size the objective and the distance to the scintillator are chosen. Two cameras types are at disposal:

- The peltier cooled Andor CCD camera DW 436 with a large chip of 2k x 2k pixels and a chip size of 26.7 x 26.7 mm^2 is preferred when high spatial resolution is needed. Due to the large chip the readout time for a full frame is 4 s at highest readout speed. The minimal accumulation time of 30 ms is limited by the fast shutter. The quantum efficiency of 95% and the noise properties of the CCD are very good. The camera manufacturer guarantees a linearity of 1% over the dynamic range of 16 bit (65535 grey levels).

- The intensified CCD (ICCD) camera DH 734 is especially useful for stroboscopic NR measurements. The peltier cooled chip with a chip size of 13.3 x 13.3 mm^2 and 1024 x 1024 pixels is coupled to a multi channel plate by fiber optical coupling. With the MCP gating times down to ns can be reached and an external trigger input allows synchronization with an external process. The quantum efficiency of the CCD chip is 15% but single photon and single neutron detection become possible because of the high light amplification factor of the MCP. The amplification factor is adjusted by the MCP gain. If it is too high the dynamic range of 16 bit is drastically reduced.

In near future a high speed camera will expand the imaging possibilities and allow real time imaging with ms and sub-ms time resolution.

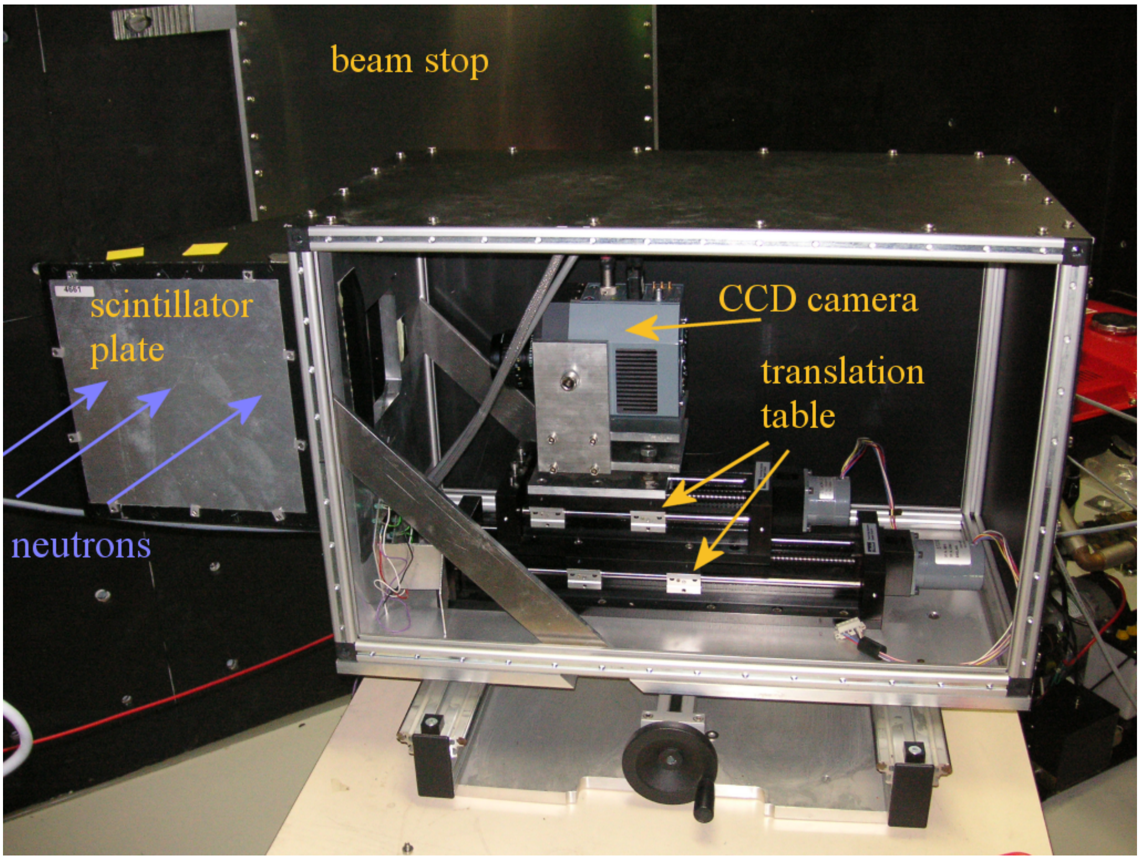

Figure 2.15: NR detector at ANTARES

2.3 The object for neutron radiography and tomography

For the NR the size of the object is relevant in one direction only, the thickness in beam direction. The thickness must be small enough, otherwise the complete neutron flux is absorbed and the NR image is black. If the object thickness is on the limit of zero transmission, the neutron statistics gets poor and the interesting contrasts very noisy. For NT the thickness condition must be fulfilled in the two directions perpendicular to the rotation axis, but tomography with missing angles is a hot research topic. The object details, one wants to see in the inspection, must be bigger than the spatial resolution and must produce a contrast, which the inspector is able to recognize at the given noise level.
The material properties become relevant in form of the neutron mass attenuation coefficient μ_ρ and the density of the object. Differences between constituent individual elements and even isotopes can be detected according to Fig. 1.2. The object must not be too strong attenuating, on the other hand the detail must not be too transparent. Assuming a relative noise $\sigma_\mu/\mu = 1\%$ in the open beam intensity and a background noise σ_{bg} due to the detector of 1% in respect to the open beam signal, the minimal detectable thickness is about $1/250 \cdot \mathrm{L}_{1/10}$ and the maximal thickness one can distinguish from the background is about $2{\cdot}\mathrm{L}_{1/10}$. $\mathrm{L}_{1/10}$ is the length of tenth, the thickness of material, which absorbs 90% and still transmits 10% of the radiation. It can be calculated from the attenuation coefficient μ by the relation:

$$\mathrm{L}_{1/10}[cm] = \frac{ln(1/10)}{\mu[1/cm]} \approx \frac{2.3}{\mu[1/cm]} \qquad \mathrm{L}_{1/2}[cm] \approx \frac{0.69}{\mu[1/cm]} \approx 0.3 \cdot \mathrm{L}_{1/10}[cm] \tag{2.2}$$

The possible thicknesses for the inspection with thermal neutrons are the red bars in

Fig. 2.16 for several materials, the yellow lines on the bars are $L_{1/10}$. For the ANTARES

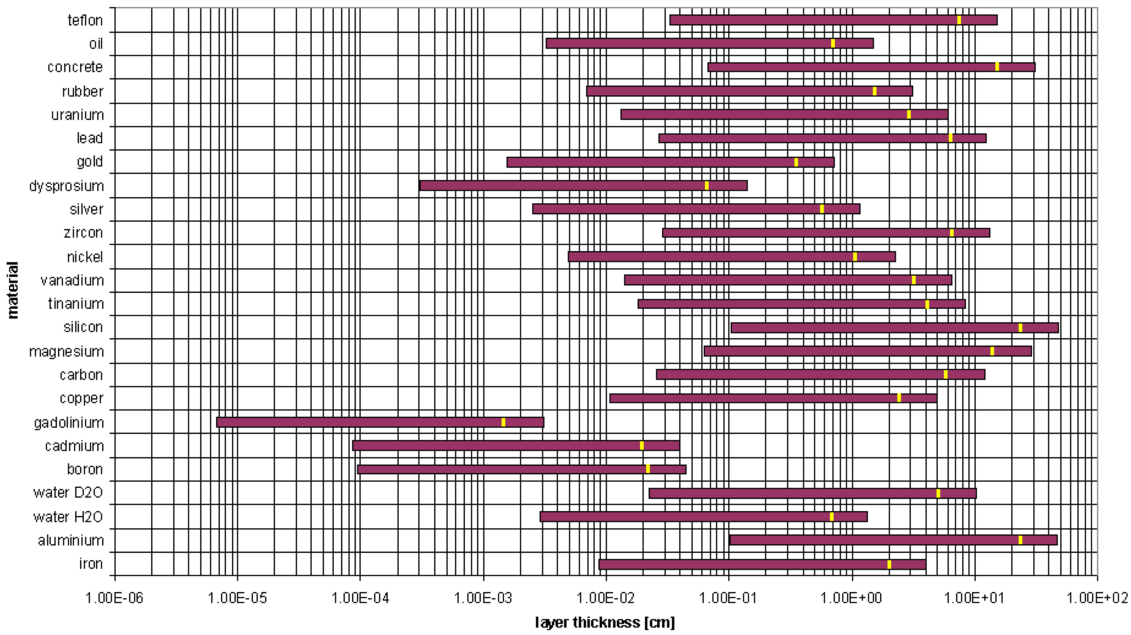

Figure 2.16: Possible object thicknesses for several materials for thermal neutron radiography

facility the attenuation coefficients μ are higher than those in literature based on the thermal spectra. Estimating the change in the attenuation coefficient with the $1/\sqrt{E}$ law and the mean energies of 25 meV at a thermal and 4 meV at the ANTARES facility yields to a larger attenuation coefficient by a factor of 2.5. For a precise comparison the individual spectrum and the energy dependent cross section must be used. As a consequence the contrasts are stronger and the detection of thin materials is improved at the cost of a smaller penetration depth. The scintillator detection efficiency increased likewise with the cold spectrum due to the cross section of ^{6}Li. The average attenuation coefficient μ and the corresponding length of tenth $L_{1/10}$ of neutrons for the ANTARES spectrum were measured for the some materials by using step wedges, see Tab. 2.2. Measuring material thickness and neutron attenuation, the attenuation coefficient was determined. The different thicknesses in a step wedge allow to study the effect of beam hardening. Typically at a thickness of $L_{1/10}$ beam hardening starts.

material	μ[1/cm]	$L_{1/10}$[cm]
Fe	1.12±0.02	2.04±0.04
C	0.29±0.01	5.6±0.35
Al	0.09±0.01	25.40±3.5
Pb	0.27±0.01	8.2±0.4
Cu	1.05±0.02	2.18±0.05
Teflon	0.26±0.02	8.7±0.6
PE	5.11±0.11	0.54±0.01
H_2O	3.6±2.0	0.63±0.3
Oil	4.4±2.5	0.52±0.3

Table 2.2: Measured attenuation coefficients μ and lengths of a tenth $L_{1/10}$ at the cold spectrum of ANTARES

For the measured values of Table 2.2 the scattered neutrons were not considered and especially for H_2O and oil that may lead to deviating results. For the other materials the effect was minimized by the use of a beam limiter. In the case of a dynamic process all the mentioned properties must be fulfilled for a limited irradiation time. The consequence is a shorter bar for the respective sample in Fig. 2.16.
If the irradiation time is long, the sample activation becomes the limiting factor for neutron imaging. Certain nuclei are especially critical for neutron activation and for large irradiation times it is necessary to assure that the mass of critical nuclei in the object is small enough (see Tab. 2.2). The NR facility is optimized for high radiation exposure with strongly neutron absorbing shielding materials, which hardly gets activated. Thus, the major part of the activation comes from the irradiated sample. The most problematic nuclei are cobalt, manganese, gold and copper. Of course the activation is proportional to the irradiation time and the amount of the exposed isotope. In the case of an activation the NR station can not be entered and no more measurements can be performed until the activation has sunk under the allowed dose value.

stable isotope	isotopic abundance[%]	isotope after neutron capture	half-life
^{13}C	1.1	^{14}C	5730a
^{15}N	0.37	^{16}N	7.13s
^{18}O	0.2	^{19}O	27s
^{23}Na	100	^{24}Na	14.96h
^{26}Mg	11	^{27}Mg	9.46min
^{27}Al	100	^{28}Al	2.2min
^{30}Si	3.1	^{31}Si	2.62h
^{55}Mn	100	^{56}Mn	2.58h
^{58}Fe	0.3	^{59}Fe	45.1d
^{59}Co	100	^{60}Co	5.2a
^{63}Cu	63	^{64}Cu	12.7h
^{93}Nb	100	^{94}Nb	20000a
^{109}Ag	50	^{110}Ag	127d
^{197}Au	100	^{198}Au	2.6h

Table 2.3: Half life times of isotopes

Fortunately most isotopes like ^{14}C, ^{16}N, ^{19}O, ^{28}Al have short decay times and after a few minutes the tomography station can be entered again. Taking out the irradiated object requires the dose free measurement of the radiation protection staff. In the case of an activation, the object must remain in the tomography station until the radioactive nuclei have decayed and the objects fulfill the dose limit of 10 μSv/h. The mirror of the detector is permanently exposed to neutrons and showed after longer measurements a high activation level, which was identified to come from ^{24}Na nuclei with a half life of 14.96 hours and will soon be replaced by a Si wafer as a mirror. On the ANTARES sample manipulator objects with a weight up to 500 kg can be handled, the positioning works with a precision of a mm and the rotation is precise to 0.1°. For many investigations a complex and laborious sample environment is necessary because diverse states as chemical environments, temperatures or pressures must be compared in order to answer NDT questions. It should not be forgotten that during the time consuming preparation of a complex setup, precious beam time is lost. Last but not least, the security requirements must be fulfilled, that means a minimization of the amount of combustibles, explosives and materials, which get easily activated, in the tomography station. The irradiation time has to be minimized.

2.4 Image quality

It is difficult to define parameters for the image quality and there exist many different parameters, which confuse the physicist rather than to help him. This chapter, influenced by [Has91, 19], tries to give an orientation in this important field and to introduce the parameters, describing the measured data in the last chapter. The combination of four parameters is useful in considering the quality of an image: the spatial resolution Δx, the time resolution Δt, the relative noise σ and the contrast C.

- The spatial resolution Δx: There are many different definitions of the spatial resolution. Intuitively, the spatial resolution Δx of an imaging system can be defined in terms of the smallest distance that separates two objects and makes them still appear distinct. If this definition is not precise enough, the point spread function PSF or the modulation transfer function MFT are used. The PSF is the image of an ideal point object - the two dimensional resolution function of the imaging system. It is not a single black pixel but a spot due to the blurring of the imaging system, the amount of blurring and the shape of the spot is a measure of the spatial resolution. Normally the PSF can be described well with a 2D Gaussian curve and the full width at half maximum FWHM of the PSF is used as Δx_{PSF}. For a NR the response spot depends on the detector resolution or on the beam divergency. The spatial resolution is position and signal dependent Δx=Δx(x,y,μ), where μ is the mean grey level - the signal. Fortunately for linear shift invariant systems Δx is constant and the NR image can be described as a convolution of the object attenuation OBJ and the PSF (equation 2.3). The PSF is the convolution kernel in the equation below.

$$NR(x,y) = \int_0^y \int_0^x OBJ(\xi,\nu) PSF(x,y;\xi,\eta) d\xi d\eta \tag{2.3}$$

  In this case an experimental determination of the PSF characterizes the spatial resolution of the complete image. Since direct measurements of the PSF are difficult the edge spread function ESF, the response of a sharp knife edge absorber, can be measured easily. The ESF is the integral over the PSF. If the PSF can be fitted well by a Gaussian, the ESF is close to an error function (see Fig. 2.17).

  The distance from 10% to 90% of the ESF signal $\Delta x_{10/90}$ is also accepted as a measure for Δx. In literature mostly Δx_{PSF} or $\Delta x_{10\%MTF}$ is dealt as the spatial resolution. The relations between the three definitions are:

$$\Delta x_{PSF} = 0.918 \cdot \Delta x_{10/90} \qquad \Delta x_{10\%MTF} = 0.358 \cdot \Delta x_{10/90} = 2 \cdot x \quad \text{for PSF}(x) = 0.9 \tag{2.4}$$

- The time resolution Δt is the exposure time of the image and respectively the time of neutron collection. Δt is controlled by the camera software. A long exposure time offers better image statistics but consumes more beam time. It should be chosen as short as possible on the condition that the image quality is good enough to recognize the requested details. The time resolution is be limited by the opening time of the optical shutter or the image intensifier for the short times. The upper limit for time resolution is the dynamic range of the camera. It must be read out before pixel overflow occurs. The dynamic range can be expanded by multiple readout and summation of images.

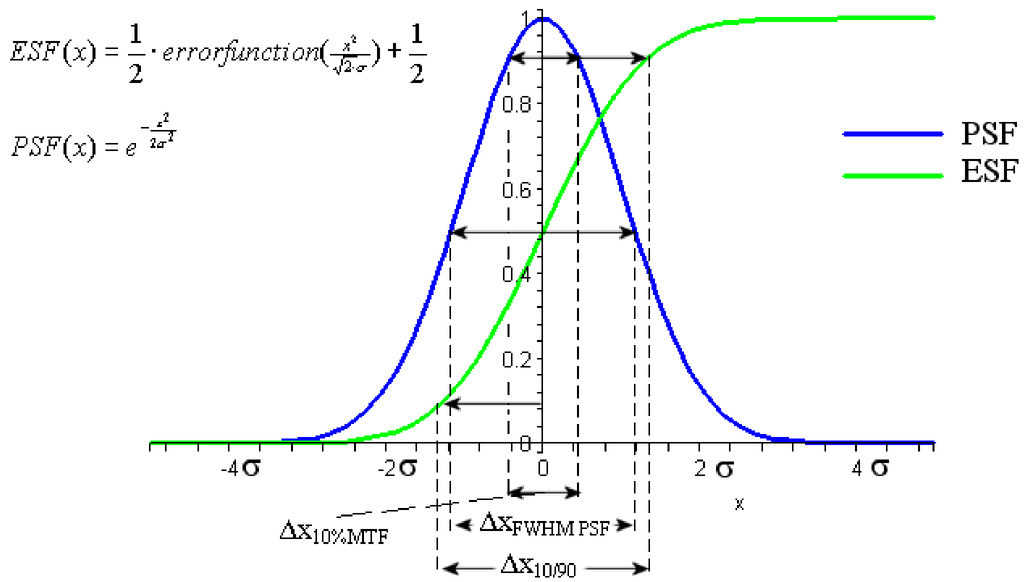

Figure 2.17: The mathematical functions used for the resolution determination

- The noise σ is the uncertainty or imprecision of the image. Normally the noise is position and signal dependent: σ=σ(x, y, μ). But in the case of a homogeneous detector and a homogeneous beam we can simplify the noise model and consider two forms of noise. The background noise σ_{bg}, limits the detection of small signals and the signal dependent noise σ limits the precision of signal measurement. The components of σ_{bg} are the readout noise and the thermal noise of the camera, the thermal photocathode noise of an intensifier, or neutron background. It can be determined by a dark current measurement. The origin of the signal noise σ are the photon and the neutron quantum noise, the amplifier noise in the CCD, the fluctuating beam intensity or scintillator degradation. The standard deviation from the mean σ_μ divided by the mean μ is the signal noise σ or relative noise. In chapter 4 the relative noise in the open beam area was calculated for most images. The inverse of σ is the signal to noise ratio SNR.

- The contrast C is an object property and can be estimated via thickness and the neutron attenuation coefficient of the object. In the NR image it finally is the signal difference between an object and its background (see Fig. 2.18).

Only the combination of all parameters gives a good description of the imaging system and determines the image quality. If a NR image is smoothed for instance, the relative noise σ can be reduced by sacrificing spatial resolution at the same time. What image quality is, depends on the inspected object and is defined by the inspector. In non destructive testing for instance the ability to recognize a detail is more crucial than a low noise. In addition to the discussed parameters, the size of an detail, the way of visualization and the experience of the inspector has an important influence (see chapter 3).

2.4.1 A practical examination of image quality

For both NR detectors at ANTARES the ESF of a strong knife edge absorber close to the detector was measured (see Fig. 2.19). As knife edge absorber a Cd plate of 2 mm

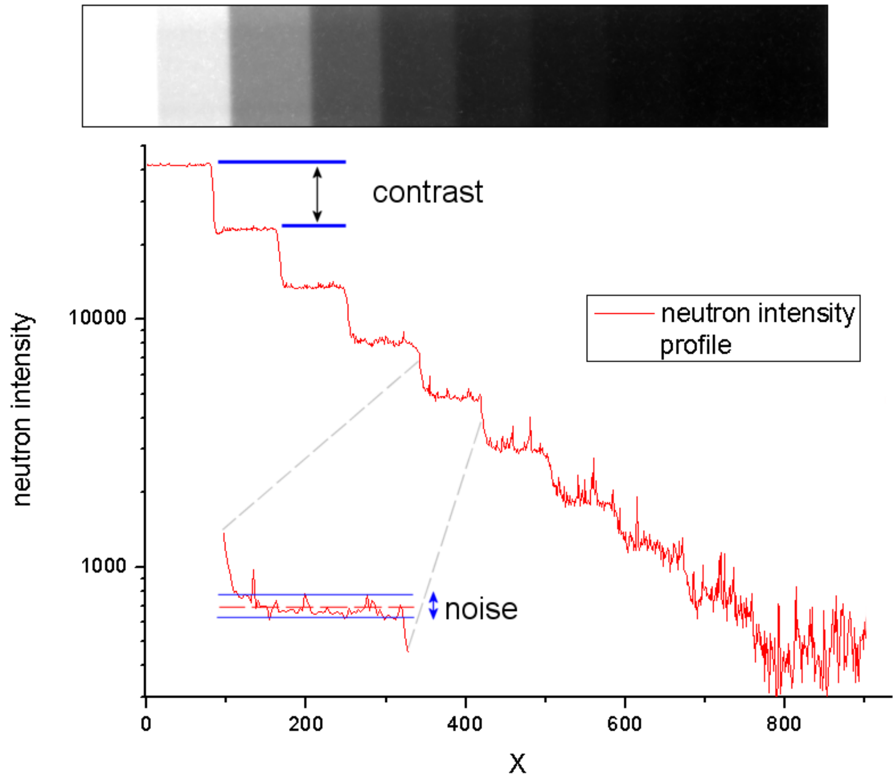

Figure 2.18: Contrast and noise in a neutron radiography profile of the step wedge above

thickness and a width of 1 cm was used. The known width allows the calculation of Δx not only in the number of pixels but also in mm with the IDL program `stufenfit.pro`.

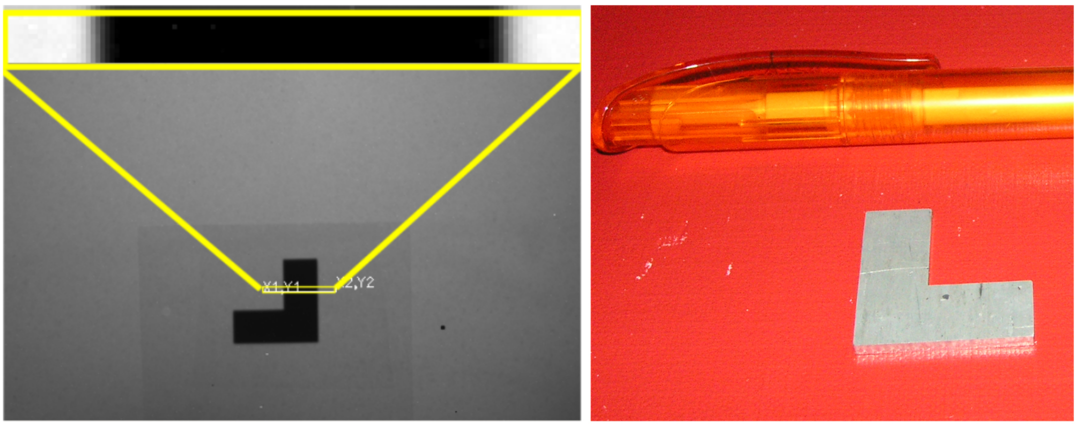

Figure 2.19: NR of the Cd absorber (left) for resolution determination, photograph of the Cd absorber (right)

The edge profile extracted from NR image was fitted with an error function. The steepness parameter of the error function Δx is the crucial resolution parameter.
Preconditions for this method are:
-A strong neutron absorber with a sharp knife edge parallel to the detector plane: A tilting of the Cd sample up to 5° in the beam direction does not spread the edge and affect Δx remarkably.
-A negligible fraction of scattered neutrons: Scattered neutron from the object or from

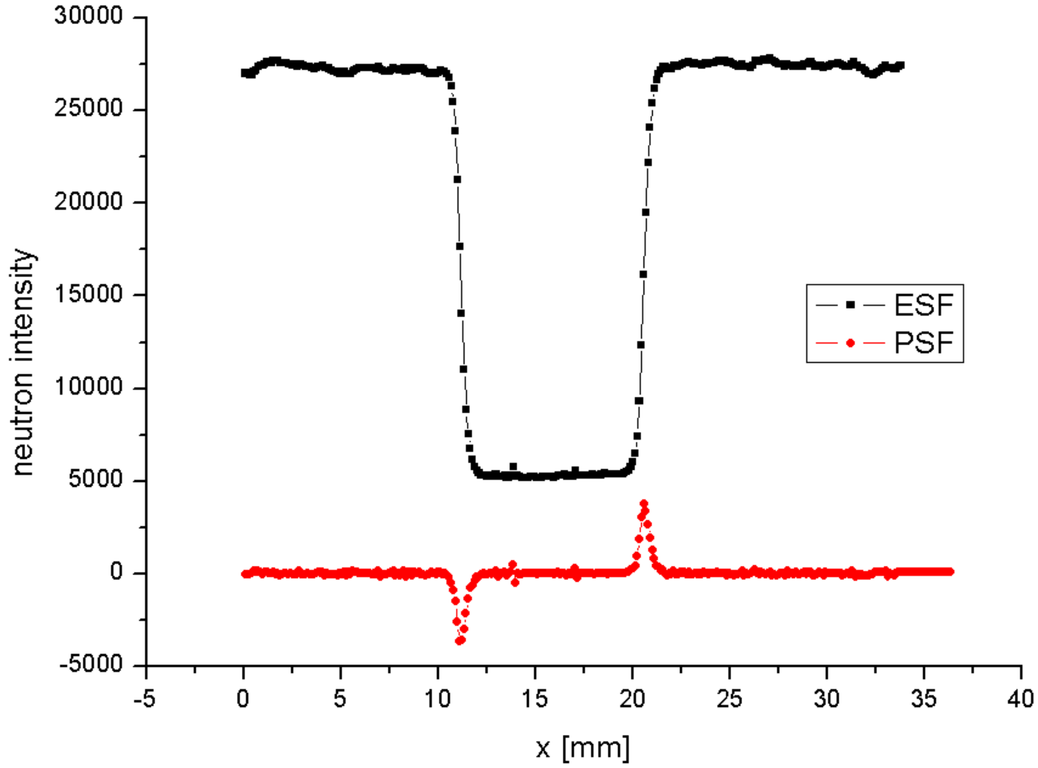

Figure 2.20: The grey level profile of the Cd edge above, also called edge spread function ESF

the shielding broadens the edge profile and deteriorates Δx.
-A short distance from the Cd knife edge to the detector plane: Otherwise the beam divergency increases Δx.
If these conditions are not fulfilled still a lower estimation of Δx is possible. The derivative of the ESF in Fig. 2.20 is the point spread function PSF.
The PSF in Fig. 2.21 was extracted from the derivative of the profile. In most cases the PSF will have a Gauss shape because of the several influences of the beam divergency, the scintillator spot size and the objective of the camera. In Fig. 2.21 the PSF was fitted with a Gauss curve with a FWHM of 0.6 mm. In the case the image blurring comes predominantly from the converter, the curve would be Lorentian [Bac02, 13]. The normalized fourier transform of the data in Fig. 2.21 is the so called modulation transfer function MTF (see Fig. 2.22).

The MTF is a more precise description of the spatial resolution than the distance of two resolvable structures. The MTF is the ratio between a spatial modulation amplitude in the object attenuation and the modulation amplitude in the image versus the spatial modulation frequency. At lowest frequencies the MTF is normalized to one, at highest frequencies it must turn to zero. The higher the spatial frequency at which the MTF drops and the steeper the drop, the better is the image quality. Sometimes special optical patterns or appropriate calibration objects are used for a direct measurement of the MTF. In the semilog plot in Fig. 2.23 the MTF was fitted with a Gaussian and with an exponential function. The Gauss curve fits the data slightly better.

The time resolution Δt for individual images is the exposure time of the CCD Δt_{exp} set by the user. The used scintillator puts a lower limit to Δt with its scintillation decay time. For real time imaging the frame rate becomes relevant. The frame rate f can be approximated for both cameras: $f=1/(\Delta t_{exp} + N_{pixel} \cdot \Delta t_{readout} + N_{columns} \cdot t_{vss})$. The

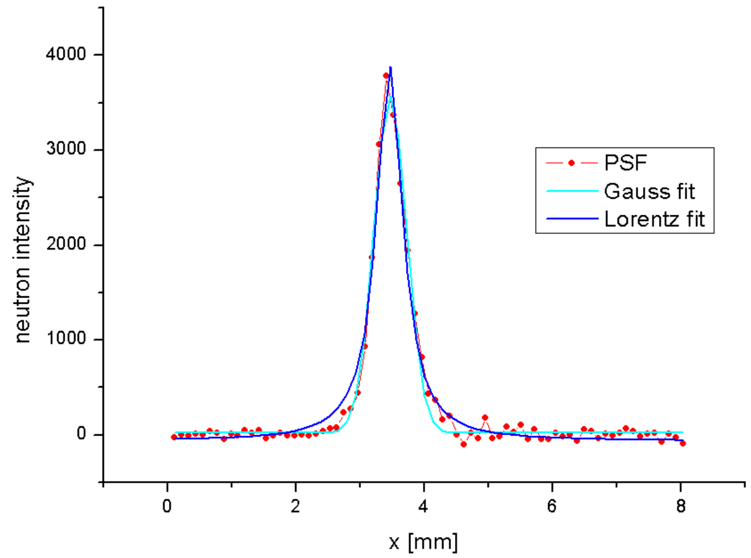

Figure 2.21: The Point Spread Function

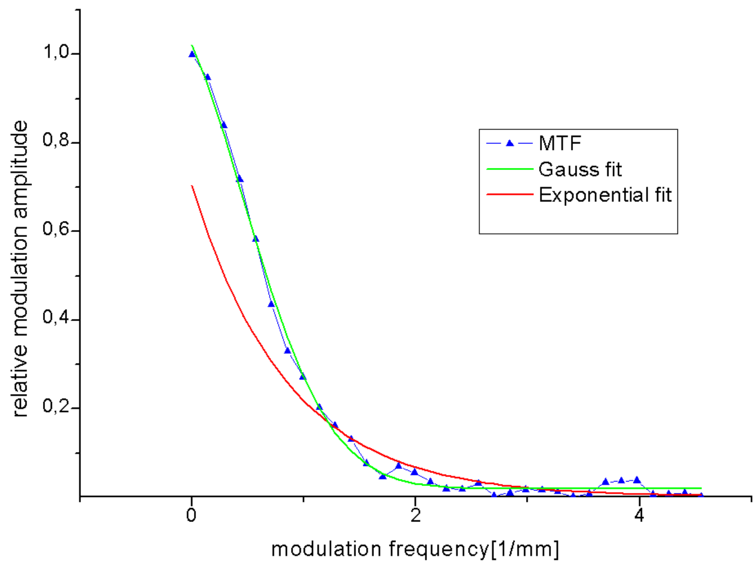

Figure 2.22: MTF of the imaging system with a Gauss and a Lorentian fit

readout time $t_{readout}$ can be set to 1, 2, 8 ore 16 μs/pixel, the time for a vertical shift t_{vss} is 16μs for the ICCD and 112 μs for the CCD.
The noise characteristics become crucial in the case of small contrasts. The background noise σ_{bg} is measured with a dark image. The signal noise σ(x,y, μ) is mainly photon and neutron shot noise, which can depend on position and the signal μ. In a first approximation it can be calculated from the mean and the standard deviation in an open beam area: $\sigma = \sigma_\mu/\mu$. Normalizing and correcting the image for known artefacts like described in the next chapter allows a more exact estimation of the relative noise σ. If the beam is not homogenous σ may differ in different positions also in normalized images and more NR images must be acquired in order to characterize σ(x,y, μ). The most important noise component for short exposure times is the neutron quantum noise, which is proportional to the square root of the neutron flux. That was confirmed impressively at the neutron spallation source at PSI after a beam breakdown. The intrinsic neutron quantum noise

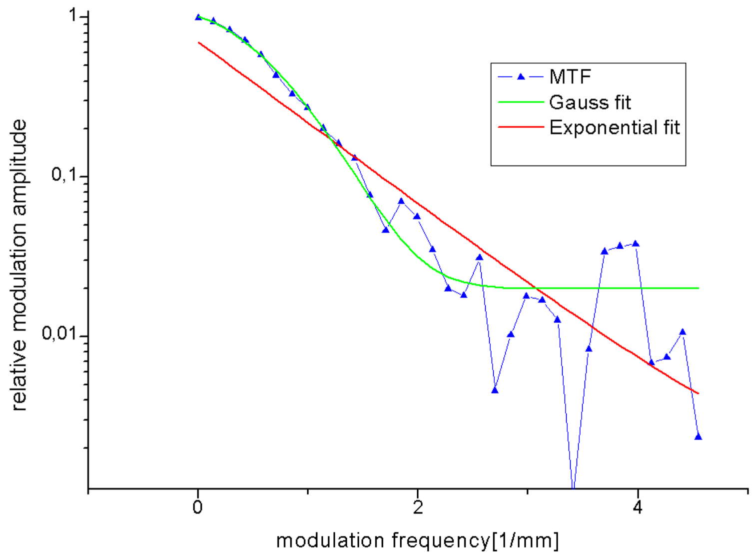

Figure 2.23: Semilog plot of the MTF with a Gauss and a Lorentian fit

behavior follows perfectly the square root dependence as visible in Fig. 2.24.
For both cameras at ANTARES the mean grey level μ and the noise σ were modelled in dependence of the camera parameters for a reactor power of 20 MW and L/D=400, see equations 2.5 and 2.6. Dark images of the cameras showed a grey level offset C of 1350±19 for the readout with 1 μs/pixel and 355±9 for the readout with 2 μs/pixel due to the DC offset in the ADC circuit. The variation of the offset is the dark current. The mean grey level depends on the objective but is independent from the distance d between camera and scintillator, since the light intensity decreases with $1/d^2$ but the area seen on the scintillator increases with d^2. The variable bin stands for the binning, bin = 2 means that 4 pixels are combined into one pixel. In the case of the ICCD camera the intensifier gain is an additional parameter which can be set from 0 to 255. N is the number of identical images acquired. The offset in the noise A and B varies between the measurements and must be determined experimentally.
For the ICCD at T=-20°C with a 50 mm objective with a 2 mm adapter ring:

$$\mu \approx C + 30 \cdot \Delta t[ms] \cdot e^{-\frac{gain}{56}} \cdot bin^2 \qquad\qquad \sigma \propto \frac{\sqrt{\mu}}{\sqrt{N}} + A \tag{2.5}$$

For the CCD at T=-50°C and a 50 mm objective:

$$\mu \approx C + 33000 \cdot \Delta t[ms] \cdot bin^2 \qquad\qquad \sigma \propto \frac{\sqrt{\mu}}{\sqrt{N}} + B \tag{2.6}$$

If some details about the object of investigation like the geometry, the material composition as well as geometry and material composition of the details are known, the prospective attenuation and contrasts can be estimated. Finally the camera parameters can be calculated such that the noise is low enough to see the necessary contrasts.

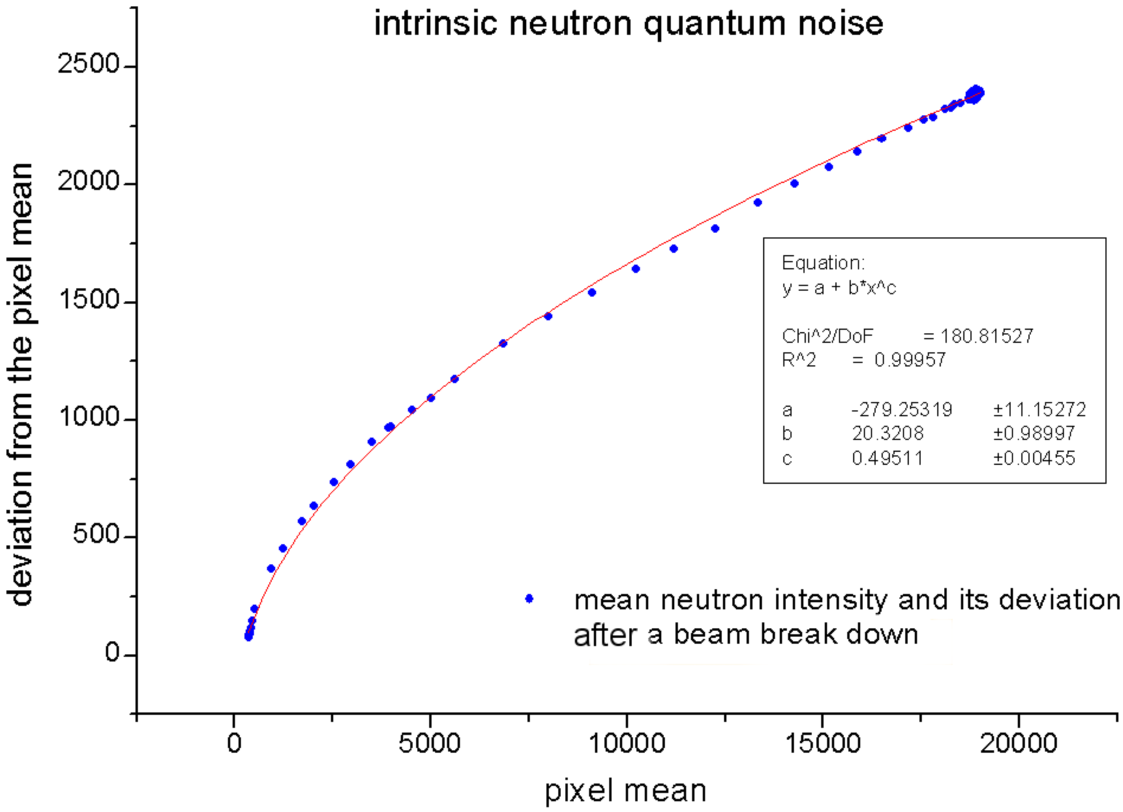

Figure 2.24: Noise σ versus the neutron flux (pixel mean), measured at PSI after a beam break down

Chapter 3

Data evaluation and visualization

The aim of the evaluation is the extraction of the relevant measured physical quantity of measure and its uncertainty. For NR this is the neutron attenuation $I/I_0(x,y)$ for each and every pixel. The evaluation consists of five steps:

1. Correction for known artefacts: The following NR artefacts as gamma spots, beam fluctuations, scintillator degradation, lens distortions and image deconvolution are treated in this chapter.

2. Normalization: All position dependent offsets and sensitivities of the NR detector can be corrected by this calibration method.

3. Calculation of the uncertainty: In order to predict future NR results and to start with quantitative analysis this part is absolutely necessary.

4. Quantitative analysis: Quantities like volume, area and attenuation properties can be extracted.

5. Visualization: Sometimes quantitative results are not necessary and the right visualization answers the question.

3.1 Hard and software for data analysis at ANTARES

At the ANTARES instrument a typical 16 bit NR image of 2048 x 2048 pixel has size of 8 MB. For a NT typically 400 NRs, or 3.2 GB of data are recorded within 3 hours. Similar data amounts are produced at NR series of objects like for instance dynamic NR measurements. A maximal data rate of 1 GB per hour is expected. Of course, the preparation time exceeds the measuring time by far, but still all the produced data must be evaluated. That sets considerable requirements to hardware and software.
Our hardware consists of a PC cluster in a 100 Mbit network, which will soon be upgraded to a 1 Gbit network in order to reduce transfer times. The data is acquired with an Intel Pentium 4 PC with 3 GHz and 1 GB RAM, which controls the camera. The data is stored on a file server with a daily backup system, which also serves as a platform for data exchange between the users. The data evaluation and the tomographic reconstruction is done by the members of our group on standard PCs. Finally, for the calculation and memory intensive visualization a 64 bit AMD Dual Opteron Linux machine with 2.4 GHz and 16 GB RAM is at our disposal.
Different software tools for data acquisition, data processing, and data visualization are used. The Andor MCD and IStar software write the raw data from the detector to the

hard disk. All the NR data is stored in 16 bit tif format in a special directory structure in order to prevent data losses. This structure includes directories for open beam images, dark images, the raw data, a detailed protocol file of the measurements and if available a digicam picture of the object. Only with careful and diligent structuring of the data, the data evaluation can be automated. In near future a professional data base will be used. The data is evaluated with special programs developed in IDL. IDL is a powerful software with a rich library of proven math, statistics, image processing and signal processing routines for data analysis, including many of the best algorithms from Numerical Recipes and the LAPACK numerical library. A core strength of IDL is image processing. Mathematical and logical operations can be applied to more dimensional arrays with simple commands and are processed very fast. Available directory and file access routines allow all kind of processing of complex data structures. For the memory intensive visualization of 3D NT data sets the software VGStudio of the company VolumeGraphics is the tool of choice. A big improvement was the use of the virtual network client (VNC) software, which made it possible to have remote access to other Windows machines. For the common development of IDL programs a version control software like CVS is strongly recommended.

3.2 Artefact correction

3.2.1 Beam fluctuations

Especially at spallation neutron sources the beam intensity may strongly fluctuate with time. The consequence is an unknown integral flux and a resulting difficulty to compare the images of varying brightness (shown in Fig. 2.5 for the ANTARES beam). For a first check the average grey level of a region in a series of images and its standard deviation can be plotted in a diagram (program `batchinfo.pro` does that job) like in 3.10. The program `batchinfo.pro` checks a chosen area in every image for its mean and its standard deviation. If the effect plays an important role it can be corrected by a multiplication with a constant factor in order to get a equal intensity level in every image (`roi_normalize.pro`).

3.2.2 Gamma spots

A difficult problem to overcome are the white spots in the image, coming from gammas hitting the CCD. Filters have to be used to get rid of these artefacts. For the identification of a gamma spot in the image two strategies are thinkable: To compare the grey level with the surrounding pixels or to acquire more identical images and to compare the same pixels of every image in the series. Both was implemented in IDL:

```
u_filtered=serienfilter(dirname , displayratio=disp_ratio,
displaybright=disp_bright, n_sig_ufilt=0.1, bw_ufilt)
```

The surrounding filter, u_filter, checks the neighboring pixels of a box with a boxwidth bw_ufilt and calculates the mean value of that box. If the grey level of the pixel is more than n_sig_ufilt times higher then it is replaced by the mean value. This filter is very effective and mostly used, but bw_ufilt and n_sig_ufilt must be carefully chosen. Good values are bw_ufilt=6 and n_sig_ufilt=2.5 - 3.5. If the values are too low object information especially at the edges gets lost. If on the other hand the values are too high the gamma spots are not filtered.

```
s_filtered=serienfilter(dirname , displayratio=disp_ratio,
displaybright=disp_bright, n_sig _sfilt=0.1, bw_sfilt)
```

The series filter, s_filter, checks the same pixels of a number bw_sfilt of images of a series and calculates the median (the middle) value of these grey levels. If the grey level of the pixel is more than n_sig_sfilt times higher then it is replaced by the mean value of the series. This filter works well only with more than three images.
The best results have been obtained with a combination of both filters, starting with the series filter (see Fig. 3.1). In order to see the success of a filter a special method for the visualization was applied: false color images of the difference between filtered and unfiltered image.

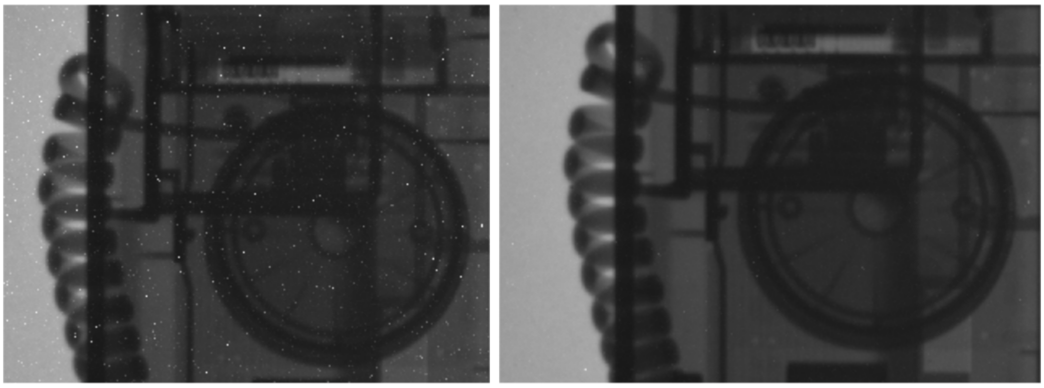

Figure 3.1: Cutout of a NR of a telephone with many white spots (left), after the filtering (right)

In Fig. 3.2 a difference image showing only the filtered gammas and its grey level histogram is displayed. In the histogram the grey level distribution of the gamma events becomes visible. Almost all gamma events increased the grey level only slightly by about 100. In principle the histogram contains some information about the gamma energies. It could be possible to predict some materials inside the object by studying the gamma spectrum.

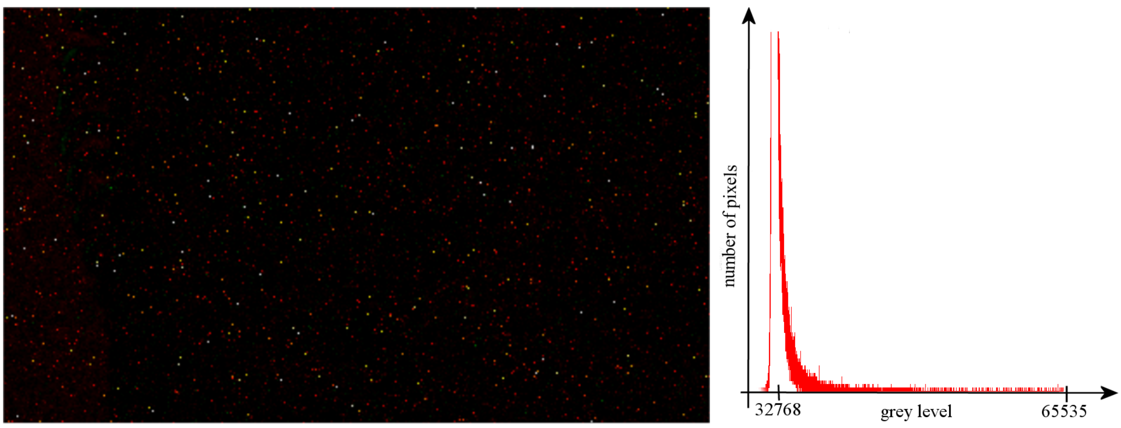

Figure 3.2: Difference image showing the isolated white spots (left), grey level histogram (right)

3.2.3 Scintillator degradation

The effect of scintillator degradation was observed for accumulation times of a few hours at high neutron fluxes [Hil05, 6]. For NT measurements or long NR series they can be identified quite easily. Taking and comparing open beam images before and after the long measurements show, that areas covered by a strongly attenuating object before are brighter due to less scintillator degradation. Partially these effects can be corrected by a linear interpolation of the open beam images before and after the measurement. Best results were obtained by taking alternately open beam images and images of the object.

3.2.4 Lens distortions

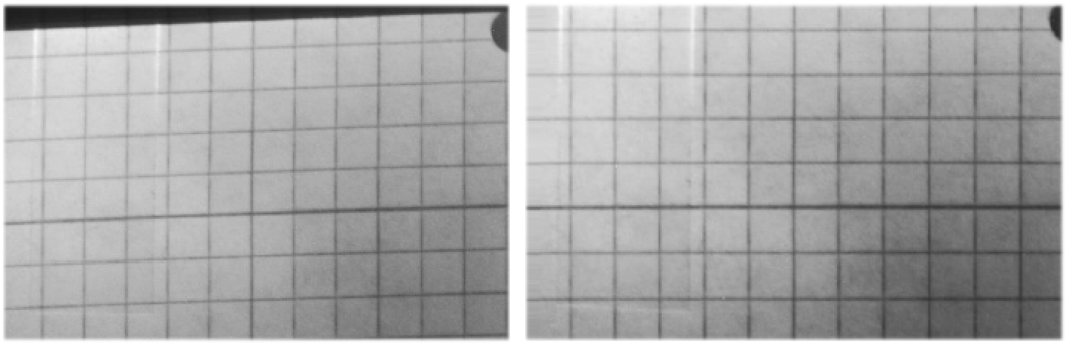

Figure 3.3: a) Image with lens distortions b) the same image after the correction [Sch04, 24]

In the corners of the NR image distances become smaller than they are in image center (2.2.2) due to optical distortions. Such distortions can disturb quantitative analysis. They can be identified best by substituting the scintillator with an optical test pattern. The deviations can be corrected with an interpolation algorithm like `lens_distortion.pro`.

3.2.5 NR deconvolution

NR image unsharpness can have several reasons: the optical misalignment, the beam divergency in combination with a large object to detector distance or the intrinsic scintillator unsharpness. If the PSF is position independent, the NR image is a convolution of the attenuation function OBJ and the PSF according to equation 2.3. The convolution in chapter 2 corresponds in Fourier space to a multiplication:

$$\mathcal{FFT}(NR) = \mathcal{FFT}(OBJ) \cdot \mathcal{FFT}(PSF) \tag{3.1}$$

The complex fourier coefficients of the PSF are multiplied with the spectrum of the OBJ. Knowing the PSF it is possible to calculate point wise the object attenuation OBJ by inverting the convolution - by devonvolving OBJ:

$$OBJ = \mathcal{FFT}^{-1}\left(\frac{\mathcal{FFT}(NR)}{\mathcal{FFT}(PSF)}\right) \tag{3.2}$$

Unfortunately this approach leads to two problems:

1. The PSF may be singular and can be not be deconvolved because the fourier coefficients are zero.

2. The NR image contains noise, which adds to the signal at high frequencies, which is already damped due to the convolution process. With the noise amplification during the inversion process the image content is destroyed.

The Wiener filter $\mathcal{WF}$ is a more advanced approach and takes the noise R into account, image B = OBJ + R and minimizes the variance.

$$OBJ = \mathcal{FFT}^{-1}\left(\mathcal{FFT}(NR) \cdot \mathcal{WF}\right) \qquad \mathcal{WF} = \frac{\mathcal{FFT}(PSF)}{|\mathcal{FFT}(PSF)|^2 + \frac{|\mathcal{FFT}(R)|^2}{|\mathcal{FFT}(NR)|^2}} \tag{3.3}$$

A difficulty is the estimation of the power spectrum of the relative noise $|\mathcal{FFT}(\mathrm{R})|^2/|\mathcal{FFT}(\mathrm{NR})|^2$. It can be determined experimentally. If it is zero, the Wiener Filter turns into the inverse Filter (equation 3.2). The result of the application of the Wiener filter to a NR image is visible in Fig. 3.4. In the deconvolved NR image more details like the thread of the screw or the oil rest in the tap hole can be identified, even if the noise increases.

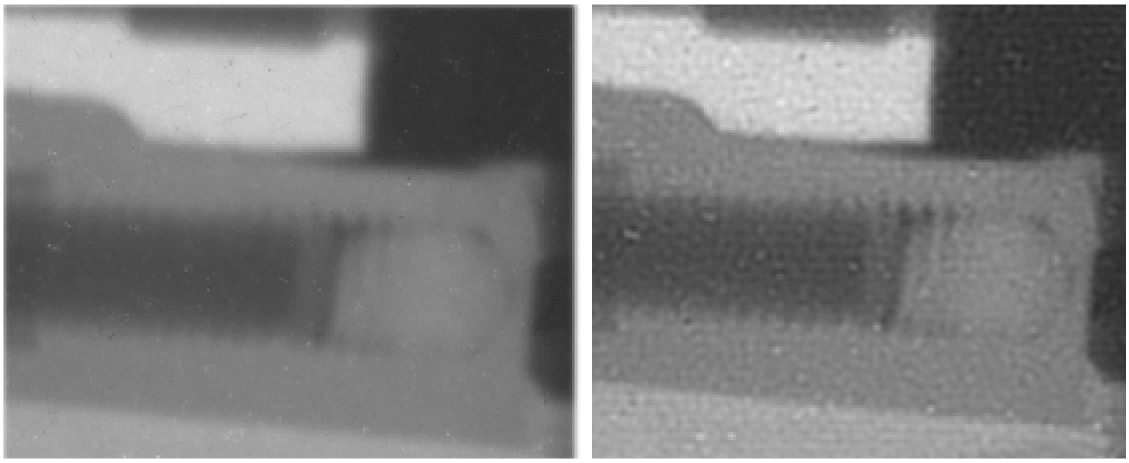

Figure 3.4: NR cutout of a screw (left) the same NR cutout after a deconvolution with the Wiener filter (right)

For better deconvolution more detailed noise models have to be developed. There are statistical and recursive deconvolution algorithms like the maximum likelihood or the maximum entropy algorithm. For more details see [Jai89, 21] and [Pra91, 22].

3.3 Normalization

Since the neutron beam, the scintillator, the optics and the CCD are not perfectly homogeneous, artefacts appear in every NR image. They are misleading in the interpretation of the data. Whenever possible the data is calibrated with open beam images OB (or white images) and dark current images DI (or black images). OB are NR images with exactly the same parameters of the beam without the object and DI are images with exactly the same parameters without neutron irradiation. The normalized image NI is:

$$NI = \frac{NR - DI}{OB - DI} \tag{3.4}$$

In this way relative measurements are performed and the corresponding procedure is called normalization (see 3.5, 3.6).

Even if a normalized NR image seems very flat, because all the inhomogenities of the beam, scintillator and optics and CCD disappear, the noise in that image (or the uncertainty image) still shows such effects. That is visible in the corners of the Fig. 3.6, right. The uncertainty of a normalized image σ_{NI} can be calculated by the propagation of uncertainties:

$$\sigma_{NI} = \sqrt{\left(\frac{1}{OB - DI}\right)^2 \sigma_{NR}^2 + \left(\frac{NR - DI}{(OB - DI)^2}\right)^2 \sigma_{OB}^2 + \left(\frac{-1}{OB - DI} + \frac{NR - DI}{(OB - DI)}\right)^2 \sigma_{DI}^2} \tag{3.5}$$

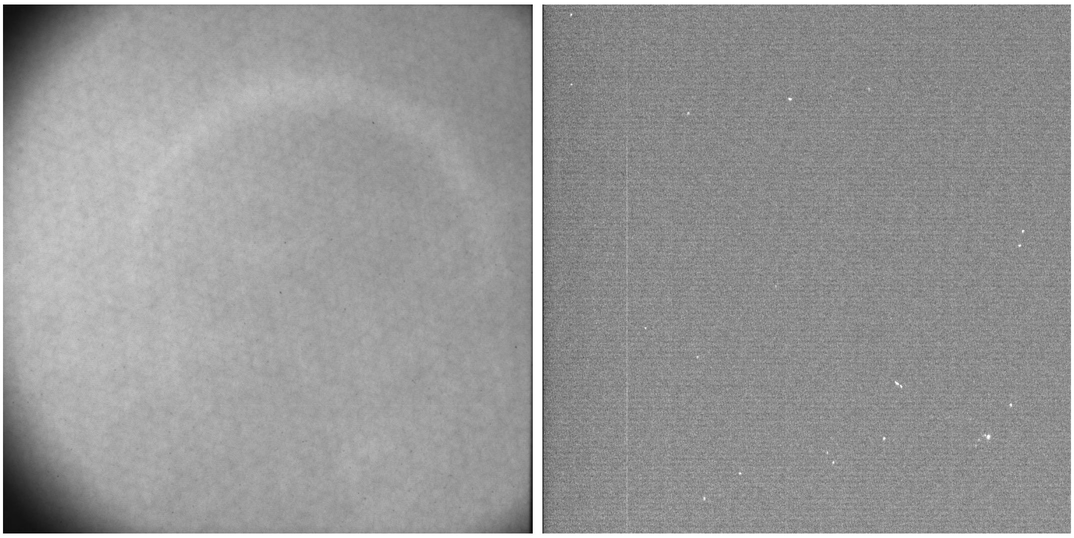

Figure 3.5: Open beam NR (left), dark image (right)

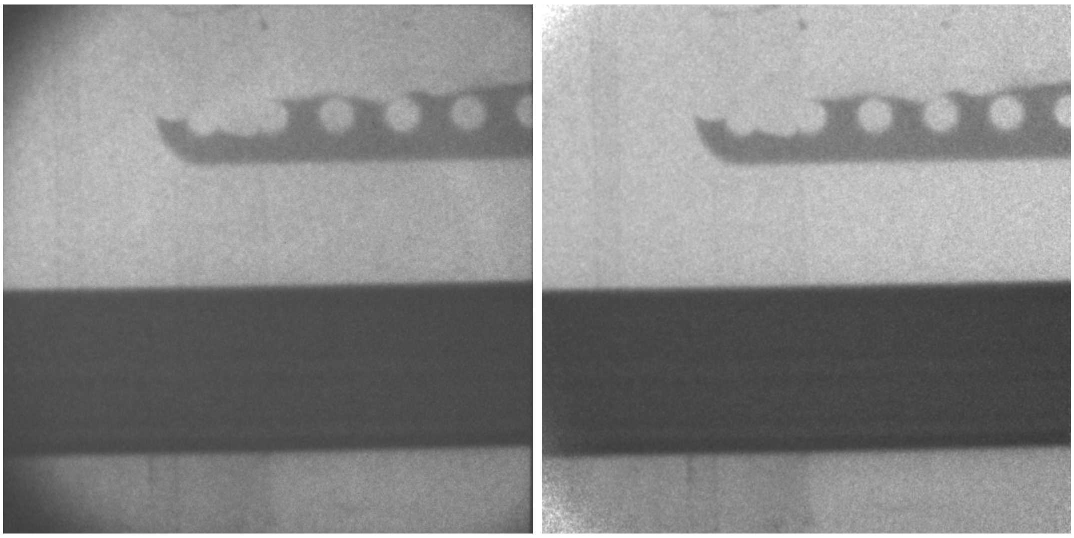

Figure 3.6: Raw NR of a refrigerator (left), the same NR after normalization (right)

3.4 Reproducibility and uncertainty of a NR image

The definite quality proof of an experimental method is its reproducibility. Therefore not only a NR image but also an image of its uncertainty is necessary. In the field of NR not many works about analysis of uncertainties were found and an own evaluation procedure was developed in order to guarantee the reproducibility. The calculation of the uncertainty allows the careful search for systematic errors and the further improvement of the setup. The IDL program `mess_unsich.pro` calculates the mean μ_{NR} according to equation 3.6 and the uncertainty σ_{NR} of μ_{NR} for one NR and the uncertainty $\overline{\sigma_{NR}}$ of μ_{NR} for a series from n NR images acquired under identical measuring conditions and with identical acquisition parameters (equation 3.7):

$$\mu_{NR} = \sum_n \frac{NR_n}{n} \tag{3.6}$$

$$\sigma_{NR} = \sqrt{\frac{1}{n-1}\sum_n (NR_n - \mu_{NR})^2} \qquad \overline{\sigma_{NR}} = \frac{\sigma_{NR}}{\sqrt{n}} \tag{3.7}$$

Fig. 3.7 shows the result of the uncertainty calculation for a NR series of step wedges. The relative uncertainty image (Fig. 3.7c) $\sigma = \overline{\sigma_{NR}}/\mu_{NR}$

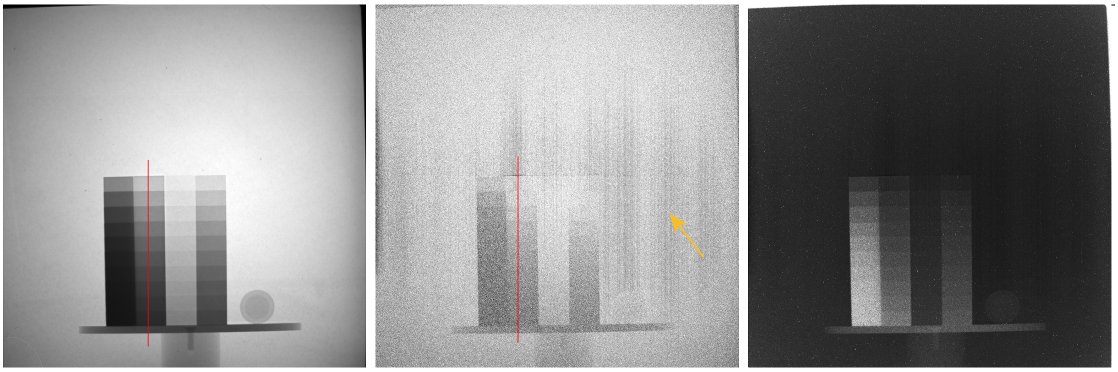

Figure 3.7: NR of step wedges: a) mean of 100 NR, b)uncertainty, c) relative uncertainty

The yellow arrow in Fig. 3.7 b) shows a camera noise, which was accidentally revealed checking the uncertainty image. The vertical line structure differs from the typical neutron quantum noise and must come from the readout and the amplification of the camera.
Extracting a line profile (column 788 from Fig. 3.7) the one dimensional data can be displayed together with its uncertainty bars (Fig. 3.8) and every pixel from the profile can be extracted again, like pixel (788 , 405) with a grey level of 18746 ± 3448. In that case the large uncertainty must come from a gamma event. Knowing the uncertainties of the NR data it can be compared and fitted much better to known geometries or theoretical models.

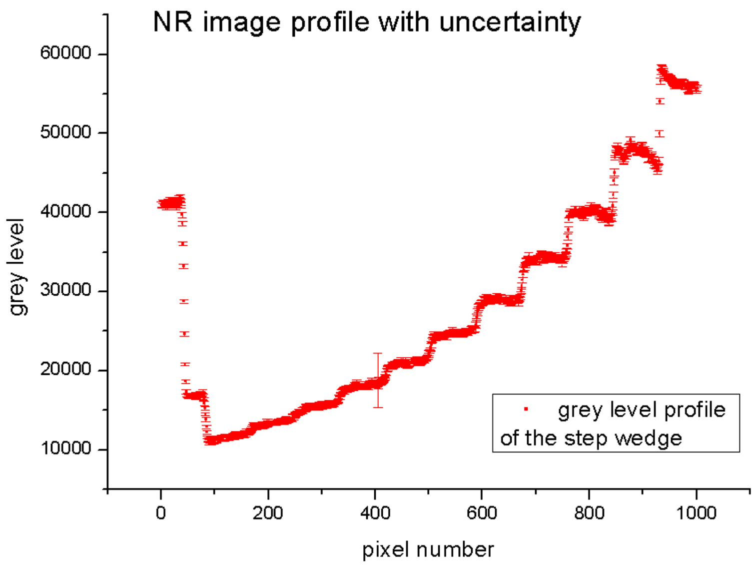

Figure 3.8: NR profile of the step wedges in Fig. 3.7

The inverse of the relative uncertainty σ is a parameter widely used in electronics: the signal to noise ratio SNR. According to equation 3.7 the SNR must increase with the square root of the number of images n. That was confirmed in a experiment, where 100 identical frames where acquired. Indeed, SNR increases with an increasing number of frames (see Fig. 3.9). In the case of Fig. 3.9 the SNR improved up to the excellent value of 2500.

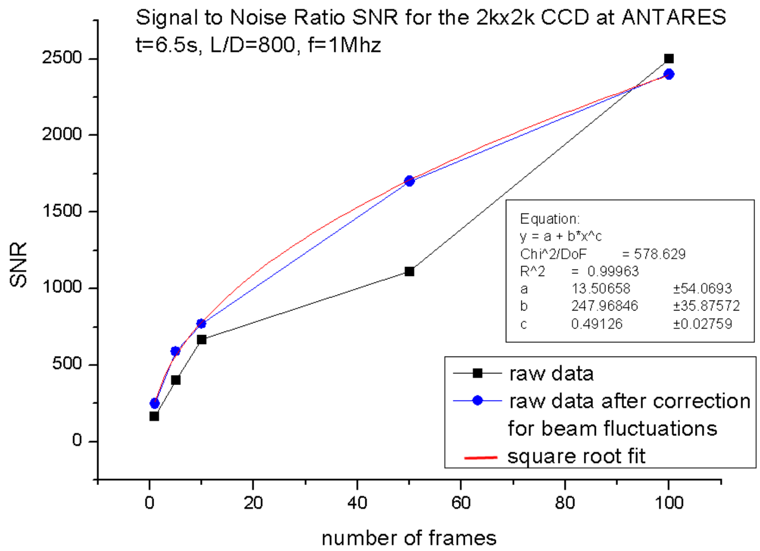

Figure 3.9: The SNR versus the number of frames

However, it is not always possible to image an object several times in order to calculate the uncertainty. In that case the uncertainty can be estimated, if the the response function of the detector is known. This was done for typical measurements with the NR detectors at ANTARES. Fig. 3.10 shows the relation between the mean value μ of many pixels and their uncertainty for different neutron attenuations and different grey levels respectively. An ideal sample for the determination of the detector response is a wedge with complete absorption on one side. In Fig. 3.10 an iron step wedge was inspected in a series of 100 NR images and the uncertainty was plotted versus the pixel mean for many pixels. Again, a square root law that confirms the quantum character of the noise can be recognized. Now the uncertainty of a single NR image, acquired with the same measurement conditions, can be predicted. Knowing the detector response and the number of images n in the series the uncertainty of a NR for these parameters can be estimated with the formula: $\sqrt{\mu} + 120$. The smallest μ is 6500 due to the background. Depending on many camera parameters like accumulation time, number of images, readout frequency, intensifier gain the uncertainty can be estimated in advance. In this way the lowest visible contrast for a certain object can be estimated.

3.5 Quantitative NR

Knowing the inspected material and its attenuation coefficient, geometry information from the NR image can be extracted:

- Distances and areas projected on the converter plate: Every pixel on the CCD corresponds to an area on the scintillator. Distances between two pixels in the image correspond to two points in the scintillator and because of a parallel beam geometry to a projected distance in the object. For such a distance measurement the exact positioning in the beam is crucial. The line or area to measure should be

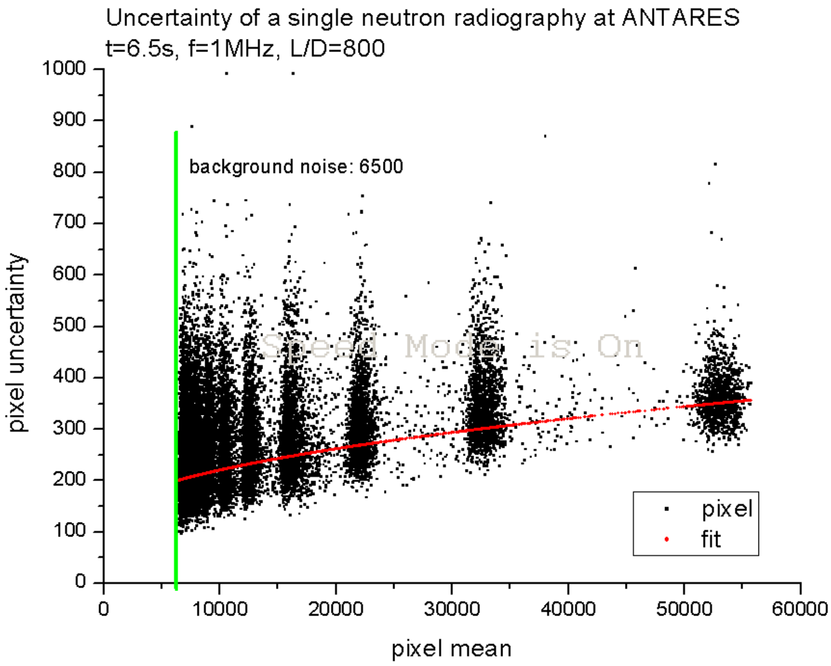

Figure 3.10: Detector response, the red line fits the most probable uncertainty, for a single NR it is approximately: $\sqrt{\mu} + 120$.

perpendicular to the beam. The calibration of the pixel size and spatial resolution is done with a strongly absorbing object with sharp edges of a defined size. Optical distortions of the objective may also influence the measurement and calibration measurements are strongly proposed.

- Total object thickness d along beam direction: If the material and its attenuation coefficient are known the thickness is:

$$\int_0^d \Sigma(z)dz = -ln(\frac{I}{I_0}) \qquad d = -\frac{1}{\Sigma}ln(\frac{I}{I_0}) \qquad \text{if } \Sigma \text{ is constant} \tag{3.8}$$

I is the decreased intensity after the object, I_0 is the intensity before the object. Both are proportional to the grey level in the image.

- For a homogeneous object the volume can be calculated by the multiplication of a pixel area A on the scintillator and the corresponding thickness.

$$V = \sum_{pixelsofareaA} -\frac{A}{\mu}ln(\frac{I}{I_0}) \qquad \text{if } \mu \text{ is constant} \tag{3.9}$$

V ... volume of the liquid $\left[cm^3\right]$
$I(z)$ ... neutron intensity after a distance x in material $\left[\frac{n}{cm^2\,s}\right]$
I_0 ... neutron intensity before the object $\left[\frac{n}{cm^2\,s}\right]$

Σ ... attenuation coefficient $\left[\frac{1}{cm}\right]$
A ... pixel area $\left[cm^2\right]$

Because of the energy dependence of Σ and the resulting beam hardening, Σ=Σ(d) can depend also on the thickness d of the sample. In the areas of strong attenuation the uncertainty increases exponentially. If the signal of the transmitted neutrons decreases to background level, the thickness could theoretically be infinite.

It is much more convenient to perform measurements on tomography data sets because the grey level in every voxel corresponds to the logarithm of the neutron attenuation coefficient and the distances are real distances. More complex measurements in a 3D volume are the identification of objects by grey level segmentation and volume measurements by voxel counting. The disadvantages of NT are artefacts from the reconstruction algorithms and the difficulty to calculate the uncertainty of the voxel grey levels.

3.6 NR data visualization

The aim of the visualization is to display the evaluated data in a form that relevant details of an object or artefacts of the imaging system become visible immediately. In medicine this must happen in a way that a diagnosis is possible afterwards, in NDT it must happen in a way that the NDT question is answered. The NDT questions can be very varying and much more quantitative.

3.6.1 Software tools for data evaluation and visualization

The data evaluation can often not be separated from the visualization. One part of the data evaluation can be handled automatically and the scientist only checks the results. The other part must be treated individually and therefore a appropriate, flexible software platform is absolutely necessary. Such a software was realized within the scope of this work. It was baptized "Neutroneye".

The software Neutroneye is a multi purpose software, which was developed under the IDL (Interactive Data Language) assembling code. Such a tool can only be developed with an object orientated language like IDL and requires some programming experience. A consistent structure and a consistent nomenclature are absolutely necessary. In 3.11 the graphical user interface of Neutoneye is visible. The image, a region of interest (ROI) and a grey level histogram of the image are displayed in the three windows. 16 bit and 32 bit tiff images can be loaded, processed and inspected. On a first glance the most important parameters of the image like name, size, minimal and maximal values can be found on the interface. By choosing a ROI and adjusting the two scroll bars for the lower and the upper grey level the hunt for details can start.

Important image parameters like the spatial resolution, the size of one pixel and the relative noise can be calculated with the ESF method and are displayed in the status bar in the lower region of the graphical user interface. The user has the choice between several visualization modes: classical black and white images, inverse images and false colour palettes. Every processed image or ROI can be saved as a bmp file for user reports. The grey level histogram has become a standard tool in image processing. It displays the number of pixels in the image as a function of their grey levels. It helps to adjust the sliders for the minimal and the maximal displayed grey levels and to find areas with slightly different grey levels like it is necessary for defects. Important parameters like the

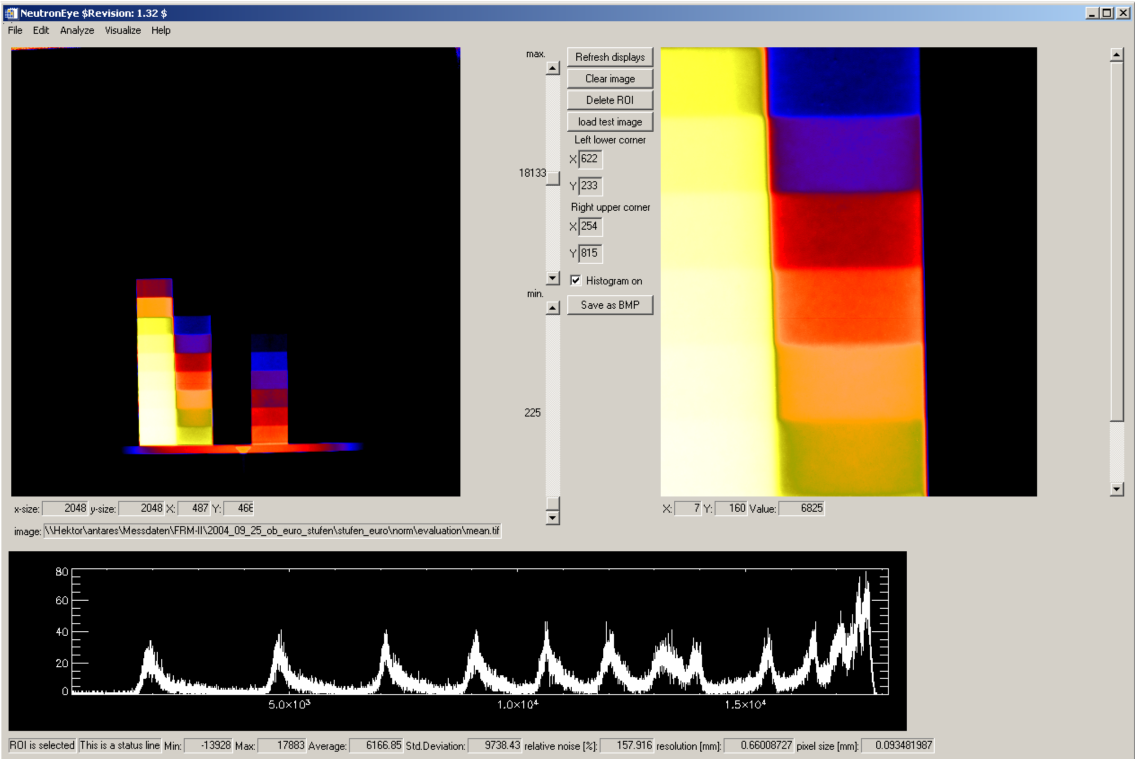

Figure 3.11: Graphical User Interface of NeutronEye showing a NR of step wedges in false colors

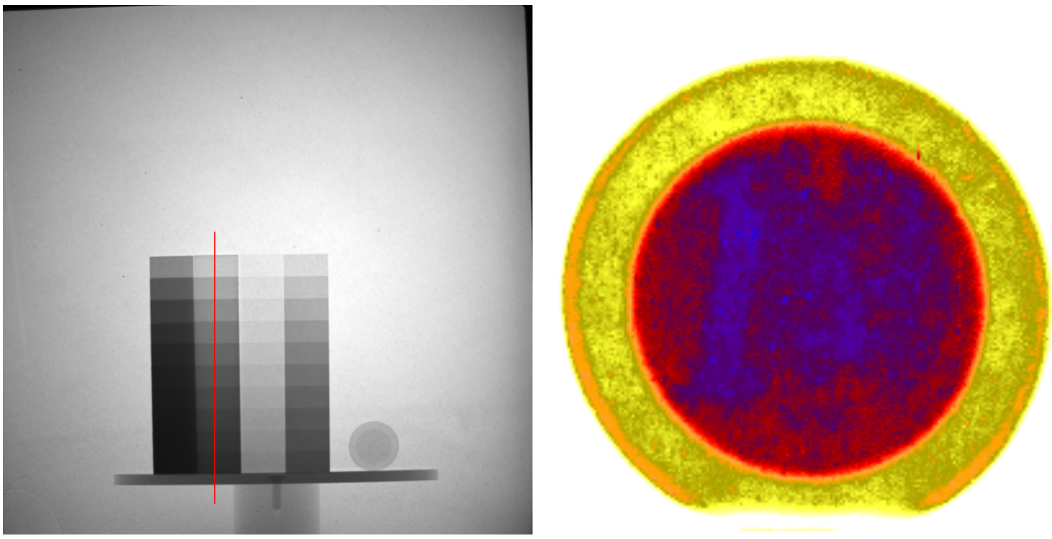

Figure 3.12: Extracting details of a NR image using Neutroneye

average grey level and its standard deviation of the ROI are calculated and displayed in the status bar. By moving the mouse over the ROI the grey level of each pixel is displayed below. In the menu almost all IDL programs described in this work can be found. Vertical and horizontal profiles can be taken and saved in a .dat file, images can be normalized and mean and uncertainty of a series of images can be calculated. By fitting the knife edge of a strong absorber the spatial resolution can be calculated with one mouse click.

3.6.2 Visualizing differences between images

One of the most common tasks in data evaluation is the comparison of two images. That can either be a comparison between two similar objects (like one with defects and another without) or a comparison between two images after different evaluation steps. While it is very difficult to find small differences by watching two images A and B one beside the other, with advanced inspection tools differences between images can be found immediately.
Consider two objects (with μ_1, x_1 and with μ_2, x_2), one behind the other like in Fig. 3.13.

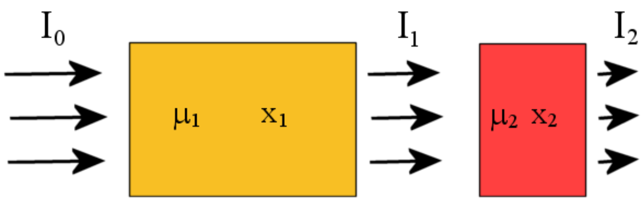

Figure 3.13: Two successive absorbers

The neutron intensities are according to the exponential attenuation law:

$$I_1 = I_0 e^{\Sigma_1 x_1} \qquad I_2 = I_1 e^{\Sigma_2 z_2} = I_0 e^{\Sigma_1 z_1} e^{\Sigma_2 z_2} \tag{3.10}$$

Three methods could be used to display the additional attenuation of the second object:

- Calculating of the ratio between images:

$$\frac{I_2}{I_1} = e^{\Sigma_2 z_2} \tag{3.11}$$

  This method (`normalise.pro`) makes sense if image B has additional attenuation in respect to image A. The ratio of B/A shows the additional attenuation of B. If A=B the ratio is 1 and grey level in the resulting image D is 65535. This method is used in the normalization operation. In the case of maximal attenuation in B the difference D=0. The uncertainty follows from equation 3.5.

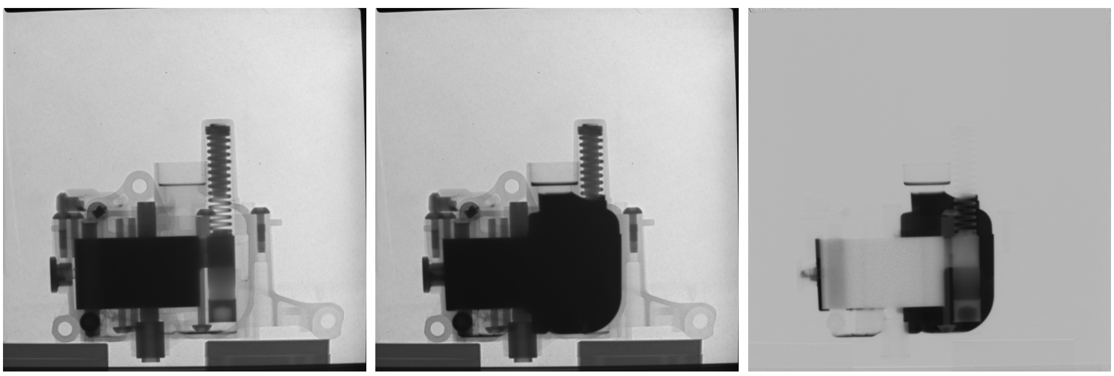

Figure 3.14: a) NR image of an empty oil pump, b) NR image of a filled oil pump, c) ratio of both showing the attenuation of the oil only)

- Calculating the difference between images:

$$I_2 - I_1 = I_0 e^{\Sigma_1 z_1} e^{\Sigma_2 z_2} - I_0 e^{\Sigma_1 z_1} = I_1 (e^{\Sigma_2 z_2} - 1) \approx I_1 \cdot \Sigma_2 z_2 \tag{3.12}$$

This method (`diff.pro`) makes sense for images with slightly different attenuation in the object, where it is not clear whether image A or image B shows a higher attenuation. For two 16 bit images A and B the program `diff.pro` calculates the difference image D=(A-B)/2+32768. All pixels in A and B with the same grey levels end up at the grey level 32768 in D, to the darker pixels in A a higher and to the brighter pixels in A are lower grey level in image D is assigned. With an optimized false color table the attenuation differences can be displayed in much more detail. But the interpretation is not trivial, because in the noise A and B are still visible. In Fig. 3.15 two NR of a tracked piston were subtracted. The oil movements are visualized.

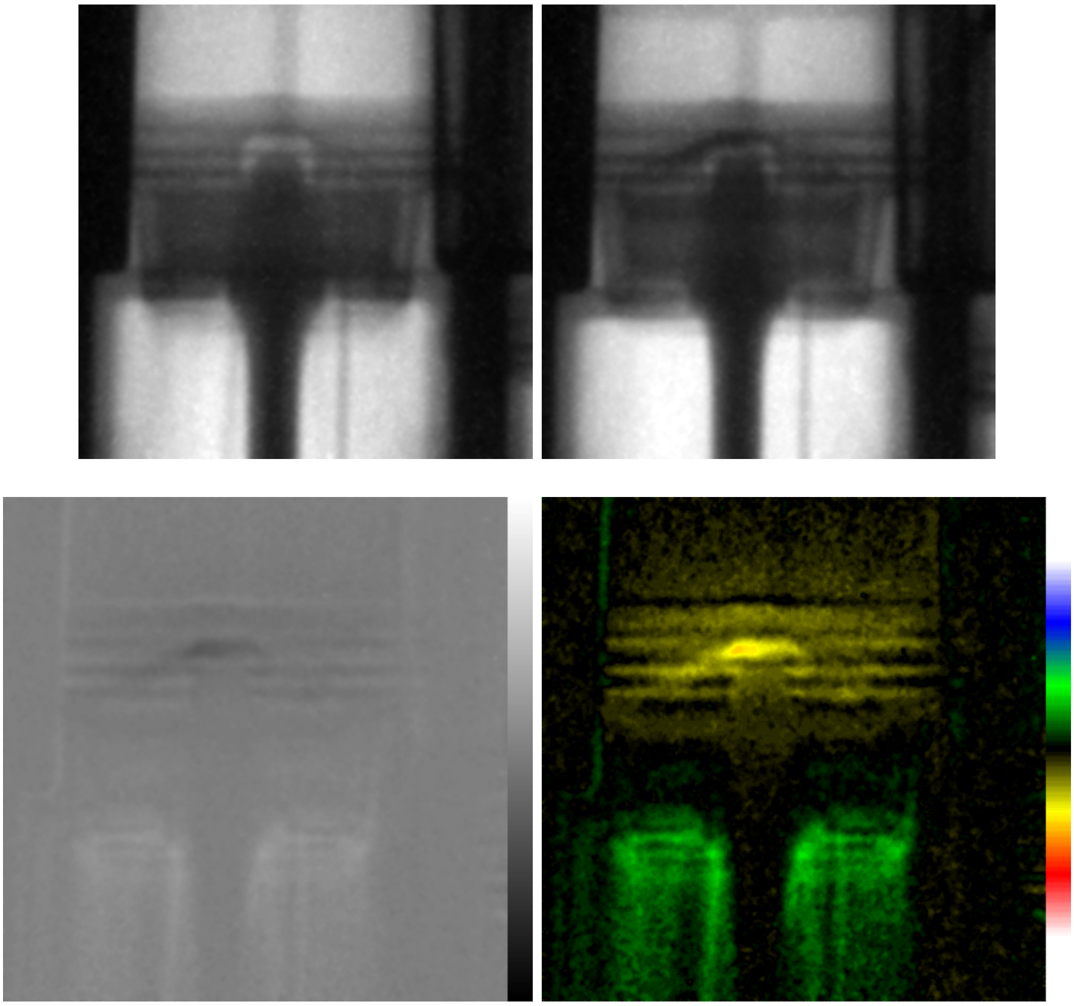

Figure 3.15: a) NR of the piston at t=0 ms, b) tracked NR of the piston at t=20 ms, c) difference image of both, d) difference image in false colors

- Composing a movie: Observing a series of consecutive images - a movie - our eyes immediately can detect a changing contrast (`batchview_tif.pro`). Fig. 3.25 shows that our eye is most sensitive to frequencies around 20 Hz. The composition of a film is suited best for a larger amount of similar images. Some examples are visible on CD.

3.6.3 Fusing images

Especially in NDT it is often necessary to combine different kinds of data. The combination of optical digicam pictures, NR images, X-ray images or difference images shows much more details than the individual images alone. The idea is to set one image semitransparent and to overlap or fuse it with another image (`img_align.pro`). If the images are coded with different colors the observer can read them more easily. A real challenge is the registration problem: the adaptation of resolution, position and tilting of the images, so that they fit to one another. The image Fig. 3.17 is a fusion of the images in Fig. 3.16 and makes the oil inside the combustion engine visible.

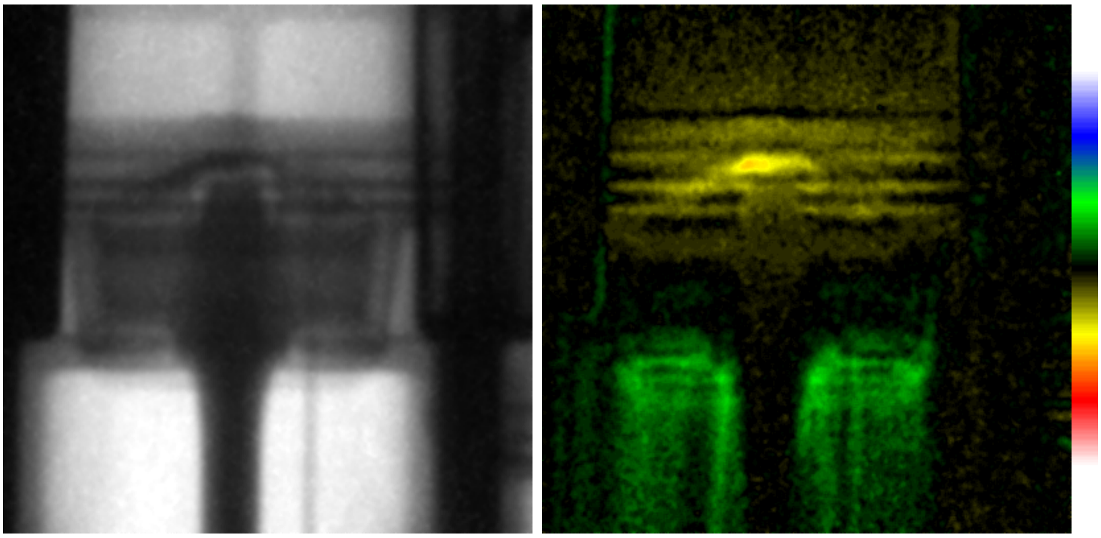

Figure 3.16: a) NR image of the piston, b) difference image of two NR images showing the oil in false colors

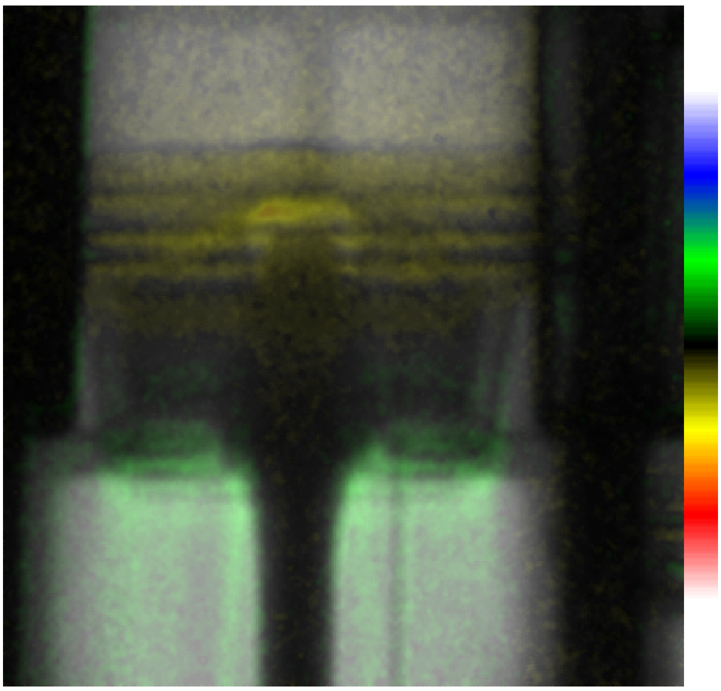

Figure 3.17: Fusion of both images

3.7 Limitations by the human eye

It may seem strange to mention the limitations of the human eye in this place. But it makes sense because in non destructive testing the most frequently asked question is: Can I see that detail or not? Not only the image quality (spatial resolution, time resolution, noise, contrast) but also the way it is visualized and the viewer must be considered in order to find a defect or an anomaly. Thus, it becomes very relevant to know the limits of the human vision for whom who studies the measured data in form of an image. In the following the human eye and it physical properties are described based on [Kol05, 20].
The sensitive detector area of the human eye is the retina (Fig. 3.18), made up of two types of photoreceptors: the rods and the cones. The rods have a high sensitivity under low ambient light and night vision, also called scotopic vision, while the cones have a higher spectral sensitivity.

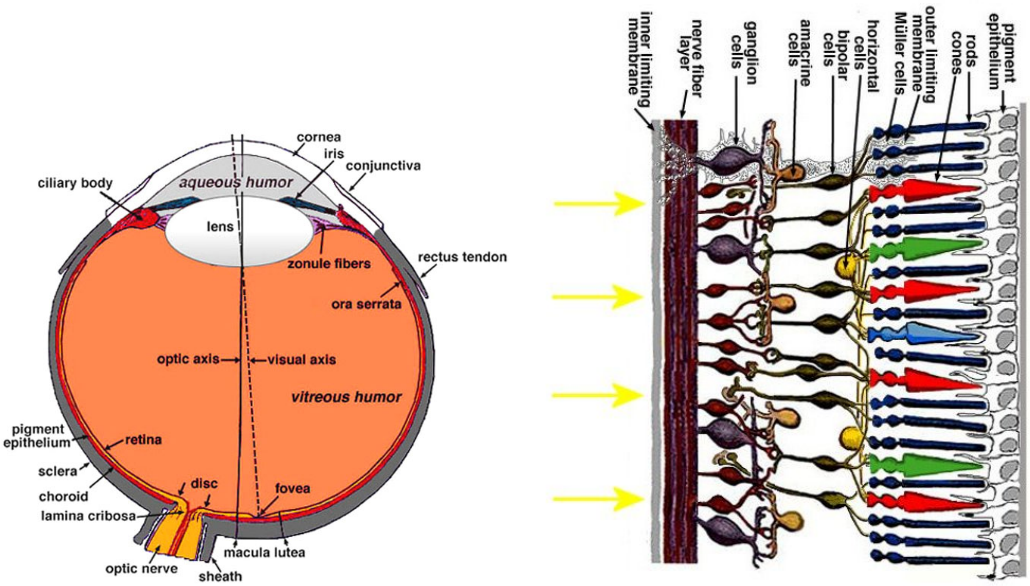

Figure 3.18: Human eye (left), retina (right)

The concentration of the two receptor types varies with eccentricity (angle from the fovea) and shows a remarkably high concentration of cones in the Fovea, the center of the retina. So even though the total field of view for a human eye is about 150°, the normal field of view is 30° and field of view with the best spatial resolution is about 1° (Fig. 3.19.

For the quantification of the visual acuity the Contrast Transfer Function CTF was measured with a sine wave pattern like the one below. The CTF is the resolution function of the human eye analogue to the MTF for an imaging system. Fig. 3.20 shows the measured CTF of the human eye in dependence of the spatial frequency for several luminances (unit: trolands). At the highest luminance a human eye is able to resolve frequencies of 10 cycles/degree at best. If the contrast becomes too small the sine grating can not be resolved any more. Depending on the distance between image and viewer the spatial frequency, which is resolved best, changes. At low light levels the maximum shifts towards lower spatial frequencies.

An additional property of the human eye must be mentioned: The human eye is able to sum over a certain area. This kind of preprocessing happens in the network of the rods on the retina and varies with eccentricity. The stimulus of a detail is proportional to the product of luminance and the stimulated area on the retina. Looking for a defect, the size

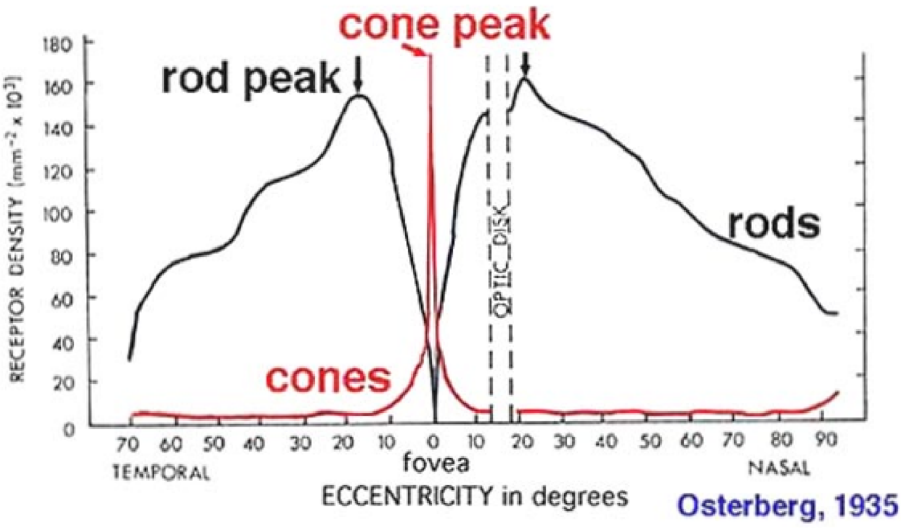

Figure 3.19: Rod and cone densities along the horizontal meridian

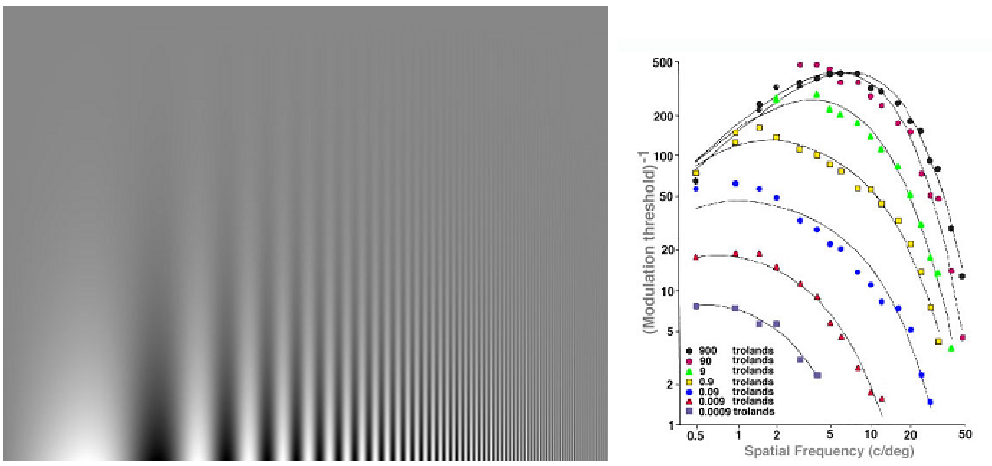

Figure 3.20: Image for the test of CTF (left), CTF of the human eye different luminances (right) [Kol05, 20].

of the defect matters as well as the contrast. Fig. 3.21 shows a test pattern with circles of varying contrast and size. If the product of contrast and area is large enough we are able to recognize it.

For the image inspection that means that the details we are able to recognize are limited by the MFT of our imaging system on the one hand, and on the other hand by the CTF of the human eye of the inspector. In Fig. 3.22 we see two possible CTFs and two possible MTFs of an image. The area MTFA in between both curves describe which details can be detected and recognized in an inspection.

The human eye is able to detect 10 orders of magnitude of luminance of visible light ($\Delta\lambda$= 400 - 800 nm) considering the adaptation under low light level. But only about 200 brightness levels can be distinguished, which has direct consequences for the visualization of data. Displaying data with a dynamic range larger than 8 bit requires contrast variation tools or false color palettes. The perception of brightness by the human eye goes logarithmical (Fig. 3.23) analogue to the perception of sound by the human ear. The human ear can measure 13 orders of sound intensity of sound waves (Δf= 20 Hz - 20 kHz). The better sensitivity for higher luminances should be considered during an inspection, for instance

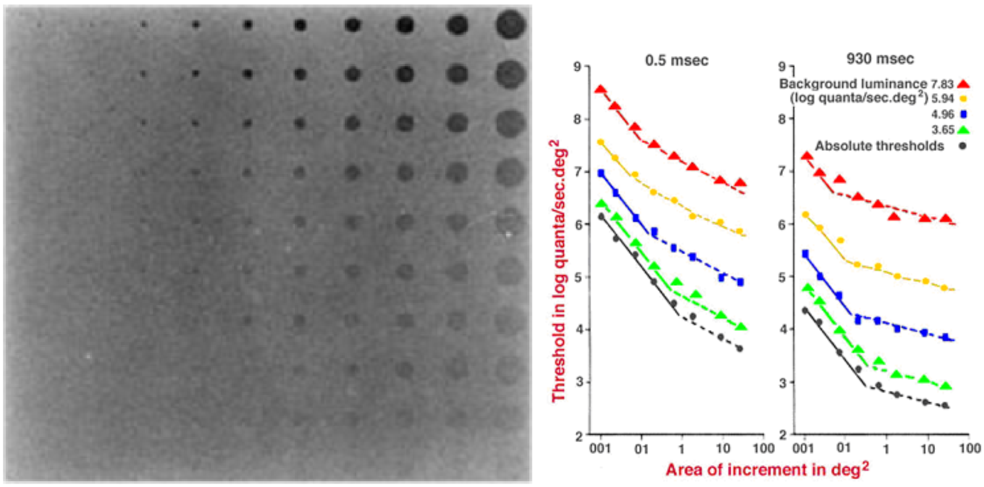

Figure 3.21: Test pattern (left), Spatial summation of the human eye (right) [Kol05, 20]

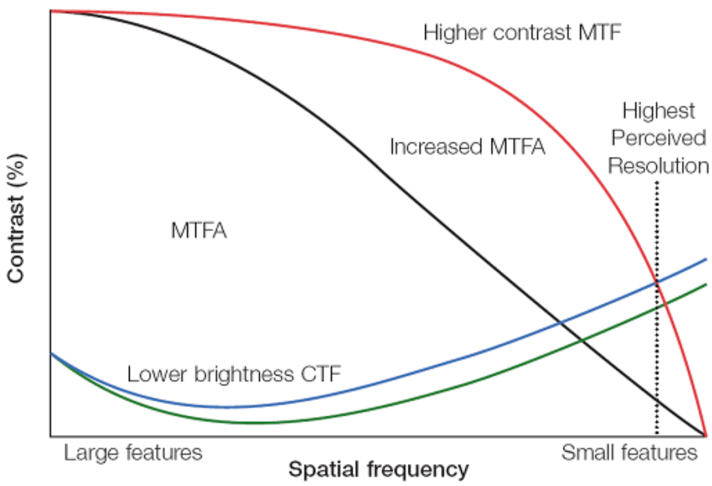

Figure 3.22: Detectable details in an image

by inverting images or by using non linear contrast variation methods (like gamma correction). In the medical field the human body is inspected in the form of inverted X-ray radiographies (negative images) because the bones give higher contrast.

The human eye and the human brain are capable of much more complex tasks. They are for instance optimized for edge detection and object recognition. This leads to "artefacts" in human vision like contrast enhancement near brightness variations and even completion of partially hidden object and structures. In Fig. 3.24 we recognize stronger contrasts near the edges a and an illusionary white square.

Since there is a finite amount of time required to collect and process information, there are limitations to the responsiveness of our visual system to rates of change, Fig. 3.25. For the detection of a flash of light the integration time is to 100 ms for rods and 10 to 15 ms for cones and the eye appears to be most sensitive to a frequency of 15 to 20 Hz. For low light levels the integration time is minimal at 100 ms and best at frequencies of 5 Hz.

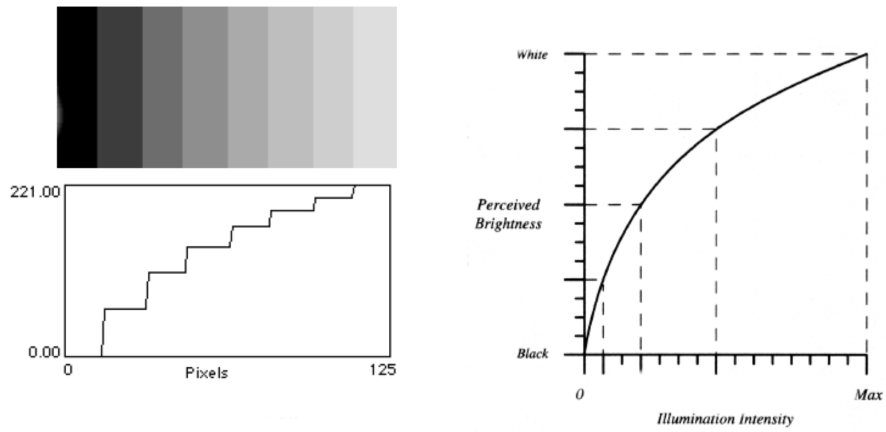

Figure 3.23: Logaritmical perception of the human eye [Kol05, 20]

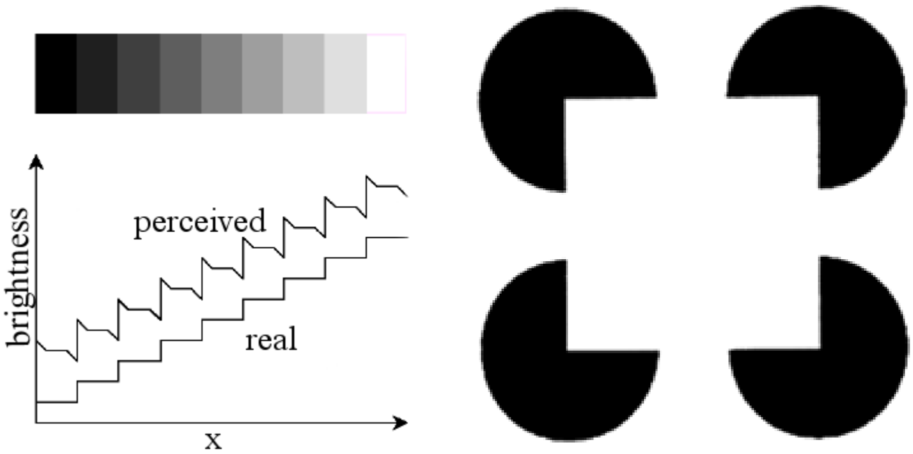

Figure 3.24: Mach bands and (left), illusory contours (right) [Kol05, 20]

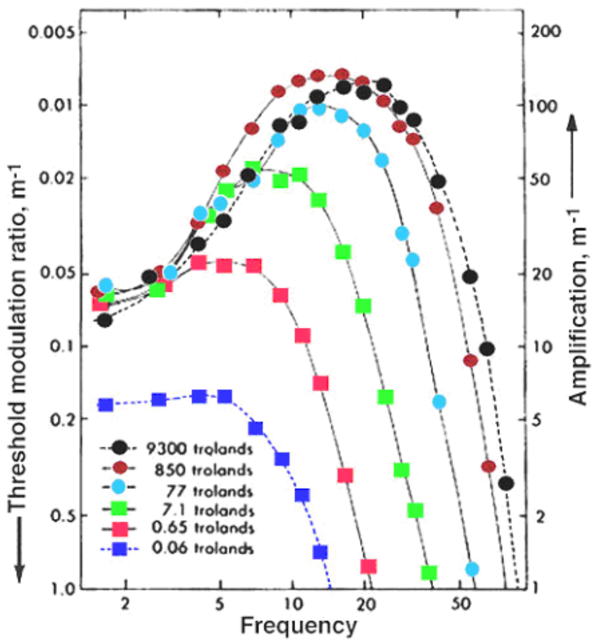

Figure 3.25: Temporal contrast sensitivity of the human eye [Kol05, 20]

Chapter 4

Measurements

Within this work two experimental methods were developed: stroboscopic NR and energy selective time of flight NR. Both techniques are described in this chapter and experimental results are presented. In the case of stroboscopic NR combustion engines and an injection nozzle were investigated at the Paul Scherrer Institut, at the Institute Laue Langevin and at the new neutron source FRM-II with different detectors systems. The presented energy selective time of flight NR experiment was a proof of principle experiment and was carried out at the pulsed spallation source ISIS.
The final section of this chapter is dedicated to the quantitative data evaluation. At KFKI the cooling liquid of a refrigerator was inspected and in the NR series the volume of the cooling liquid in the buffer of the freezer box was calculated for every frame of the series.

4.1 Stroboscopic NR: Combustion engines

Stroboscopic neutron imaging is a new technique developed at the Technische Universität München within this work. At high flux neutron sources typical integration times for a single 16 bit NR image are around 100 to 1000 ms. The time resolution for dynamic neutron radiography -or neutron radioscopy- is given by the neutron integration time plus the readout time of the CCD. That leads typically to a time resolution Δt of a few seconds.
For cyclic processes the periodicity allows the synchronization of detector and process. Identical NR images from the same time window of the process can be acquired stroboscopically. By summation of n images either on chip or after readout by software a time resolution down to the ms and sub ms range is reached. The quality of the image is the same as for a NR image with a n times longer integration time. By shifting the phase of the trigger signal the time window can be shifted and finally a NR movie can be composed.
An ideal object of investigation for stroboscopic neutron imaging are combustion engines. Combustion engines are an active field of research. The aims are their optimization and improvement through more power, longer lifetimes, lower weight, lower production costs, less fuel consumption, less exhaust gases. There are still unanswered questions at ms time scales like the oil distributions, the fuel injection or the movement of the piston rings, which can hardly be simulated. The robust, metallic motor block makes it very difficult to observe the physical processes inside with classical NDT methods. Spot sample measurements are the only way to get access to physical quantities like oil pressure and oil density. Optical windows open the door to many optical methods like "Schlieren" - images and shadowgraph techniques, which deliver information about fuel concentration. Light scattering methods as Laser Doppler Anemometry and Phase Doppler Anemometry can determine position and velocity of droplets. Spectroscopic methods give access to position

sensitive chemical composition and temperature information. For more detailed information see [Sfb05, 25]. However, with these methods the system is disturbed and the real conditions like temperature, pressure and chemical environment can never be achieved.
Before stroboscopic NR is established as a standard inspection method feasibility studies must be done and pioneer experiments must prove the opportunities of the method. NDT questions, which can be followed up with neutrons are:
-What is the distribution of the lubrication liquid inside a running combustion engine (piston cooling, piston lubrication, backflow of the oil in the oil pan, oil transport to the bearings)?
-How does the fuel injection occur inside a real system under real conditions?
Neutron imaging gives us the possibility to answer these questions because of two reasons:

1. the large penetration depth of neutrons for many metals, especially aluminum often used for the motor block

2. the high total neutron cross section of hydrogen, and hydrogenous substances like fuel and oil in the case of a combustion engine.

4.1.1 First NR of a running combustion engine

After the method of stroboscopic imaging was proven to work [Bru01, 31], in the year 2002 for the first time a self running combustion engine was investigated by stroboscopic neutron imaging. For the four stroke 480 W model air craft engine of the company OS (Fig. 4.1) a test stand was prepared. The engine runs with nitro fuel at 4800 rpm.

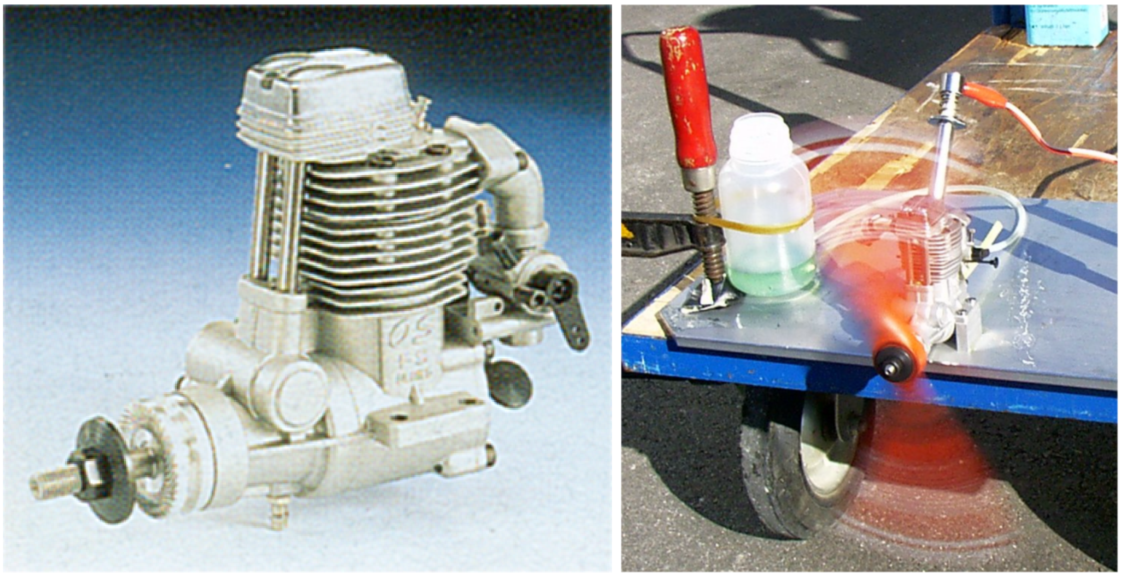

Figure 4.1: Photograph of the model aircraft combustion engine

The preparation of the test setup for stroboscopic imaging is time consuming. A reliable and stable triggering signal for the synchronization of motor and intensified camera is needed. Normally an inductive sensor generates a TTL signal every time a piece of metal passes at a maximal distance of 2 mm. A small screw, mounted on the rotor, gave a stable electrical signal between 0 V to 5 V for the camera triggering. In the first experiments an external delay generator was used, later the delay was generated by the camera software. It is not trivial to get this kind of engine running and an electric starter is proposed for future experiments. Although the power of the engine is not huge,

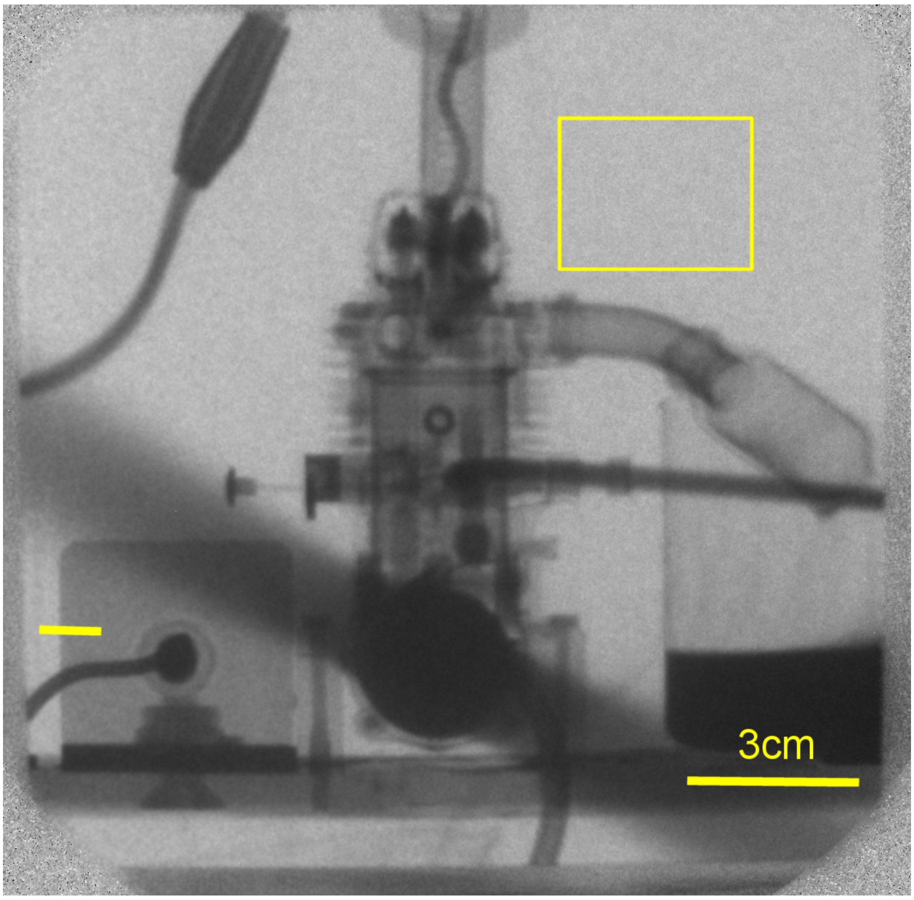

Figure 4.2: Single frame of a neutron radiography movie of the model air craft engine in Fig. 4.1, Δt = 250 μs with 4000 accumulations, Δx=0.75 mm, σ=1.7%

the air movements are 2 m^3/s. The fast moving rotor of the engine is dangerous and must be handled with care. The exhaust gases should be filtered form the unburned fuel in order to prevent pollution of the experiment.

The running engine was imaged at position 2 of the NEUTRA facility [PSI05, 27] in 2002. At a thermal flux of 7.5$\cdot$10^6 n/cm^{2}s and L/D = 350 a typical accumulation time at NEUTRA is 100 ms. With the stroboscopic technique a much better time resolution is possible and an exposure time of 250 μs was chosen. 4000 images of the same phase were summed up in total, 400 were integrated on chip and 10 individual images were added by by software after readout. One cycle of 12.5 ms was subdivided into 50 frames with 250 μs exposure time each. The detector was a cooled and MCP intensified CCD camera PI-Max in combination with a 300 μm thick ^{6}LiFZnS converter from the company AST. The result is shown in Fig. 4.2: one single frame out of the neutron radiography movie [ppt1, 42]. The environment of the small engine consists of the trigger sensor mounted perpendicular to the rotor plane, the glow plug on top of the engine, the exhaust pipe, a small pot for the exhaust gases and the black strongly attenuating fuel supply tube. In addition to the piston and the valve movements small changes in the lubrication distributions are visible (see 4.3).

The image was characterized by measuring the relative noise σ in the open beam in the rectangle in the image and the spatial resolution was estimated via an ESF measurement. After normalization the relative noise σ was measured to be 1.7% and the spatial resolution

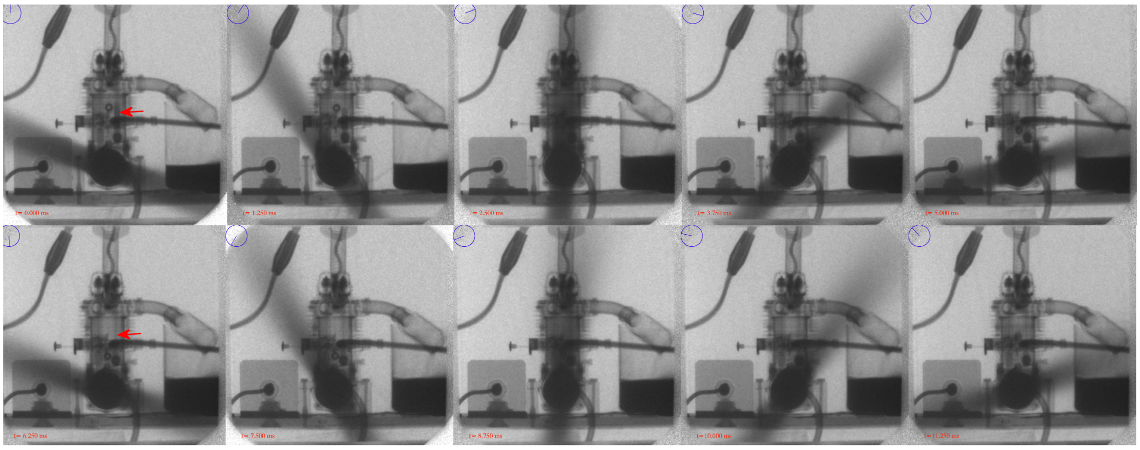

Figure 4.3: Dynamic neutron radiography frames of the movie, link to CD

Δx was 0.75 mm due to blurring caused by the beam divergency. The field of view was 15 x 14.7 cm^2 (1058 x 1038 pixels).
This experiment demonstrated that stroboscopic NI with a time resolution of 100 μs with acceptable quality is feasible. Oil movements inside the model aircraft engine were observed at this time scale. During the experiments it was realized that the test setups for this kind of measurements are very complex and require a long preparation time.

4.1.2 Car combustion engine

In a collaboration with the ILL, the University of Heidelberg and PSI a four-piston BMW combustion engine was inspected with the stroboscopic neutron radiography technique at the high flux test beam line H9 at ILL [ILL05, 28] in order to compare different facilities and detectors. The Neutrograph facility is described in [Fer05, 29]. The object is an original BMW four cylinder car combustion engine (Fig. 4.4) of the type NG4 with a motor block of aluminium. It is driven by a 2 kW electro motor mounted on a vertical translation stage below. The spark plugs were removed to reduce the drag. In this way a water cooling circuit is not necessary and no exhaust gases are produced, which must be controlled and cleaned. The vibrations of such engines may be critical, so that they should be fixed on appropriate bearings in order to prevent moving or even breaking of the engine. The identical system as in the measurement before was used: a MCP intensified CCD camera PiMax [Rop04, 12] with a peltier cooled chip and 16 bit digitalization. The usable dynamic range is limited by the inherent noise of the intensifier. The full cycle (duration 120 ms) of this four stroke engine running at 1000 rpm was split into 120 individual frames over 2 rotations: 150 individual images with a exposure time of 200 μs each were accumulated on chip. In this way the measuring time for the full run was in the order of 18 min only. In Fig. 4.5 above the first frame of the recorded movie is visible, showing valves, pistons, piston rods, piston pins and piston rings. Of special interest is the visualization of the piston cooling via an oil jet directed the piston bottom. Since the pistons are connected to the engine body only via the piston rings with very low heat dissipation, a continuous oil jet is directed from below to the piston bottoms, lowering the piston temperature by more than 200° C. In the movie [ppt1, 43] the dynamic oil distribution is clearly visible. Around the upper turning point of the piston, the oil movement at the piston bottom due to inertia was observed. The field of view was 21.5 x 21.0 cm^2. The observation area could by varied by displacement of the full set-up. The image characterization yielded a spatial resolution of 1.8 mm and a relative noise of 2%. The spatial resolution is so

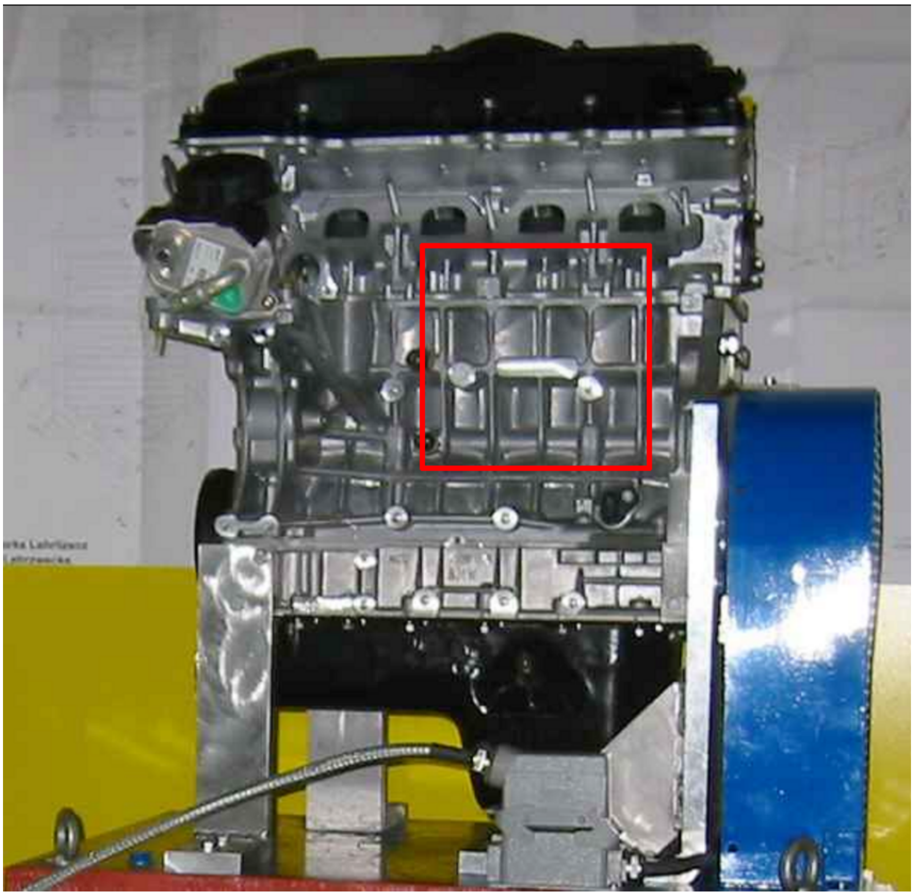

Figure 4.4: Photograph of the BMW combustion engine, the red rectangle is the FOV for the NR

moderate due to the beam divergency in combination with the large distance between the object and the detector, but the noise in the most homogeneous area, the beam center, is very low considering the low integration time. In Fig. 4.5 the new visualization technique was used: a NR frame was overlapped with a difference image (in false colors) between that frame and a second frame of different position in time. The green and the blue color mean less attenuation, the yellow and red color mean more attenuation in the second frame. Before the subtraction operation the piston was tracked along its movement in the cylinder. However, difference images always show artefacts. Regions of interest with a different attenuation result in a diverse noise level and different offsets in the grey level results in a false color offset of the difference image. The piston is in the upper turning point and the oil (yellow spot) is moving from right to left because of the inertia and the special form of the piston bottom. The green stripes show how the oil disappears during the up-movement of the piston.
This experiment confirmed that the stroboscopic NR method has the potential for inspection of the lubrication circuit in large car combustion engines made of aluminium.

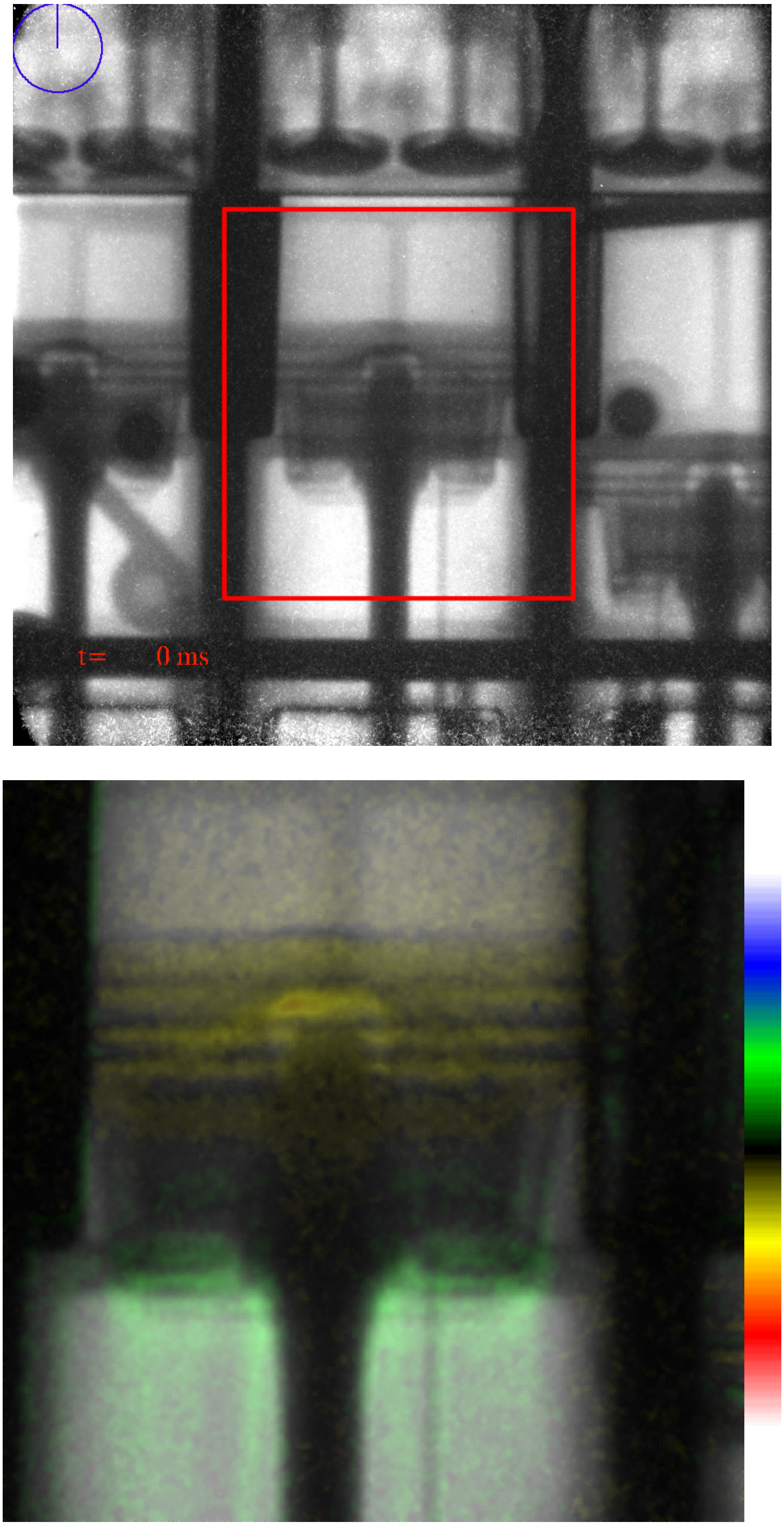

Figure 4.5: NR frame of a dynamic NR movie of the running engine (above): Δt = 200 μs with 150 accumulations, Δx=1.8 mm, σ=2%, FOV: 21.5 x 21.0 cm^2; ROI of the piston (below) overlapped with a difference image of two NRs at different position in time in false colors: the oil inside the engine is visible

4.1.3 Injection nozzle

After the first measurements with combustion engines, it was realized that it would be very difficult to see the fuel in a running engine. So, the decision was taken to try with a commercial fuel injector as a next step. Apart from fuel injection systems high pressure sprays are an essential technology with many other applications as thermal and plasma spray coating and liquid-jet machining. Liquid sprays are difficult to investigate because of the fast time scale and the slight density changes in respect to air. Using flash lights shadow - and reflection images can be obtained but no real density profile across the liquid cloud can be measured. Recently radiographic studies of spays were performed with X-rays and synchrotron radiation [Mac02, 30]. In the automobile industry common rail diesel injectors are state of the art and were purchased. An appropriate test stand (Fig. 4.6) was provided by the company Bosch.

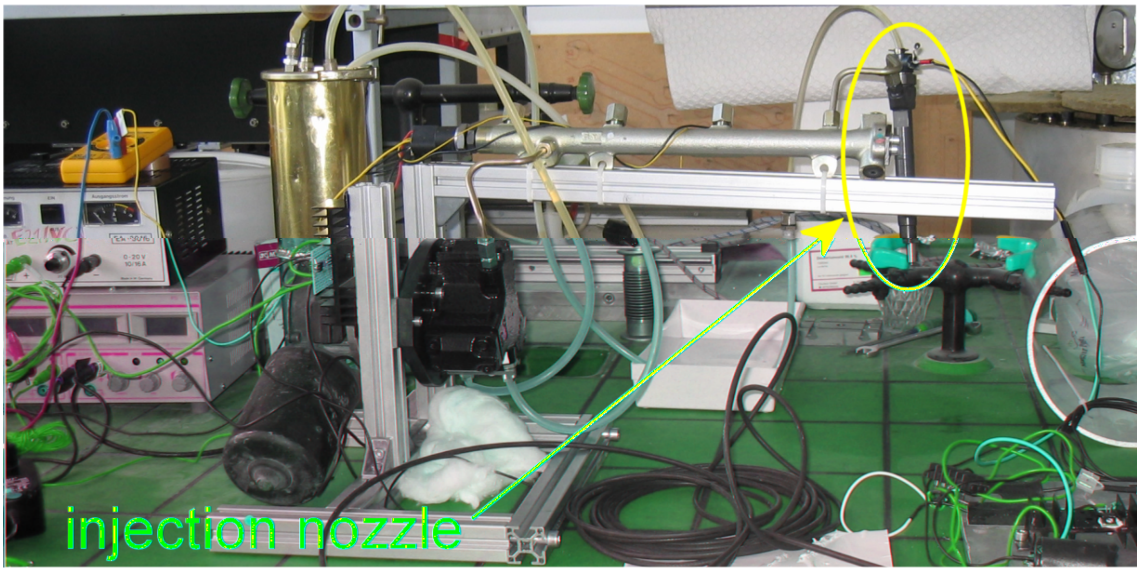

Figure 4.6: Diesel injection setup for neutron radioscopy

The injector is mounted on one of the four positions of the pressure rig. The oil pressure can be adjusted between 0 and 1200 bar by the current of the high pressure pump. Injection nozzles in the car have several holes which inject the fuel clouds very homogenously. During the experiments a common rail diesel injection nozzle with one single central hole of 0.2 mm diameter and a pressure up to 1000 bar was inspected. Safety precautions were taken to prohibit contact with the oil jet. It can penetrate the skin or even cut a finger and poison the human blood circuit. The oil, a special non flammable oil with a viscosity similar to Diesel fuel is used as fuel substitute and arrives from the small tank via a pre pump and a high pressure pump to the high pressure rig. After longer operation times of the nozzle the produced oil fog can disturb the measurement. The nozzle needs a voltage of about 100 V in order to open the electronic valve and a current of 2 A to keeps it open. A special power electronics with a high voltage cap and a power MOSFET was used for this special task. The NR detector and the nozzle are triggered with the same electronic TTL pulse. The pulse frequency must be lower than 20 Hz to keep the pressure in the rig constant.

At the beam line H9 at ILL the very high flux of $3.2{\cdot}10^9$ n/cm^{2}s gives optimal conditions for short exposure times. The detector system at ILL uses a Sensicam, an Interline Transfer CCD camera of the company PCO with a fast shutter option. The injector was triggered

with about 20 Hz and kept open for 1 ms. The CCD camera accumulated 5000 images synchronous to the injection process.
In 2003 the fast injection process of a high pressure nozzle was observed for the first time with neutrons (see Fig. 4.7).
The injection cloud was observed in 5 steps of 100 μs each. The lack of a sharp edge

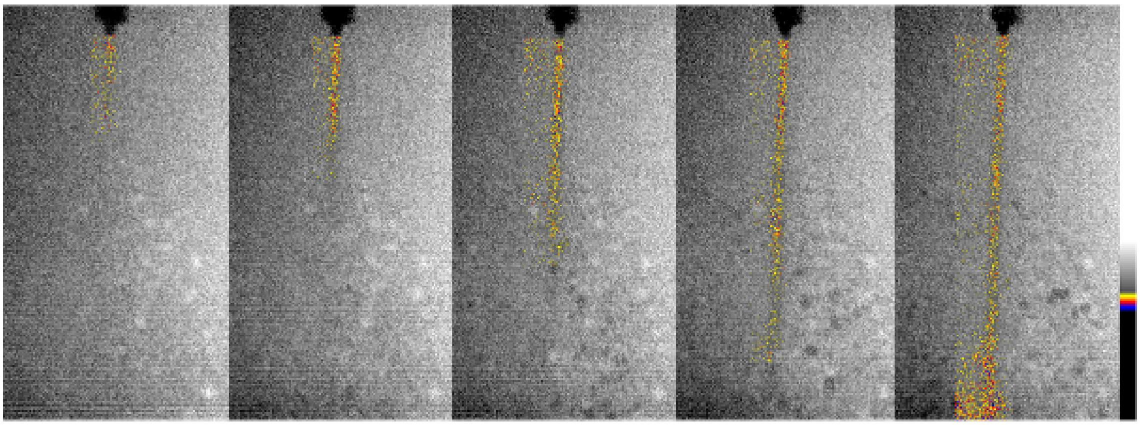

Figure 4.7: First neutron radiographies of the injection process, t= 500 μs, 600 μs, 700 μs, 800 μs, 900 μs, Δt = 100 μs with 5000 accumulations, Δx=1.0 mm, σ= 0.28%

in the image allows only a rough estimation of the spatial resolution. From the profile of the cylindrical nozzle the spatial resolution is estimated to be 1 mm, at a time resolution Δt of 100 μs. This agrees with the PSF estimation based on the L/D ratio of 150 of the neutron beam and a distance object to detector of about 150 mm. Some problems were encountered: The injection chamber filled up with an oil fog and on the aluminum windows oil drops formed, the scintillator efficiency was not homogeneous because of the scintillator deterioration, the noise level was very high and has a line structure and the right side of the NR images is brighter for an unknown reason. The measurement was continued with the following improvements:
- Data images and open beam images were taken alternatingly by simply triggering the camera with twice the frequency of the nozzle.
- The dark current correction was optimized.
- More images were accumulated.
- The data evaluation and visualization were optimized and automatized.
The last experiment was continued at ILL by Martin Engelhardt [Eng04, 33] and Andreas Hillenbach. The best results are presented in Fig. 4.8. High pressure injections of fuel were investigated with neutrons for the first time. The best results have a spatial resolution of 1 mm and a relative noise of 0.2%. Up to now the injection in a running engine was not visualized. It may be possible to see the fuel in near future but the spatial resolution will not be high enough to optimize the injection process with NR.

The visualization of the injection cloud was a real challenge. The position in time of the nozzle opening is delayed by 500 μs in respect to the rising edge of the triggering signal and the attenuation of the fuel cloud is below 0.25%. Thus, it is an ideal sample for the check of NR image quality and in fact a lot of methodical improvements resulted from these experiments.

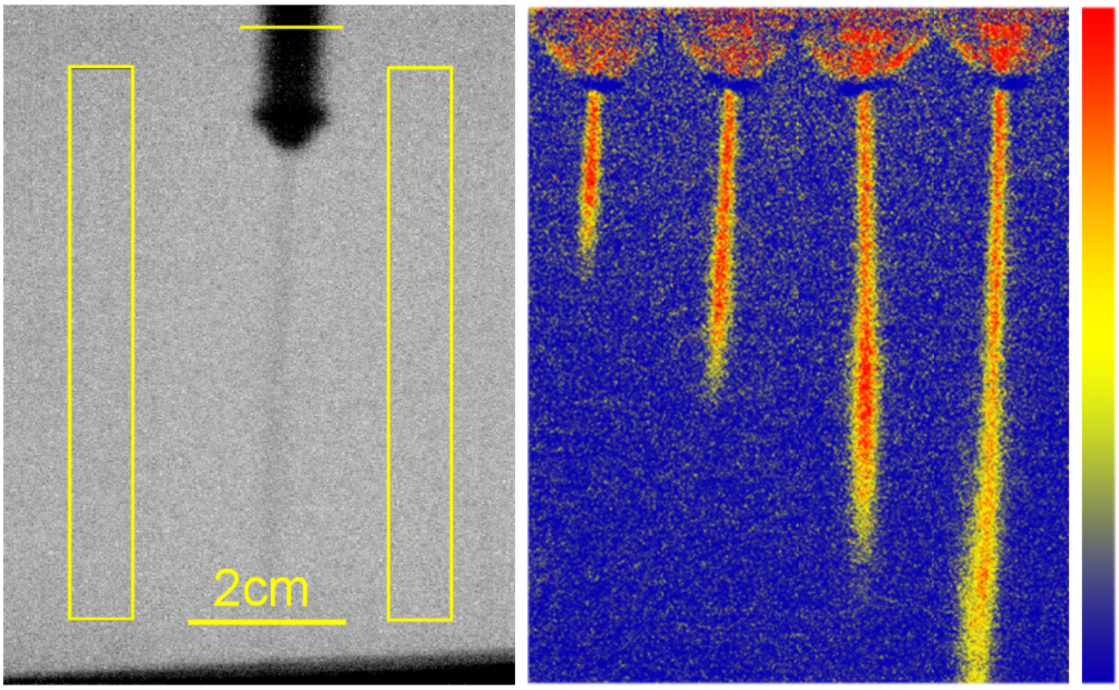

Figure 4.8: NR image of the injection nozzle in action (left): Δt = 100 μ s with 12000 accumulations, Δx = 1.0 mm, σ=0.44%, FOV: 62 x 83 mm^2;
NR series of the injection process at 350 bar (right): t=500 μs, 600 μs, 700 μs, 800 μs , Δt = 100 μs with 12000 accumulations, Δx =1.0 mm, σ=0.2%, FOV of each injection: 10 x 50 mm^2 (640 x 127 pixel), blue no attenuation, yellow 0.4% attenuation, red 0.8% attenuation

4.1.4 First neutron radioscopy of an combustion engine at FRM-II

Finally, in December 2004 in the first reactor cycle of the FRM-II it was possible to perform the first stroboscopic NR experiment of a Diesel current generator (Fig. 4.9) at the ANTARES facility.

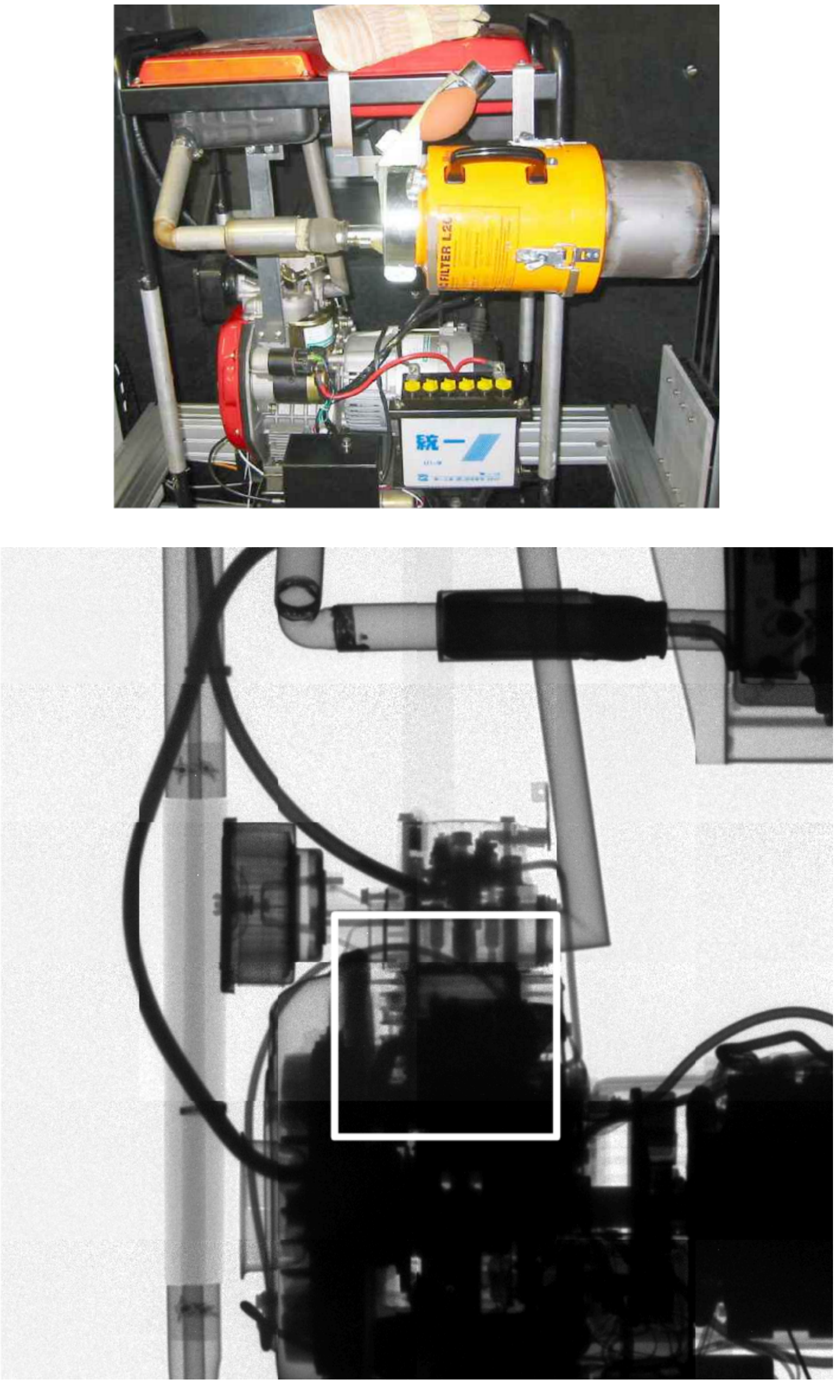

Figure 4.9: Direct injection diesel generator test setup for dynamic neutron radiography (above), NR image composed from 16 single NR images (below)

Before the start of the experiment the generator was modified in the following way: On the exhaust pipe a filter (yellow cylinder) was mounted, which is normally used for trucks driving into closed rooms or buildings. The filtered exhaust gases were conducted in the

exhaust air pipes of the experimental hall of the FRM-II. Furthermore many parts of the generator as the exhaust tube, the tank, the starting motor were displaced or completely removed such that no unessential parts are exposed to the high neutron flux. For security reasons only a limited amount of fuel was left in the tank and with a surveillance camera the experiment was carefully watched. Before the dynamic radiography run the generator was scanned by translating it on the sample manipulator and 16 single NR images with a respective field of view of 144 x 144 mm^2 and 1024 x 1024 pixels were composed to a big one with a size of 658 x 658 mm^2 and 4682 x 4682 pixels (Fig. 4.9).
For the stroboscopic measurement the starter motor was removed to get a better transparency of the motor block. The four stroke direct injection diesel generator runs with 3000 rpm, 50 Hz. That is 20 ms for each revolution and 40 ms for each cycle. As a detector the ICCD camera with 1024 x 1024 pixels was used. The settings of choice for imaging were 1 ms accumulation time and 1500 on chip accumulations per frame for each of the 40 frames. Because of radiation safety reasons at the time of this first experiment the small collimator could be used with a smaller flux of 2.5·10^7 n/cm^2 s only. The total measuring time was about 3 hours. The result is visible in Fig. 4.10.

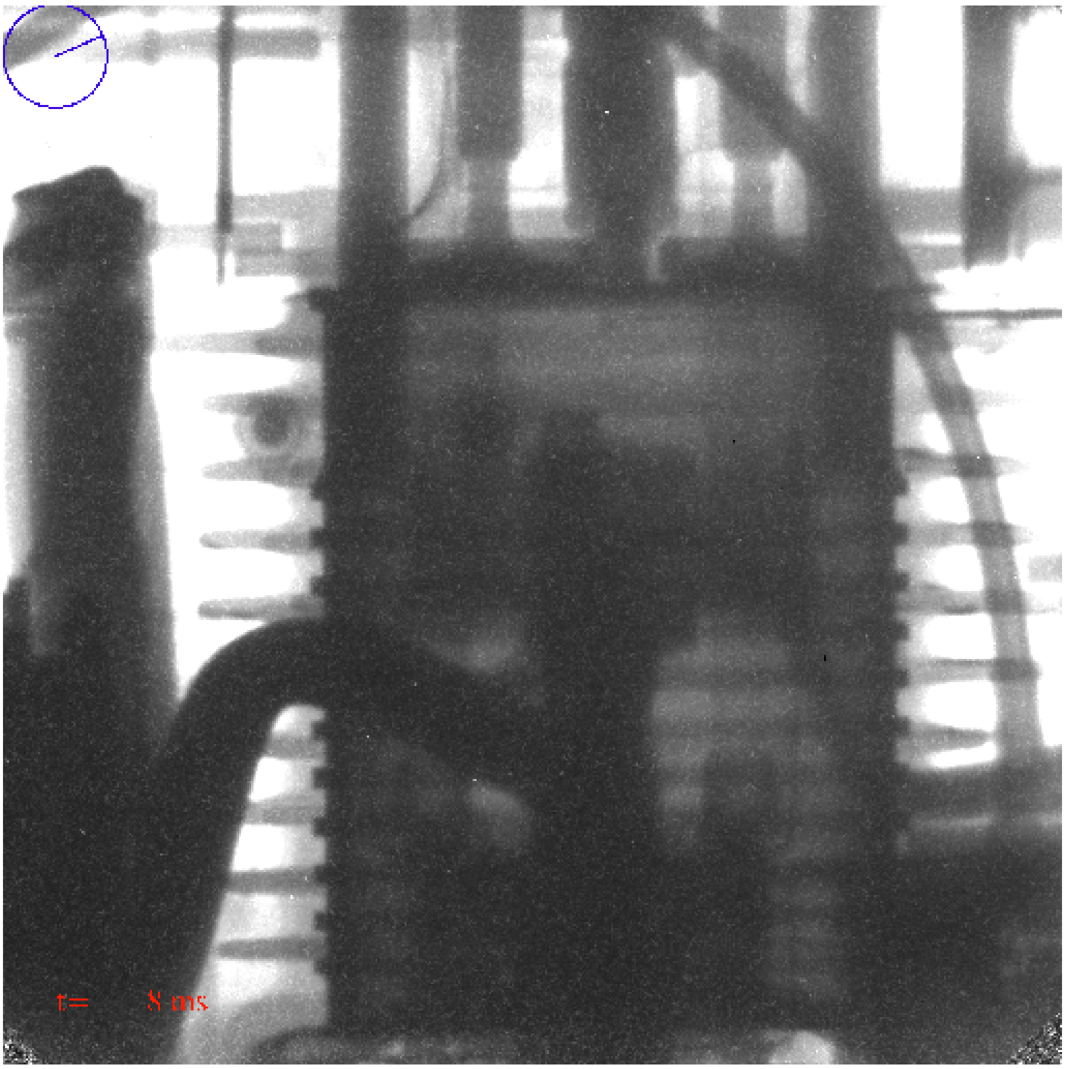

Figure 4.10: One frame of the NR movie [ppt2, 44] of the generator measured at FRM-II for the first time: Δt = 1 ms with 1500 accumulations, Δx = 1.0 mm, σ = 2.5%, FOV: 144 x 144 mm^2 (1024 x 1024 pixels)

A NR movie was composed [ppt2, 44]. The spatial resolution is 1 mm and the relative noise is 2.5%. Aims for the future are a longer accumulation time with the big collimator and the optimization of the spatial resolution. Attaching an electrical load like a heater to the generator it should be possible to visualize the fuel injection because of the increased amount of injected fuel.
The ANTARES facility is perfectly suited for dynamic neutron imaging because of the high neutron flux and the high spatial resolution. Due to the cold spectrum the facility allows the inspection of thinner and less attenuating objects in comparison to thermal facilities do. The experimental setup for stroboscopic NR as well as the evaluation software was successfully tested for the first time with satisfactory result.

4.2 Energy selective time of flight NR

By imaging an object at different neutron energies additional information can be obtained. The contrast changes reflect the energy dependent cross section of a material and allows in the best case material discrimination. Practically there are five possibilities for a neutron spectrum variation:

- Different moderators or variation of the moderator temperature: A neutron spectrum is mostly a Maxwell distribution with the temperature of the moderator medium as the main parameter.

- Monochromators are quasi perfect crystals, which reflect a small part (about 1%) of the neutron following the Bragg equation.

- Filters attenuate parts of the neutron spectrum according to the cross sections of the constituent nuclei. A clear change in the spectrum is only reached with filters working in a resonance regime. The thicker a filter is the better is the energy discrimination, but the more neutrons are absorbed and the lower is the transmitted flux. Filters are favored especially for fast spectra, where other methods are difficult to realize.

- A velocity selector is s high-speed turbine, which is transparent for those neutrons which manage to pass between the twisted lamellae inserted in the rotor in a time interval defined by the rotation speed of the selector. Thus, neutrons of a special velocity or energy are selected. Modern velocity selectors spinning with up to 30000 rpm, reach an energy resolution of $\Delta E/E \approx 30\%$.

- At pulsed neutron sources at a certain distance from the source a time of flight (TOF) spectrum can be measured due to the finite velocity of the neutrons. Immediately after the generation of the neutron pulse the gamma particles and the fast neutrons arrive at the sample position, later the thermal neutrons and finally at the end of the cycle before the consecutive pulse the cold neutrons arrive. Measuring the time between generation and arrival of the neutrons - the time of flight - and the flight path the neutron velocity can be calculated. Fast detectors allows an energy selective neutron measurements. At most time of flight instruments ^{3}He tubes are used as detectors.

The last method can be used for neutron imaging. ^{3}He tubes are not ideal for imaging because of their bad spatial resolution, but the detector for stroboscopic NR with the ICCD camera is. It has the excellent spatial resolution of a large area NR detector and an excellent energy resolution due to the gating properties of the intensifier.

By synchronizing this detector with the neutron pulses and shifting the phase of the triggering signal energy selection becomes possible. Many frames can be accumulated on the chip before the readout. The time between neutron pulse generation and the shutter opening of the camera defines the starting energy, the opening time of the intensified camera defines the energy windows (and the energy resolution). The minimal energy resolution ΔE of the detector is limited by scintillator decay time Δt_{sci}:

$$\Delta E = \frac{2E}{s}\sqrt{\frac{2E}{m_n}}\Delta t_{sci} \qquad\qquad \Delta E \approx 3.0 \cdot 10^4 \cdot \frac{\Delta t_{sci}}{s} \cdot E[eV]^{\frac{3}{2}} \tag{4.1}$$

For Δt_{sci} =80 μs and s = 15 m the energy resolution is $\Delta E \approx 0.16 \cdot E[eV]^{\frac{3}{2}}$. The efficiency of scintillator is energy dependent too, the cross section of ^{6}Li in the thermal region follows the $1/\sqrt{E}$ behavior (see Fig. 1.7). A normalization for all energies accounts for this.
The ability to distinguish between two materials is mainly determined by the difference in their energy dependent cross sections and the available neutron flux. Resonances in the high energy regime (MeV), but also Bragg cutoffs at cold neutron energies (in the meV regime) are mostly used for energy selective NR.
The proof of principle experiment for this method was carried out at the spallation source ISIS, at the Rutherford Appleton Laboratory, near Oxford in UK (see Fig. 4.11). The repetition rate is 50 Hz and the duration of the pulse is 20 ms. The measuring position at the HIPR experiment at the ENGIN beam line was at a distance of about 15 m from the liquid methane moderator at T = 100 K. The spectrum has a maximum near 2.0 Å (see Fig. 4.11) and the total flux is about 10^6n/cm^{2}s.

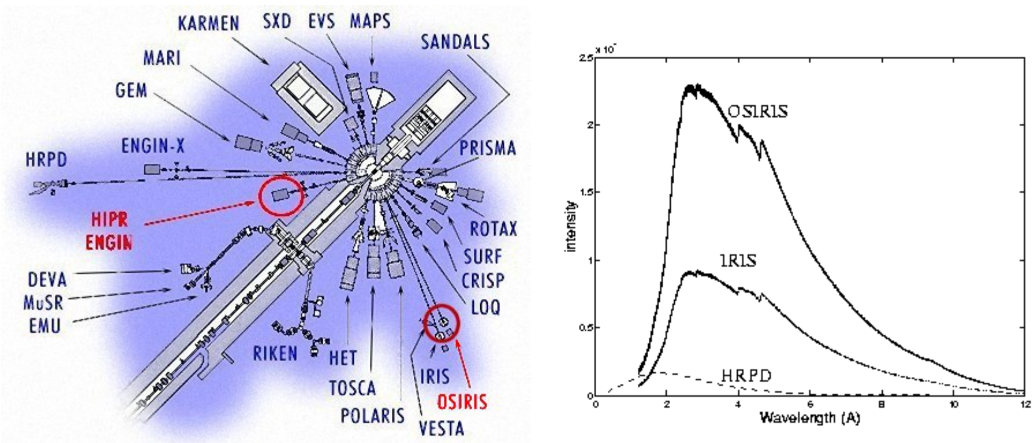

Figure 4.11: Instrumentation overview at ISIS (left), Rutherford Appleton Laboratory, time of flight intensity spectrum (right) plotted versus time of flight.

A detector with an MCP intensified CCD camera PIMax [Rop04, 12] was applied. The trigger input of the camera was connected to the synchronization signal of the spallation source. The selection of the energy band and the number of accumulations was done via camera software. The beam diameter was about 8 cm and varied with the energy. The divergency, determined by neutron guide, was not negligible and the distance between object and detector was reduced to the minimum in order to improve the spatial resolution. From equation 1.1 and v =s/t (v is the speed, s is the flight path and t is the time of flight of the neutron) follows in our case: $\lambda\left[\text{Å}\right] = t\,[ms] \cdot 0.24$. The maximal resolution due to the scintillator was 0.02 Å. A standard NDg neutron scintillator of the company AST was

used.
The first sample was a strongly absorbing Gadolinium foil of 5 x 5 cm^2 with a star pattern. The idea was to determine the spatial resolution of the set up and to verify the energy dependent contrast. NR at three different energies are shown in Fig. 4.12.

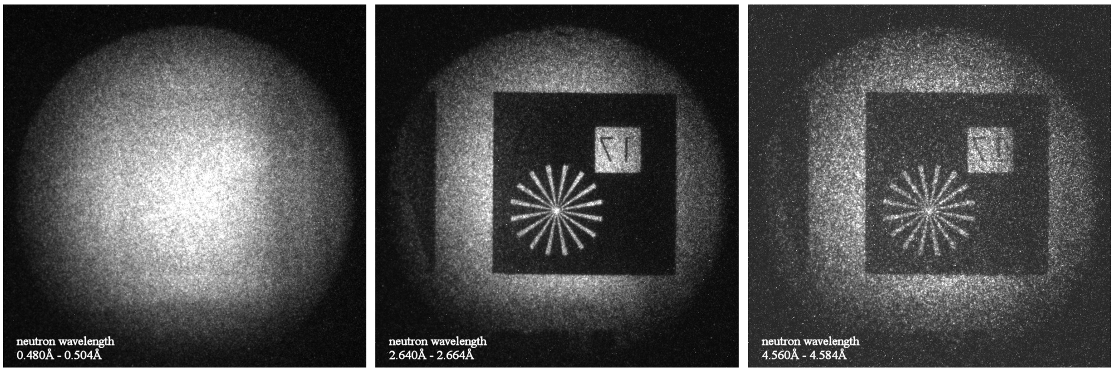

Figure 4.12: NR images of a Gd-Foil with a star pattern at three different energies: at 0.48Å, at 2.64Å and at 4.56Å: Δt = 0.1 ms with 20000 accumulations, Δx =0.5 mm, σ=10-30%, FOV: 161 x 166 mm^2 (1300 x 1340 pixels)

Since the neutron flux is not the same for the different energies the NR images must be normalized. The reason for the different contrast of the foil in the three NR in Fig. 4.12 is the energy dependent neutron cross section of the material of Gadolinium. At high energies the foil is not visible at all, while with lower energies the attenuation increases and the foil appears. The neutron attenuation of the foil for all measured energies is displayed in Fig. 4.13.

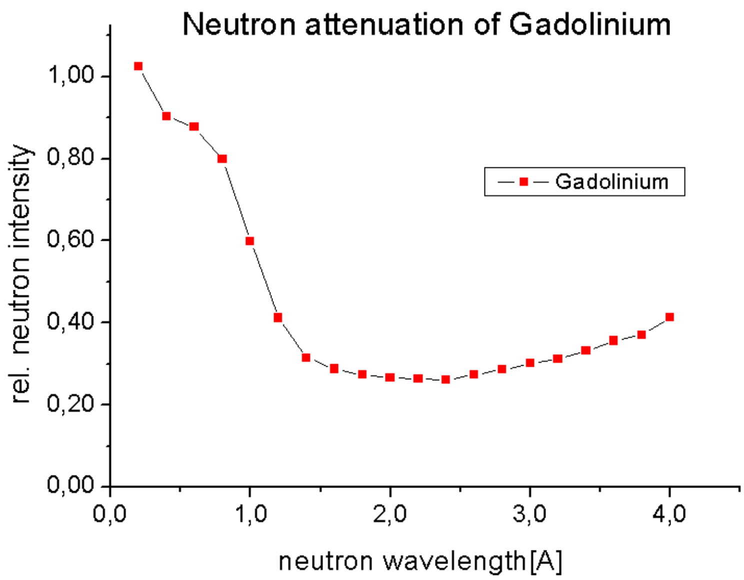

Figure 4.13: Neutron attenuation of a Gd foil at varying energy

According to the cross section of Gadolinium (Fig. 1.7 in chapter 1) an exponential increase up to 1.2 Å and a slower increase in the attenuation at longer wavelengths is expected. The increase in the thermal region is clearly visible, but for cold neutrons the attenuation decreases again. That can be explained by the low cold neutron flux and the high noise level.

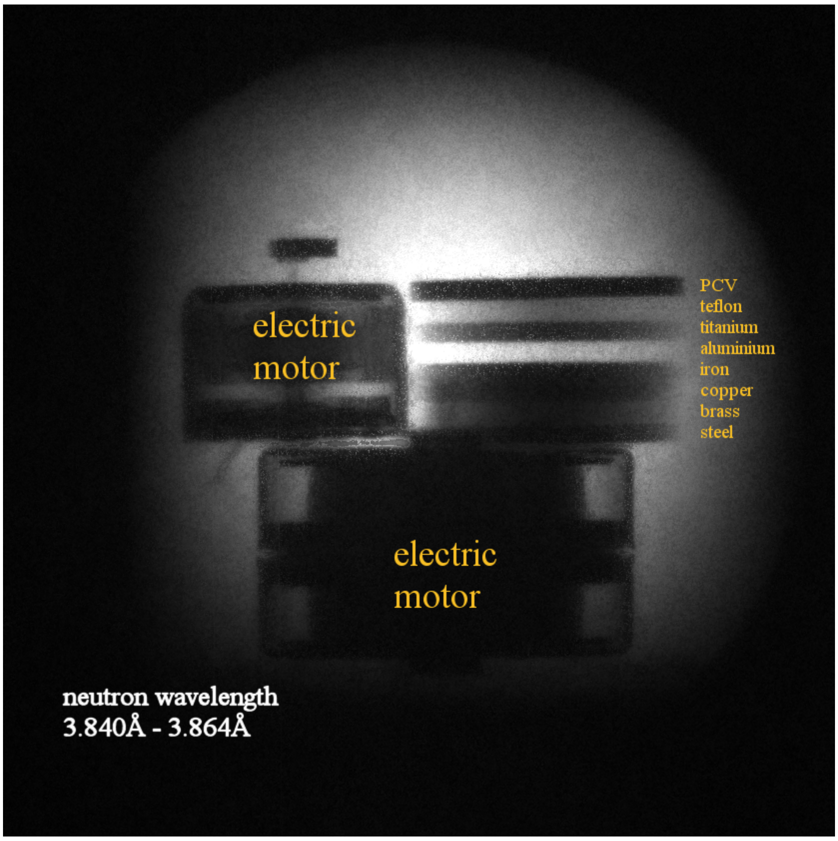

Figure 4.14: Energy selective NR image of two electric motors and a material stack: t=16 ms, Δt= 100 μs with 40000 accumulations, σ= 10-30%, Δx =0.5 mm, FOV: 100 x 100 mm^2 (833 x 833 pixel)

The second sample is visible in Fig. 4.14. A stack of materials should proof the ability to discriminate materials and two electric motors should serve a test objects. The material from top to bottom are: PVC, teflon, titanium, aluminium, iron, copper, brass and steel. Fig. 4.14 shows a NR of the objects.

A NR series of 39 images , starting with wavelengths between 3.840 and 3.864 Å and ending with wavelengths between 4.742 and 4.766 Å, was recorded, [ppt3, 45]. For some materials of the stack the rapid changes in the attenuation coefficients Σ near the Bragg energy (Bragg cutoff) were observed. Since Bragg cutoffs are determined by the lattice type and the lattice parameters they are characteristic for each material. The changes in Σ from one energy to the next were visualized in the form of difference images (see Fig. 4.15). In the false color difference images the contrast changes are visible in the green, blue and white color. Because in the difference image alone the position of a characteristic material relative to the object sometimes is not clear, it was fused with a NR image (see Fig. 4.16). Iron can be distinguished best from the other elements because of its large Bragg cutoff. The iron parts of the electric motor appear brighter and prove that it is possible to resolve a materials position sensitively. In order to obtain the best contrast, one energy above and below the Bragg cutoff should be used. The method is not limited to iron but can also be applied for the detection of other elements like copper or brass, Fig. 4.17. A necessary condition for the material discrimination is the polycrystalline solid state which most metals have. Because of the low neutron flux and the short measurement period the camera parameters could not be optimized and the statistics are moderate. In a time window of 1 ms about 1000 counts were registered by the detector.

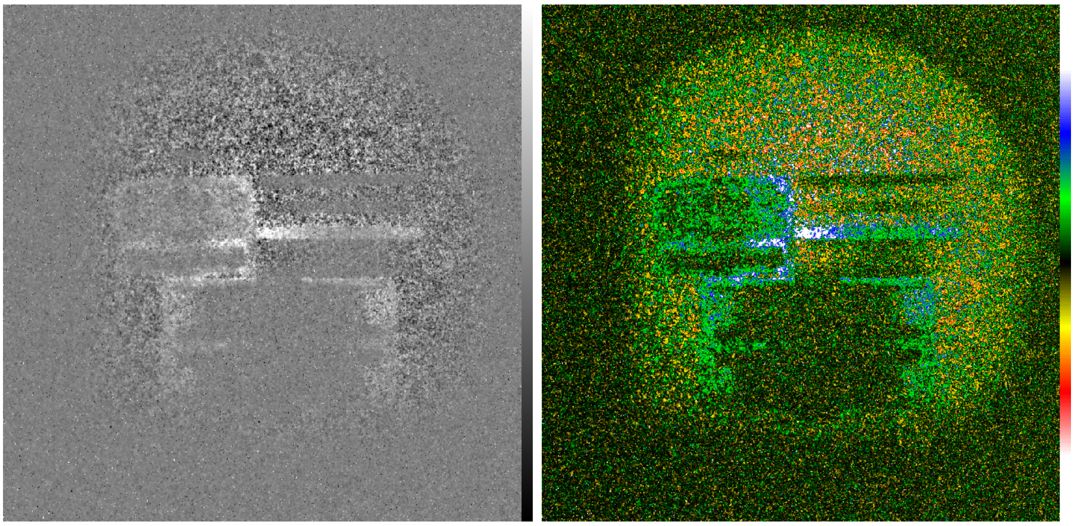

Figure 4.15: Difference images of two NR images: in black and white (left) and in false colors (right)

The uniqueness of this technique is the combination of an excellent energy resolution of time of flight with the good spatial resolution of a large area NR detector. After these promising results a consecutive experiment was planned and prepared. The beam lines IRIS or OSIRIS offer higher flux by a factor of 10 and a cold spectrum from a liquid ^{2}H moderator at 22 K. Unfortunately the complete beam time was cancelled due to problems with the accelerator coils.

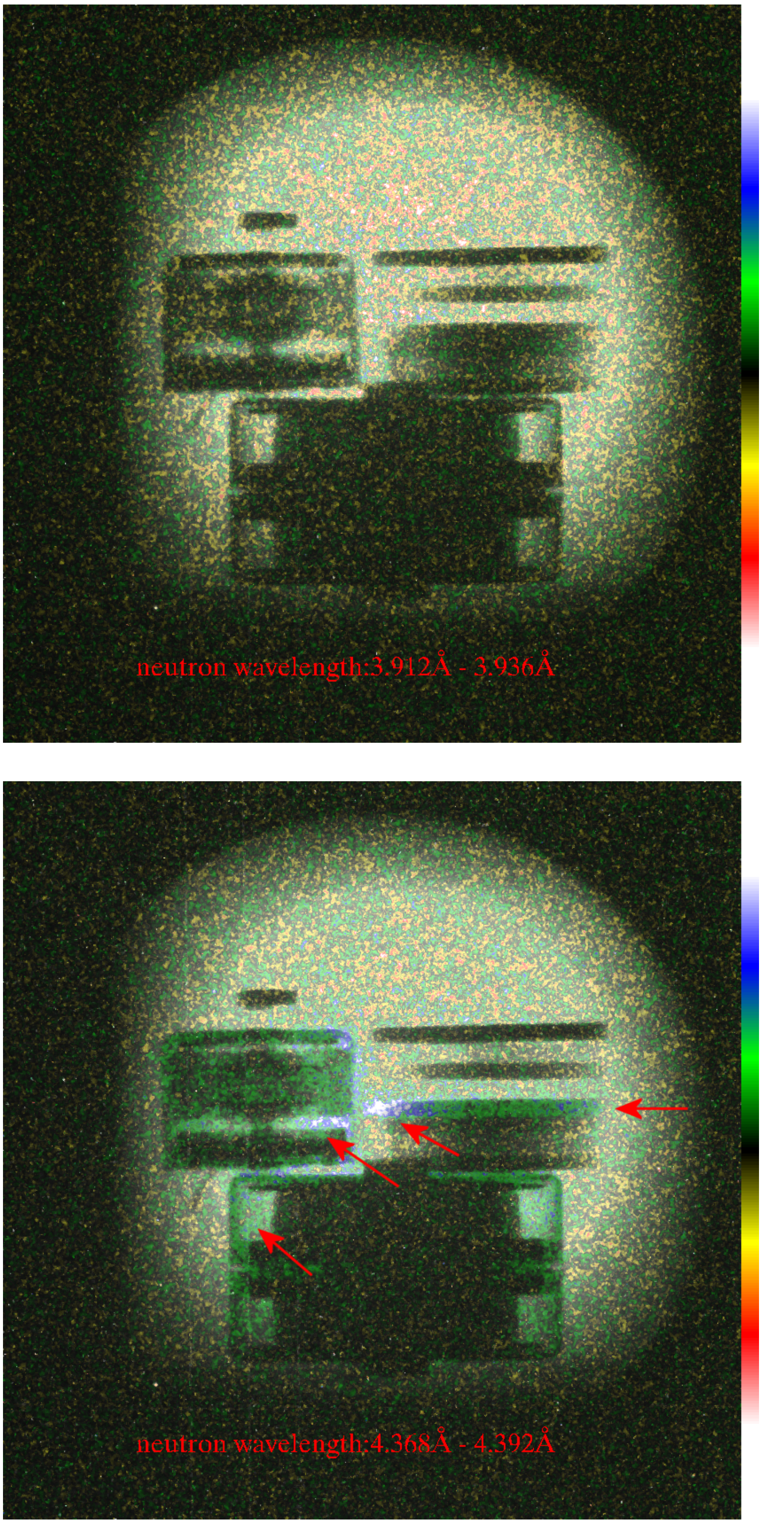

Figure 4.16: Difference of two NR (above) at 4.368 Å and 4.392 Å, difference NR highlighting the iron (below) with the green color in the image stack as well as in the housings of the two electric motors

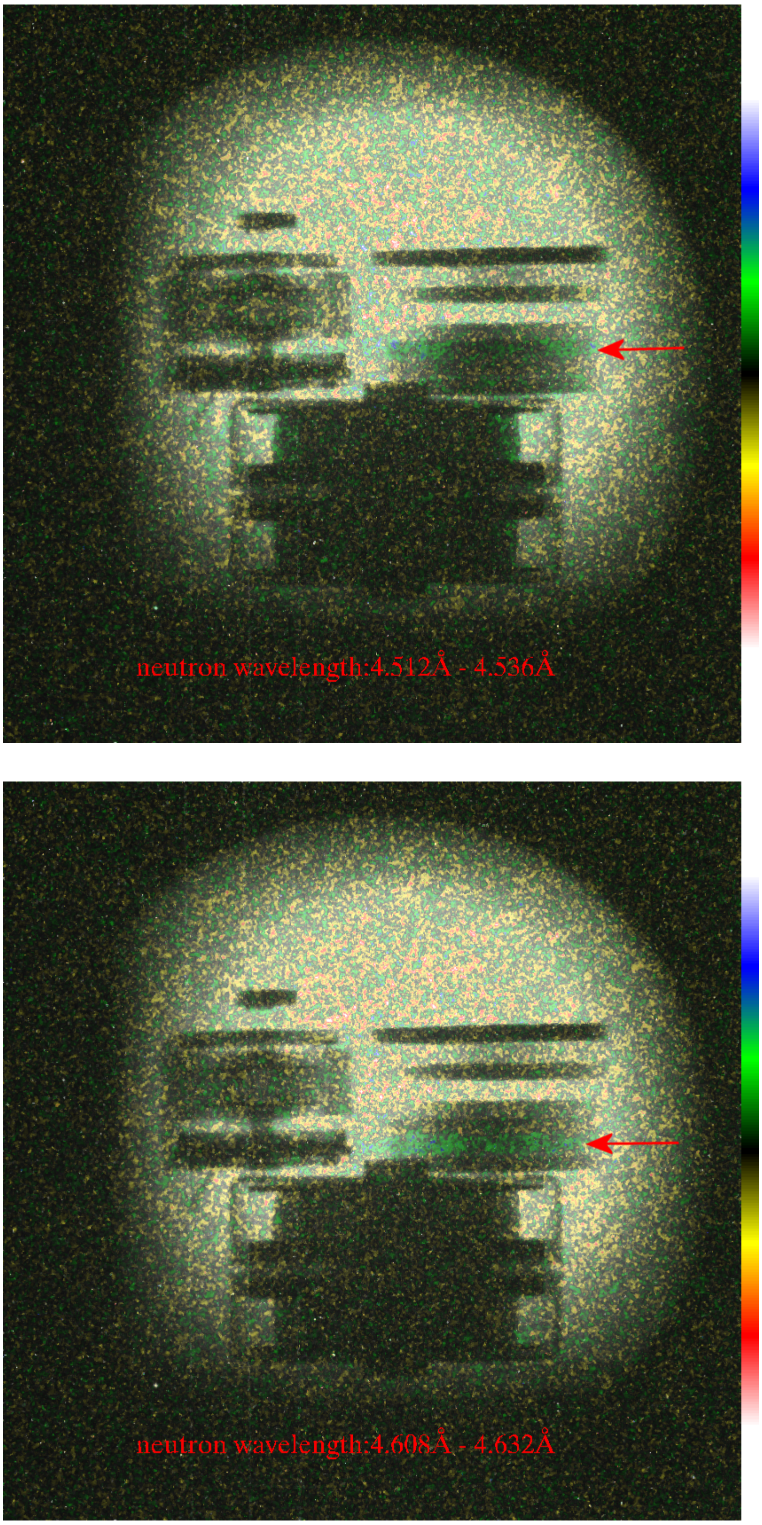

Figure 4.17: Difference of two NR at a Bragg cutoff of copper (above), difference of two NR at a Bragg cutoff of brass (below)

4.3 Quantitative NR: a compressor type refrigerator

A frequent problem in the NR data evaluation is a quantitative volume measurement. As described in chapter 3, section 3.5, the volume in dependence of the grey level g, the grey level of the empty buffer g_0, the attenuation coefficient of the liquid Σ, and the area A_{pixel} corresponding to one pixel on the scintillator, is:

$$V = \sum_{pixels of ROI} -\frac{A_{pixel}}{\Sigma} ln(\frac{g}{g_0}) \qquad \text{if } \mu \text{ is constant} \tag{4.2}$$

V ... volume of the liquid $\left[cm^3\right]$
$g(z)$ ... neutron intensity after a distance x in material $\left[\frac{neutrons}{cm^2\, s}\right]$
g_0 ... neutron intensity before the object $\left[\frac{neutrons}{cm^2\, s}\right]$
Σ ... attenuation coefficient $\left[\frac{1}{cm}\right]$
A_{pixel}.. pixel area $\left[cm^2\right]$

This evaluation was applied to NR data of a compressor type refrigerator. The evaporation and the condensation process of the cooling liquid was studied in order to optimize the machine. In the liquid buffer of the evaporator (Fig.4.18 right) the cooling liquid evaporates lowering the temperature in the inside of the deep freeze unit. Sometimes condensation in the wrong place of the circuit leads to complete malfunction of the refrigerator.

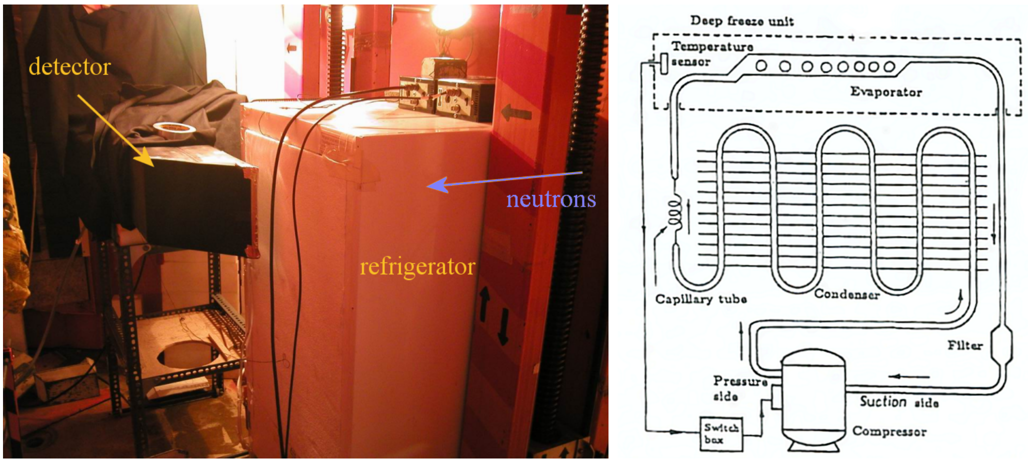

Figure 4.18: The refrigerator in front of the neutron radiography detector (left), scheme of the liquid circuit in this type of refrigerators (right)

The experiment was performed at KFKI Budapest (Fig.4.18 left). At the dynamic neutron radiography station at KFKI, a neutron flux of 10^8 n/cm^{2}s at a L/D ratio of 170 is available. The empty refrigerator was positioned on a translation table such that the liquid buffer (see 4.19) was in the beam and could be inspected. An exposure time of 1 ms for one image was chosen. The spatial resolution was 1.5 mm due to the beam divergency. The detector was a standard NR detector with a MCP intensified Peltier cooled ICCD camera from the company Princeton Instruments.
A measured NR image is visible in Fig. 4.20. With the IDL program `volume_calc.pro` the Region Of Interst (ROI) for the volume calculation and the offset grey level are chosen. All pixel in the ROI with a lower grey level than the offset contribute to the liquid volume

Figure 4.19: Photograph of the liquid buffer of a refrigerator, boiling temperature of the liquid -30°C

and are displayed in false colors. In the case of the refrigerator the evaporator was selected as ROI, the liquid in the buffer was visualized and volume was calculated via the thickness of the liquid in every pixel.

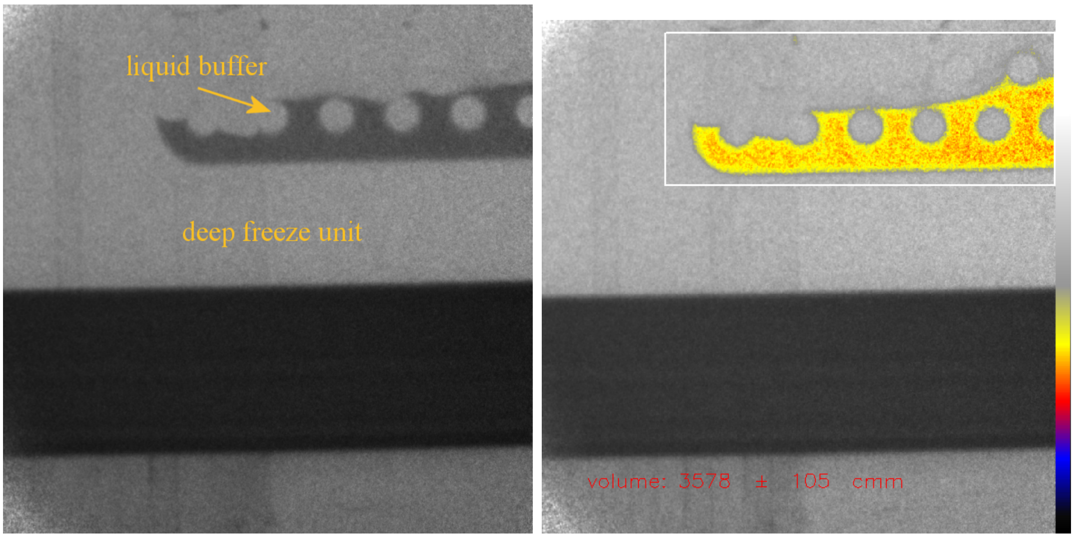

Figure 4.20: Normalized NR of the liquid buffer of the refrigerator (left); ROI of the liquid buffer (right), grey levels between 10000 and 25000 are displayed in false colors, Δt = 1.5 ms with 12000 accumulations, Δx =1.5 mm, σ=4%, FOV: 120 x 120 mm^2 and 680 x 680 pixels

For the calculation of the volume uncertainty the uncertainties of the pixel area and the attenuation coefficient were estimated. With the IDL program batch processing is possible: an unlimited number of images can be processed with the same parameters [ppt4, 46]. The palette on the right hand side of the bmp color image helps to interpret the image (Fig. 4.21).

The liquid volume in the refrigerator was successfully calculated and the program will be applied to more complex geometries in future. In the case of the refrigerator the precision for the volume calculation was a few percent. The exact pixel size and the attenuation coefficient of the cooling liquid were only estimated but could be determined by appropriate calibration measurements. Beam hardening and scattering may be the limiting factors then.

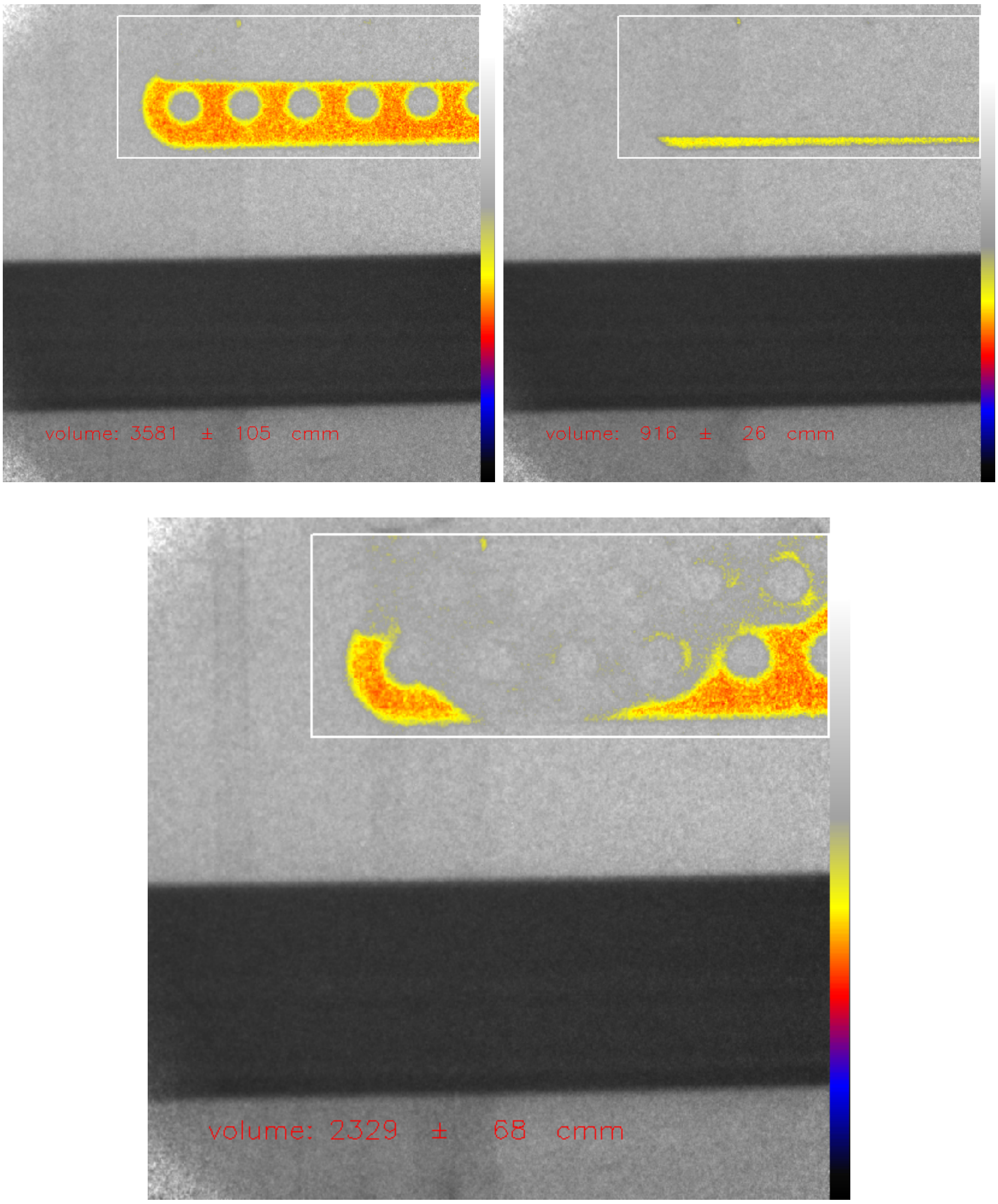

Figure 4.21: Some frames of the NR stack after the liquid volume calculation: $\Delta t = 1.5$ ms with 12000 accumulations, $\Delta x = 1.5$ mm, $\sigma = 4\%$, FOV: 120 x 120 mm^2 and 680 x 680 pixels

Appendix A

New application: fossil stone

Fossils are geological and historical objects from a time of some hundred million years ago. They can help us to lift secrets like the evolution of plants and animals on earth and the mountain formation processes. After the discovery of a fossil a very laborious, time consuming and costly preparation follows until the fossil can be admired in a museum (Fig. A.1).

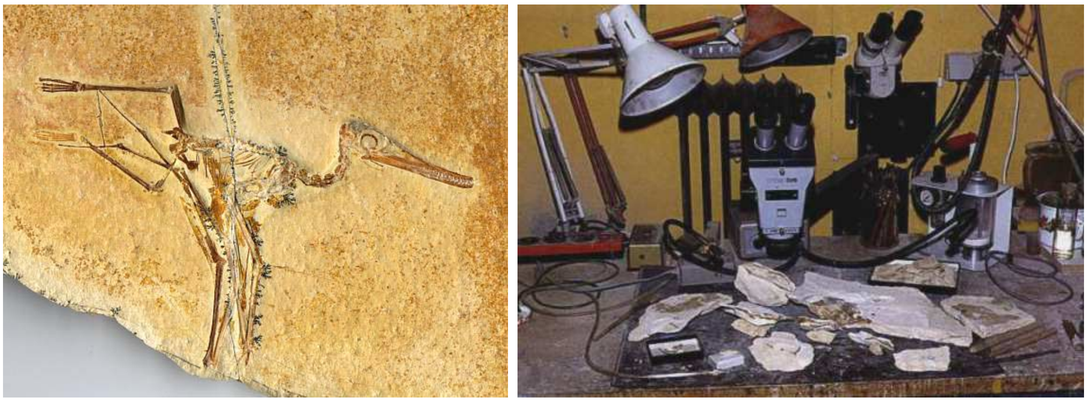

Figure A.1: Pterodactylus elegans, working place for fossil preparation.

From the many promising pieces of rocks only a few really contain a beautiful fossil. A careful and accurate preparation takes not hours but weeks or months and requires professional tools like a robust stereo microscope and appropriate grinding machines. It is worth inspecting as accurate as possible a finding before the preparation, but it is very difficult to look deep into the piece of rock and to discover the traces of plants and animals non-destructively.
The fossil stone (Fig. A.2 left) from the northern Dolomites containing fossil shells was inspected at the ANTARES facility with X-ray and with neutrons (Fig. A.2, center and right). Its age is estimated to be 240 million years which corresponds to the Trias age. Neutron imaging is the favorite technique due to the high penetration depth of neutrons and its good contrasts for hydrogenous and carbonaceous materials. In the next step a neutron tomography study was started.
In Fig. A.3 the 3D neutron tomography data set is displayed from three different points of view.

The histogam A.4 shows the grey levels of the 3D data set and the assigned colors. The high peak on the left hand side corresponds to high number of voxels with low grey levels (low neutron attenuation) like air. The smaller peak can be assigned to the fossil. The basic color ocher should be similar to the color of the stone on the photograph and

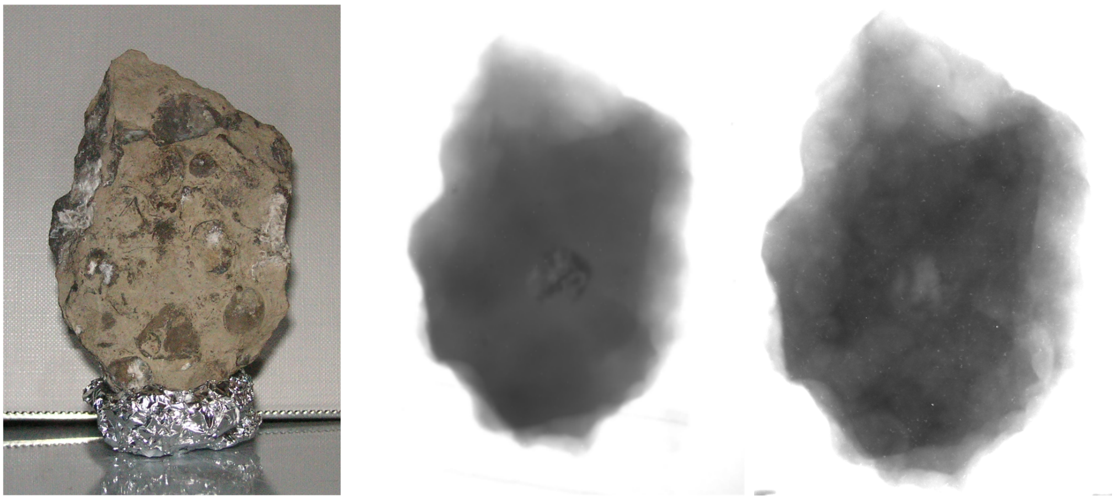

Figure A.2: Lime stone including fossil shells: Photograph (left), X-ray image (center) and NR image (right); the void is better visible in the X-ray image, the NR image gives much more contrasts for the shells

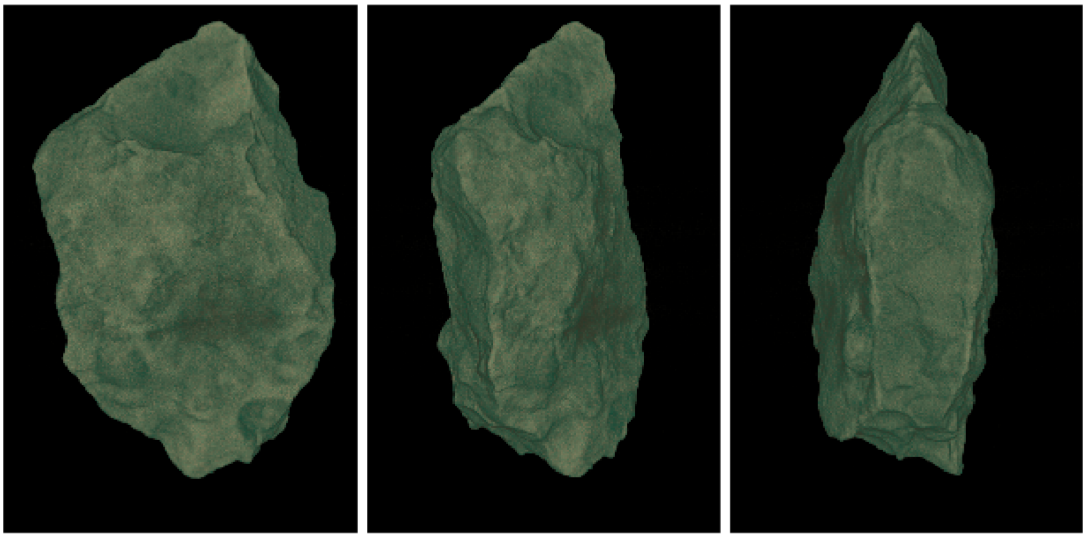

Figure A.3: NT data set of the lime stone with fossil shells: front view (left), under 45 °(center), side view(right)

the green color highlights the shells were marked. The brighter the color in the sliced the stronger is the neutron attenuation.

Fossil shells were already visible in the optical inspection of the piece of lime rock. The question was: Is it possible to get enough contrast in the NT see the shells inside the stone? At a L/D ratio of 400 a series of 400 images within a rotation of 180° were acquired, each with an accumulation time of 1.25 s. The spatial resolution of one image Δx was 0.7 mm and the relative noise σ=0.7%. With the IDL program `all_in_one` [Sch04, 24] the tomographic reconstruction was performed. After four hours on a normal PC all slices of the 3D data set were calculated.
Fig. A.5 shows two cuts of the fossil rich in detail. The position and the orientation of the shells can be clearly identified. In addition voids and creeps inside the stone appear. In the movie [ppt5, 47] the fossil is presented with more details. Neutron imaging methods are an excellent tool for the investigation of fossils. The high sensitivity for many elements

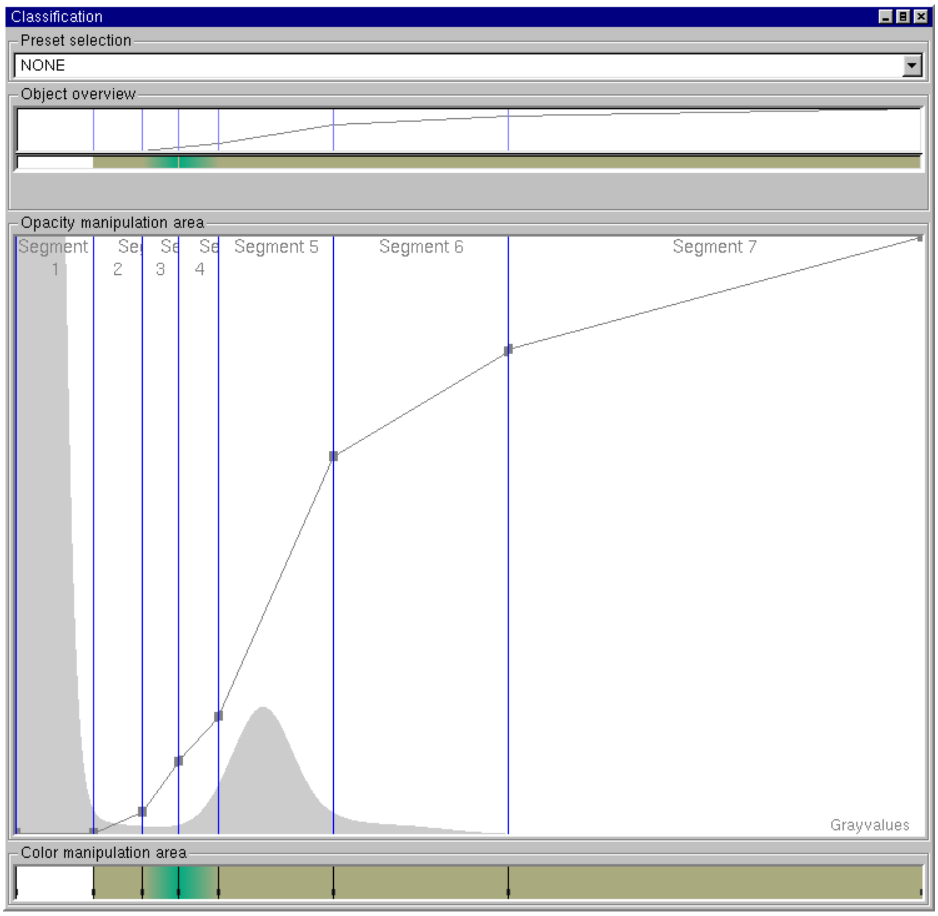

Figure A.4: Histogram and look up table of the fossil

and the capability to penetrate thick objects delivers unique information about the inside of the fossil and can support the preparation and the inspection in future.

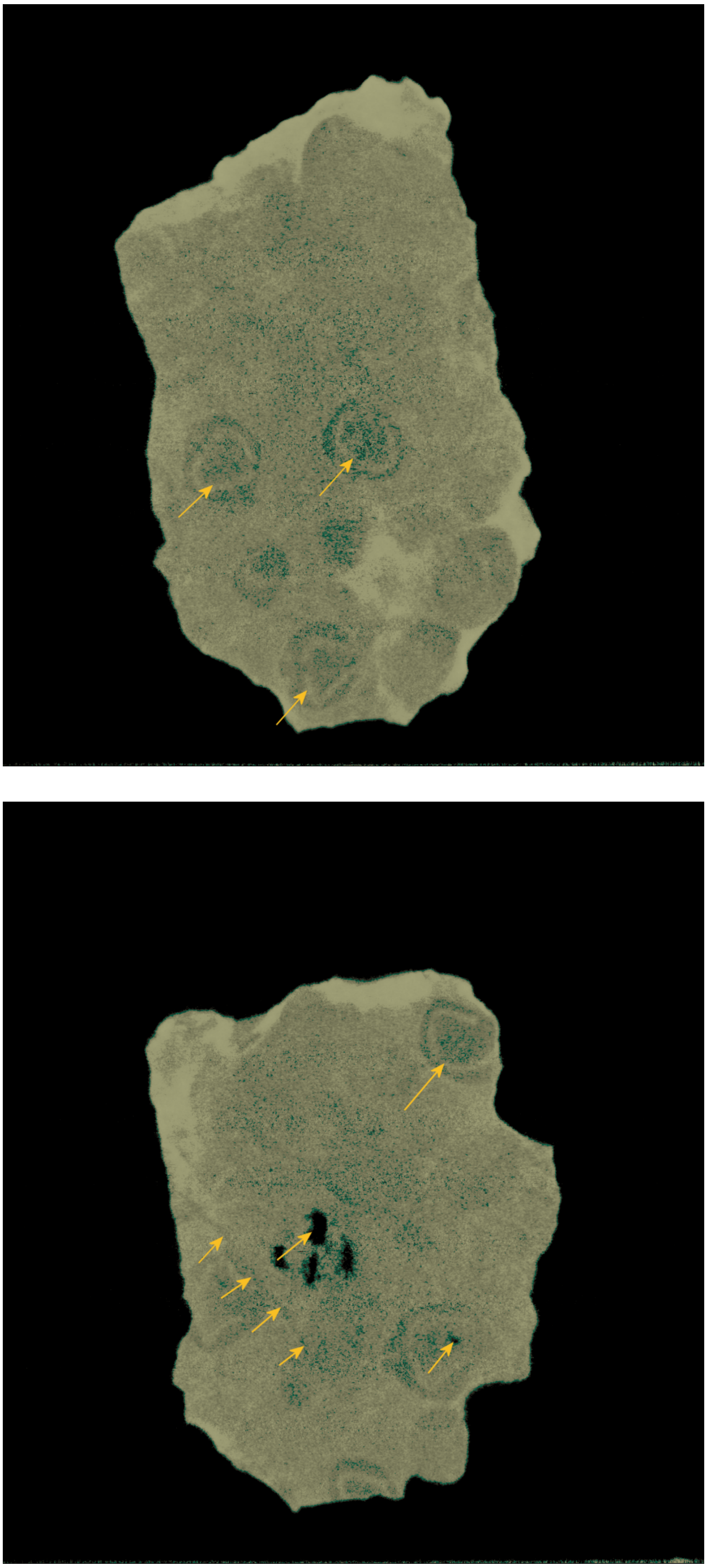

Figure A.5: Cuts through the 3D neutron tomography data set of the fossil: The position and the orientation of the shells as well as voids due to crystallization and cracks are visible.

Appendix B

Visualization method: Difference NR of an oil pump

This imaging method helps to visualize differences between two NR. As a test object an oil pump was chosen. While the eye can distinguish only with difficulties where the oil is, in the difference image with false colors it is very easy to see. The color encodes the neutron attenuation of the oil. Fig. B.1 shows the NR of the oil pump in the filled and in the empty state.

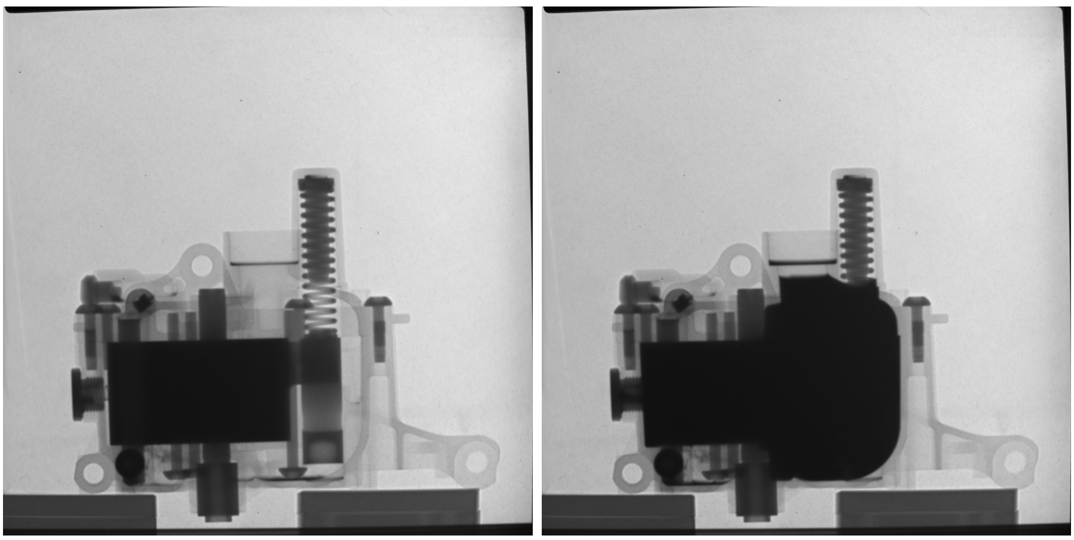

Figure B.1: NR of an empty and a filled oil pump

In the next evaluation step the NR of the filled pump was normalized (divided by) with the NR of the empty pump. The resulting image is the neutron attenuation of the oil and the uncertainty is very large in the areas of large thickness (Fig. B.2).

The visualization of the exact oil distribution in the pump was the aim. That was achieved with an image fusion of the NR image of the pump and the NR of the oil (Fig. B.3) shows in an impressive way the locations of the oil.

Such new visualization techniques shorten the time for non destructive testing and make results much easier to interpret. Pre-knowledge like geometry or knowledge of the materials is used in the evaluation procedure.

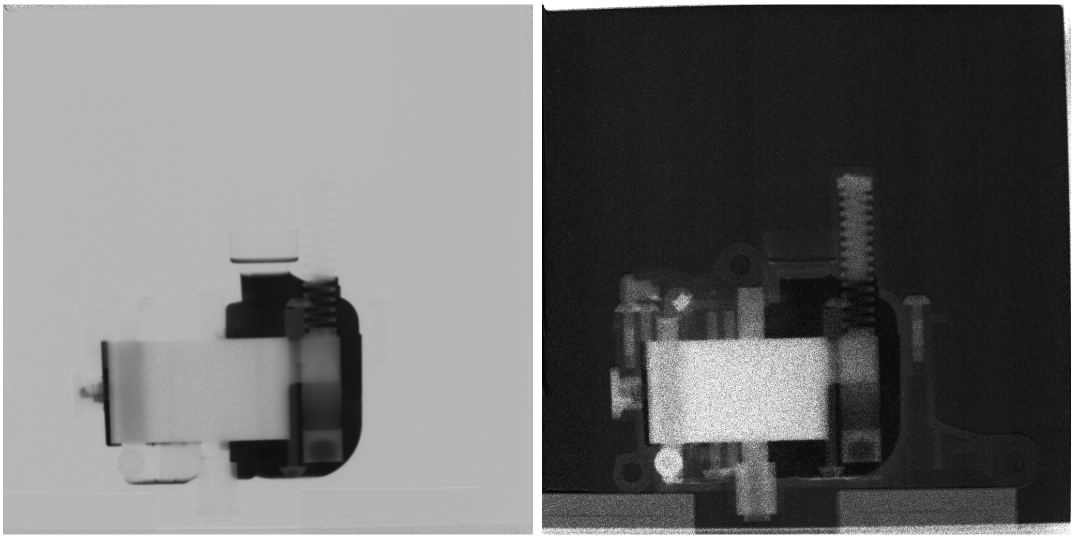

Figure B.2: NR of the oil in the pump (left),image of its uncertainty (right)

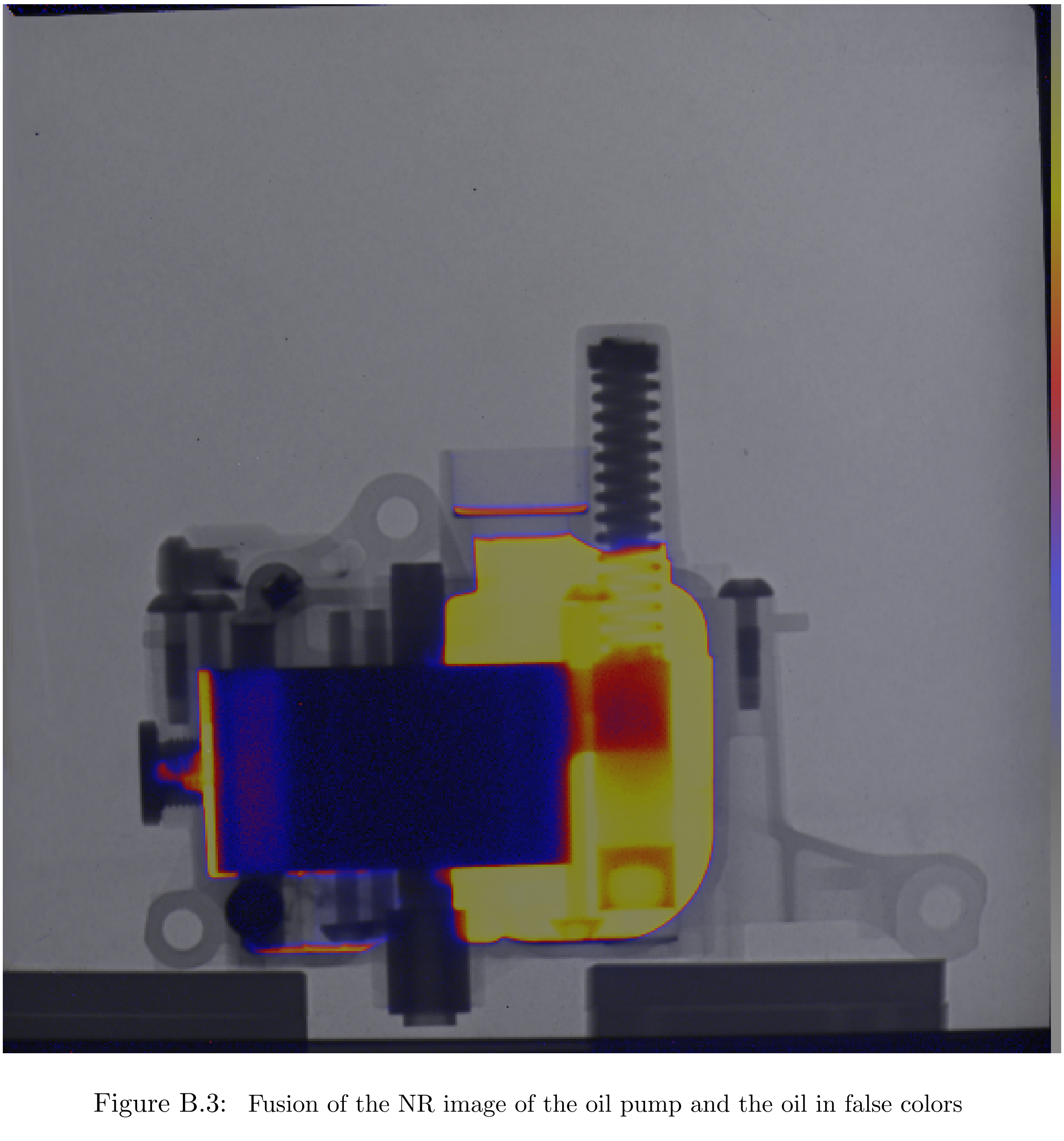

Figure B.3: Fusion of the NR image of the oil pump and the oil in false colors

List of Figures

Bibliography

[Kak88, 0] "Principles of Computerized Tomographic Imaging", A. C. Kak, M. Slaney, IEEEPress, 1988

[Eme82, 1] "Theorie der Kernreaktoren", D.Emendörfer, K. - Höcker (eds), Bibliographisches Institut AG Sürich, 1982

[Due76, 2] "Nuclear Reactor Analysis", J.J. Duedestadt, L.J. Hamilton (eds), John Wiley & sons, 1976

[Iae05, 3] International Atomic Energy Agency: `www-nds.iaea.org`, 2005

[Fur99, 4] "Frontiers of neutron scattering", Albert Furrer, World Scientific, 1999

[San01, 5] "Development and applications of a pixellated transmission detector", J. Santisteban, L. Edwards, A. Steuwer, PJ. Withers, M. R. Daymond, NJ Rhodes, E M Schooneveld, Isis annual report 2001

[Hil05, 6] "High flux neutron imaging for high-speed radiography and dynamic tomography and strongly absorbing materials", A. Hillenbach, M. Engelhard, H. Abele, R. Gähler, Nuclear Instruments and Methods in Physics Research A, 2005

[Ciz99, 7] "Performace and characteristics of a new scintillator", J.B. Cizz et al., Nuclear Instruments and Methods in Physics Research A 424 (15-19), (1999)

[Dis05, 8] Datasheet for LCD Shutter on `www.displaytech.com`, 2005

[Oly05, 9] `www.olympus-biosystems.com/templates_eng/bio_imaging/glossary_CCDchips.html`
Digital Imaging in Optical Microscopy, 1005

[Rei93, 10] "Integrated Electronic Shutter for Back-Illuminated Charge-Coupled Devices", R. Reich, R. Mountain, W. McGonagle, J. Chin-Ming Huang, J. Twichell, B. Kosicky, E. Savoye, IEEE Trans. on Electron Devices, Vol. 40/7, 1993

[Ast04, 11] Datasheet on `www.appscintech.com`, 2004

[Rop04, 12] Datasheet on `www.roperscientific.com/pdfs/datasheets/pimax/1024sb.pdf`, 2004

[Bac02, 13] "New features in cold neutron radiography and tomography: Part I: thinner scintillators and a neutron velocity selector to improve the spatial resolution", S. Baechler, N. Kardjilov, M. Dierick, J. Jolie, G. Kühne, E. Lehmann and T. Materna, Nuclear Instruments and Methods in Physics Research Section A: Accelerators, Spectrometers, Detectors and Associated Equipment, Volume 491, Issue 3, Pages 481-491, 1 October 2002

[Sch99, 14] "Neue Entwicklungen zu Radiographie und Tomographie mit thermischen Neutronen und zu deren routinemäsigem Einsatz" B. Schillinger, Dissertation an der Technischen Universität München, 1999

[Tre05, 15] "New ways in neutron tomography", W. Treimer, `http://www.physik.uni-kiel.de/kfn/Highlights/Highlight-2-engl.php`, 2005

[Sch04, 16] "Neutronen sehen was Röntgenstrahlen berborgen bleibt", B. Schillinger, T. Bücherl, ZfP-Zeitung 89, 2004

[Gru05, 17] , "Design of the neutron imaging facility ANTARES at high flux neutron source FRM-II", F. Grünauer, "Dissertation an der Technischen Universität München", 2005

[Har86, 18] "Mathematics and Physics of Neutron Radiography", A. A. Harms and D. R. Wyman, D. Reidel Publishing Company, 1986

[Has91, 19] "The Physics of medical x-ray imaging", B. H. Hasegawa, Medical Physics Publishing, Madison Wisconsin, 1991

[Kol05, 20] "Webvision, the organization of the retina and human vision", H.Kolb, E. Fernandez, R. Nelson, `http://webvision.med.utah.edu/`, 2005

[Jai89, 21] "Fundamentals of digital image processing", Anil K. Jain, Prentice Hall Information and systems sciences series, 1989

[Pra91, 22] "Digital image processing", W.K.Pratt, A Wiley-Interscience Publication John Wiley & Sons, Inc, 1991

[Idl05, 23] "Solutions for Data Visualization and Image Analysis", `http://www.rsinc.com/`

[Sch04, 24] "Aufbau einer Röntgenanlage für Radiographie und Tomographie am Experiment ANTARES am FRM-II", Micheal Schulz , Diplomarbeit an der Technischen Universität Müenchen, 2004

[Sfb05, 25] "Abschlußbericht Sonderforschungsbereich 224 Motorische Verbrennung" , Deutsche Forschungsgemeinschaft, http://www.vka.rwth-aachen.de/sfb_224/, 2005

[Bal99, 26] "Characterisation of segregation by dynamic neutron radiography",M. Balaskò E. Svab, Acta physica polonica, Vol 96 (1999)

[PSI05, 27] "The Neutron Transmission Radiography (NEUTRA) Station at PSI", http://neutra.web.psi.ch/facility/index.html, 2005

[ILL05, 28] "Neutrograph, radiography and tomography with neutrons for industry and science", http://www.neutrograph.de/, 2005

[Fer05, 29] "The new station for fast radiography and tomography at the ILL in Grenoble", T. Ferger, H. Abele, J. Brunner, R. Gaehler, B. Schillinger, J. R. Villard, September 2002

[Mac02, 30] "X-ray imaging of shock waves generated by high-pressure fuel sprays", MacPhee AG, Tate MW, Powell CF, Yue Y, Renzi MJ, Ercan A, Narayanan S, Fontes E, Walther J, Schaller J, Gruner SM, Wang J., Science. 15;295 (5558):1261-3., Feb 2002

[Bru01, 31] "Aufbau eines Teststandes für dynamische Neutronenradiographie", J. Brunner, Diplomarbeit an der Technischen Universität München, 2001

[Mue04, 32] "Bau eines Entwicklungssystems für Radiographie und Tomographie mit Neutronen", Martin Mühlbauer, Diplomarbeit an der Technischen Universität München, 2004

[Eng04, 33] "Imaging of dynamic processes with a timescale of microseconds at a thermal neutron beam", Martin Engelhardt, Diplomarbeit an der Technischen Universität München, 2004

[Sch05, 34] "Detection systems for short-time stroboscopic neutron imaging and measurements on a rotating engine", Nuclear Instruments and Methods in Physics Research Section A: Accelerators, Spectrometers, Detectors and Associated Equipment, B. Schillinger, H. Abele, J. Brunner, G. Frei, R. Gähler, A. Gildemeister, A. Hillenbach, E. Lehmann and P. Vontobel, 2 March 2005

[Bru05, 35] "Characterization of the image quality in neutron radioscopy" Nuclear Instruments and Methods in Physics Research Section A: Accelerators, Spectrometers, Detectors and Associated Equipment, In Press, Corrected Proof, available online 1 April 2005, J. Brunner, M. Engelhardt, G. Frei, A. Gildemeister, E. Lehmann, A. Hillenbach and B. Schillinger

[Von05, 36] "Dynamic imaging with a triggered and intensified CCD camera system in a high-intensity neutron beam", Nuclear Instruments and Methods in Physics Research Section A: Accelerators, Spectrometers, Detectors and Associated Equipment, P. Vontobel, G. Frei, J. Brunner, A.E. Gildemeister, M. Engelhardt, March 2005

[Kar04, 37] "Energy-selective neutron radiography and tomography at FRM", Applied Radiation and Isotopes, Volume 61, Issue 4, Pages 455-460 N. Kardjilov, B. Schillinger, E. Steichele, October 2004

[Kar03, 38] "New features in cold neutron radiography and tomography Part II: applied energy-selective neutron radiography and tomography", N. Kardjilov, S. Baechler, M. Bastürk, M. Dierick, J. Jolie, E. Lehmann, T. Materna, B. Schillinger, P. Vontobel, Nuclear Instruments and Methods in Physics Research Section A: Accelerators, Spectrometers, Detectors and Associated Equipment, Volume 501, Issues 2-3, 1 , Pages 536-546, April 2003

[San01, 39] "Time-of-flight neutron transmission diffraction", J.R. Santistaban, L. Edwards, M.E. Fitzpatrick, A. Stewer, P.J. Withers, M.-R. Daymond, M.W. Johnson, N. Rhodes, E.M.Schooneveld, Journal of Applied Cristallography . 34, 289-297, 2001

[Ste01, 40] "Strain imaging by Bragg edge neutron transmission", A. Steuwer, P.J. Withers, J.R. Santisteban, L. Edwards, G. Bruno, M.E. Fitzpatrick, M.R. Daymond, M.W. Johnson, D. Wang, Nucl. Instruments and Methods in Physics research Section A 0 1-4, 2001

[Ste01, 41] "Bragg Edge Determination for Accurate Lattice Parameter and Elastic Strain Measurement", A. Steuwer, P.J. Withers, J.R. Santisteban, L. Edwards, G. Bruno, M.E. Fitzpatrick, M.R. Daymond, M.W. Johnson, D. Wang, Phys. stat. Sol. (a) No. 2, 221-230, 2001

[ppt1, 42] "Model air craft engine" (added on compact disc: `links/ppt/hub/hub.ppt`)

[ppt1, 43] "BMW_movie" (added on compact disc: `links/ppt/bmw/bmw.ppt`)

[ppt2, 44] "Dynamic NR of a generator at FRM-II" (added on compact disc: `links/ppt/gen-frm2/gen-frm2.ppt`)

[ppt3, 45] "Energy Selective NR" (added on compact disc: `links/ppt/esnr/esnr.ppt`)

[ppt4, 46] "Quantitative NR" (added on compact disc: `links/ppt/refrigerator/refrigerator.ppt`)

[ppt5, 47] "NT of a fossil stone" (added on compact disc: `links/ppt/fossil/fossil.ppt`)

Abbreviations

CCD	... Charge Coupled Device
CVS	... Software for version management
ESF	... Edge Spread Function
ESRF	... European Synchrotron Radiation Facility, Grenoble, France
FFT	... Fast Fourier Transform
FOV	... Field Of View
FRM-II	... Forschungsreaktor München II
FWHM	... Full Width Half Maximum
ICCD	... Intensified CCD
IDL	... Interactive Data Language, software for data
	... visulization and image processing
ILL	... Institut Laue Langevin, Grenoble, France
ISIS	... Neutron Spallation Source, Oxford, UK
KFKI	... Research center of the Hungarian Accademy of Sciences, Budapest, Hungary
LSP	... Line Spread Function
MCP	... Multi Channel Plate, component of an image intensifier
MCNP	... Monte Carlo Nuclear Particle Code, software for Monte Carlo Simulations
MTF	... Modulation Transfer Function
NR	... Neutron Radiography
NT	... Neutron Tomography
NI	... Neutron Imaging
NDT	... Non Destructive Testing
PSF	... Point Spread Function
PSI	... Paul Scherrer Institut, Villigen, Switzerland
SNR	... Signal to Noise Ratio
ROI	... Region of Interest(cutout) of an image

Publications

"Aufbau eines Teststandes für dynamische Neutronenradiographie", J. Brunner, Diplomarbeit an der Technischen Universität München, 2001

"Dynamic Neutron Radiography of a combustion engine", J. Brunner, E. Lehmann, B. Schillinger, Neutron Radiography (7), Proceedings of the Seventh World Conference, Rome, Italy, September 15-21, 2002

"The new station for fast radiography and tomography at the ILL in Grenoble", T. Ferger, H. Abele, J. Brunner, R. Gähler, B. Schillinger, J. R. Villard, Neutron Radiography (7), Proceedings of the Seventh World Conference, Rome, Italy, September 15-21, 2002

"Dynamic neutron radiography of a combustion engine", J. Brunner, G. Frei, A. Hillenbach, E. Lehmann , B. Schillinger, Proceedings of the 16th World Conference of Non Destructive Testing, Montreal, Canada, `http://www.ndt.net/article/wcndt2004/index.htm`, 2004

"Characterization of the image quality in neutron radioscopy", Nuclear Instruments and Methods in Physics Research Section A: Accelerators, Spectrometers, Detectors and Associated Equipment, J. Brunner, M. Engelhardt, G. Frei, A. Gildemeister, E. Lehmann, A. Hillenbach and B. Schillinger, 1 April 2005

"Detection systems for short-time stroboscopic neutron imaging and measurements on a rotating engine", Nuclear Instruments and Methods in Physics Research Section A: Accelerators, Spectrometers, Detectors and Associated Equipment, B. Schillinger, H. Abele, J. Brunner, G. Frei, R. Gähler, A. Gildemeister, A. Hillenbach, E. Lehmann and P. Vontobel, 2 March 2005

"Dynamic imaging with a triggered and intensified CCD camera system in a high-intensity neutron beam", Nuclear Instruments and Methods in Physics Research Section A: Accelerators, Spectrometers, Detectors and Associated Equipment, P. Vontobel, G. Frei, J. Brunner, A.E. Gildemeister and M. Engelhardt, 21 March 2005

Digital version on compact disc

Conclusions

In the current study various experimental methods and computation based procedures in the field of neutron imaging were presented. Some of the results are reported world-wide for the first time. The most significant contributions of the current thesis to the further development of the neutron radiography can be named as the following:

1. The development of the stroboscopic neutron imaging technique, allowing neutron imaging at sub-millisecond time scale of periodic processes and the first visualization of a running cycle of a combustion engine running on its own.

2. The first time of flight based energy selective neutron radiography experiments using a fast gateable detector at the pulsed neutron spallation source ISIS.

3. The development of a quantitative evaluation and visualization software for the calculation of uncertainties and fast data inspection.

With stroboscopic neutron imaging periodic processes at sub-millisecond time scales can be inspected. By synchronizing a position sensitive detector with short gating times to the process, taking stroboscopically images of the same time window and summing them either by software or on the chip, the time resolution can be improved by a factor of 1000. By phase shifting of the trigger signal a neutron radiography movie can be composed. In chapter 4 this method was applied in the investigation of combustion engines and injection nozzles.

The presented energy selective neutron imaging method is based on the time of flight principle. At pulsed neutron spallation sources the neutron energies at sample position are time dependent and can be selected, again by the synchronizing detector with the neutron source and changing the phase of the trigger signal. In contrast to energy selective neutron radiography using a velocity selector or filters the energy resolution is much higher. The energies can be exactly tailored to the specific spectral attenuation properties of the material one wants to detect. At next generation spallation sources this technique will become very important.

The evaluation and visualization of the large data amounts is only possible with a highly optimized and sophisticated software. Because no commercial software is flexible enough to be adopted and expanded to our specific needs, many routines were programmed in IDL and most of them were embedded in a graphical user interface. This evaluation software (Neutroneye) is described in chapter 3.

During this work the neutron imaging facility ANTARES at FRM-II started operation. With many test experiments the facility, the detector and the data handling was characterized, improved and optimized.

The developed methods and techniques are available for the instrumentation staff, for future users and students of the neutron radiography and tomography facility ANTARES at the new research reactor FRM-II and can be further improved and expanded.

Outlook

Stroboscopic imaging will be applied to all kind of cyclic processes. The dynamics of lubrication liquids and cooling agents in metallic housings are ideally suited for an inspection with this method. For product development the objects could be adapted to neutron imaging by substitution of impenetrable materials with window materials or by downsizing of the object.

At the next generation spallation neutron sources energy selective time of flight NR will allow very precise material selective inspections, where the spectrum is tailored for the specific problem. At steady state neutron sources velocity selectors can be used for energy variation.

In future the software tools used at neutron imaging facilities will increase significantly. By the use of "pre-knowledge" about the object like geometry of material composition it will be possible to recognize complex patterns and to perform 3D measurements with sub pixel resolution.

Fitting algorithms and evolutionary software will allow automated inspection of large data series. For individual NDT problems a software like "Neutroneye" has to offer complex tools for evaluation and visualization, especially for combination of different data types.

The combination of various NDT methods like ultra sonic inspection, infrared imaging, X-ray inspection, magnetic resonance imaging, eddy current inspection, neutron imaging and others will extend our possibilities of non destructive testing impressively.

Acknowledgements

At the end of this work I would like to cordially thank all who have contributed to its successful completion.

First of all I would like to thank Prof. Dr. P. Böni for the unique opportunity to be a member in his scientific group and for his great support of new collaborations, short term scientific missions and the participation at conferences, which had a strong influence on my personal scientific development and my life.

Especially I want to thank the scientific supervisor during my PhD time Dr. B. Schillinger. With his excellent scientific understanding and technical know-how he supported me whenever necessary. His encouragement and high motivation without suppressing the necessary creativity created a extremely good atmosphere in the ANTARES group.

I want to thank all members of the ANTARES group for their help, the fruitful discussions and the fun we had together: E. Calzada, F. Grünauer, K. Lorenz, M. Mühlbauer and M. Schulz. Special thanks go to Dr. N. Kardjilov for all the help, especially at the beginning of my PhD thesis.

For the successful cooperation with the Institute Laue Langevin, Grenoble, France, I want to thank Dr. R. Gähler, H. Ballhausen, M. Engelhardt, T. Ferger, A. Gildermeister and Andreas Hillenbach.

For the successful cooperation with the Paul Scherrer Institut, Villigen, Switzerland I want to thank Dr. E. Lehmann, G. Frei, R. Hassanein and P. Vontobel.

I want to thank Dr. Marton Balaskò, who really impressed me by his brilliant way of doing NDT and made my short term scientific mission in Budapest possible. Thank you for the many new inspirations and ideas.

For the injection nozzle setup I want to thank Dr. W. Bauer from Bosch. For the setup of the car combustion engine I am grateful to Prof. Dr. K. Zeilinger and Dr. H. J. Riedl from the department of mechanical engineering and for the model air craft engine I want to thank M. Axtner.

Further I want to thank all the nice people from the workshop of the Reaktorstation and from the FRM-II software group for their commitment and their patience.

During my PhD the physics students Andreas Neubauer, Carola Oberhüttinger, Sören Schlimme, Konrad Senn and Veronika Vitztum contributed to the IDL programming, the measurements and the data evaluation.

Two students of the computer science department of the TU-München: Alex Kruppa, Franz Strasser, Alex Kruppa, Franz Strasser worked for me within the scope of an interdisciplinary project (IDP), which was very fruitful.

For the final corrections of this work I want to thank, again Dr. B. Schillinger, Dr. W. Waschkowski and N. Wieschalla.

Last but not least I want to thank my parents, my brother, all my friends and the mountains of South Tyrol, who supported me all the time.